University of New Hampshire
University of New Hampshire Scholars' Repository

Doctoral Dissertations | Student Scholarship

Spring 1992

# Nuclear structure studies of the oxygen nucleus observed with the quasielastic (electron, electron'proton) reaction

Mark Bancroft Leuschner
*University of New Hampshire, Durham*

Follow this and additional works at: https://scholars.unh.edu/dissertation

Recommended Citation
Leuschner, Mark Bancroft, "Nuclear structure studies of the oxygen nucleus observed with the quasielastic (electron, electron'proton) reaction" (1992). *Doctoral Dissertations*. 1680.
https://scholars.unh.edu/dissertation/1680

This Dissertation is brought to you for free and open access by the Student Scholarship at University of New Hampshire Scholars' Repository. It has been accepted for inclusion in Doctoral Dissertations by an authorized administrator of University of New Hampshire Scholars' Repository. For more information, please contact nicole.hentz@unh.edu.

## INFORMATION TO USERS

This manuscript has been reproduced from the microfilm master. UMI films the text directly from the original or copy submitted. Thus, some thesis and dissertation copies are in typewriter face, while others may be from any type of computer printer.

**The quality of this reproduction is dependent upon the quality of the copy submitted.** Broken or indistinct print, colored or poor quality illustrations and photographs, print bleedthrough, substandard margins, and improper alignment can adversely affect reproduction.

In the unlikely event that the author did not send UMI a complete manuscript and there are missing pages, these will be noted. Also, if unauthorized copyright material had to be removed, a note will indicate the deletion.

Oversize materials (e.g., maps, drawings, charts) are reproduced by sectioning the original, beginning at the upper left-hand corner and continuing from left to right in equal sections with small overlaps. Each original is also photographed in one exposure and is included in reduced form at the back of the book.

Photographs included in the original manuscript have been reproduced xerographically in this copy. Higher quality 6" x 9" black and white photographic prints are available for any photographs or illustrations appearing in this copy for an additional charge. Contact UMI directly to order.

U·M·I

University Microfilms International
A Bell & Howell Information Company
300 North Zeeb Road, Ann Arbor, MI 48106-1346 USA
313/761-4700 800/521-0600

Order Number 9225255

# Nuclear structure studies of the $^{16}O$ nucleus observed with the quasielastic (e,e'p) reaction

Leuschner, Mark Bancroft, Ph.D.

University of New Hampshire, 1992

U·M·I
300 N. Zeeb Rd.
Ann Arbor, MI 48106

# NUCLEAR STRUCTURE STUDIES OF THE $^{16}O$ NUCLEUS OBSERVED WITH THE QUASIELASTIC (e,e'p) REACTION

by

Mark Bancroft Leuschner
B.S., University of Massachusetts, 1985

A DISSERTATION

Submitted to the University of New Hampshire
in Partial Fulfillment of
the Requirements for the Degree of

Doctor of Philosophy
in
Physics

May, 1992

This dissertation has been examined and approved.

Dissertation director, F. William Hersman
Associate Professor of Physics

John R. Calarco
Professor of Physics

Terry G. Forbes
Research Professor of Physics
and Earth, Oceans, and Space

Jochen H. Heisenberg
Professor of Physics

Harvey K. Shepard
Professor of Physics

April 3, 1992
Date

# Acknowledgements

This dissertation would not have been possible without the considerable help of a great number of people, who providing both expertise and friendship. As I finish my graduate career after many years of work, the relief of finishing my dissertation is closely balanced by the sadness of leaving the people who have made these years as great as they've been.

First and foremost, I thank my advisor and one of my closest friends Bill Hersman, without whom this project would not have enjoyed the considerable success that it has. His enthusiasm and creativity have been an inspiration, and it is hard for me to imagine a more positive and productive working relationship than the one I've enjoyed during these past few years. I look forward to a continuing relationship in the years to come.

I thank all of the members, both past and present, of the UNH nuclear physics group. It was a pleasure to work with professors John Calarco, John Dawson, and Jochen Heisenberg. They all represent a standard of research excellence which any graduate student would aspire to. Wooyoung Kim, John Wise, and Tim Smith have all been a great help with my research, as collaborators and as friends. To my fellow graduate students Jim, Judi, and Dave, I thank you all for the good times as officemates, as housemates, as friends, and especially as collaborators during many late night shifts.

I thank Louk, Gerrit, Henk, and Gerard for their hospitality during my visits to NIKHEF, and for the many hours they all spent helping me with the analysis and interpretation of the results. I regret not having had the benefit of an even more active collaboration during the oxygen project. I hope there will be oppor-

tunities to work with you all again at NIKHEF sometime in the near future. I would also like to thank Ineke and Annemarie for their help during my visits to Amsterdam, and especially for being such good friends.

I am indebted to many great friends in the physics department at UNH, especially Kara, Professor Dawn Meredith, and Professor Bob Lambert. To my friends and co-karateka Kara and Dawn, I thank you both for your inexhaustible sense of humor, and for many a well-deserved bruise. Professor Lambert, I look forward to many more Bruins games and many more Chomsky books. The only reason I'm actually going out to Indiana is to catch up with my *Nation* subscription.

I thank Nancy Voorhis for her friendship during the past few years, and for putting up with the burden of excessive computer demands from the nuclear physics group. Without her help we would all still be mired in the stone age of computing.

Last, but certainly not least, I thank Dot, Robin, Lorraine, Pat, and Nancy for their help in administration, and for their friendship. Life as a graduate student would not have been nearly as much fun without my daily excursion down to the physics office.

# Table of Contents

# List of Tables

# List of Figures

# ABSTRACT

## NUCLEAR STRUCTURE STUDIES OF THE $^{16}$O NUCLEUS OBSERVED WITH THE QUASIELASTIC (e,e'p) REACTION

by

MARK B. LEUSCHNER

University of New Hampshire, May, 1992

The spectral function of the $^{16}$O(e,e'p)$^{15}$N reaction has been measured in quasielastic parallel kinematics. Momentum distributions are extracted for several discrete states, with special emphasis on the low-lying positive parity states of $^{15}$N. Spectroscopic factors and bound state wave functions are deduced from a distorted wave impulse approximation analysis, including coupled channels effects, employing five different optical potentials. The distribution of spectroscopic strength is determined out to $E_m$ = 40 MeV from a multipole decomposition of the spectral function continuum. The spectroscopic factor of the $2s1d$ shell of $^{16}$O, as evidenced by transitions to the positive parity ($2s_{1/2}$,$1d_{5/2}$) doublet at $E_x$ = 5.3 MeV, is found to be $0.269 \pm 0.018$. The summed spectroscopic strength of the valence $1p$ shell exhausts only $72\% \pm 5.5\%$ of the independent particle shell model limit.

# 1. Introduction

The atomic nucleus is a system of strongly interacting protons and neutrons. Exact calculations for nuclear systems with $A > 2$ are not possible due to the many-body nature of the problem. In addition, the nucleon-nucleon interaction is not well understood, thereby complicating the theoretical description even for few-body nuclear systems. As a consequence of these two factors, the description of nuclear properties is based upon models which attempt to explain the systematics of the available experimental data.

One successful model of the atomic nucleus is the shell model, in which the nucleons are assumed to move independently in a mean field representing the combined effect of the other nucleons. With the inclusion of a strong spin-orbit interaction, it was found that the nuclear shell model was able to explain the systematics of nuclear binding energies.[1] The shell model was also able to accurately predict the ground state spins and parities of odd-A nuclei.

A major difficulty of the independent particle shell model (IPSM), however, is its inability to accurately predict the excited state spectra of nuclei in terms of one-particle/one-hole ($1p-1h$) excitations. This failure is understood to be a consequence of the residual interaction, which is responsible for nucleon-nucleon correlations. These multinucleon correlations lead to the depletion of orbitals beneath the fermi level, and the subsequent population of orbitals above the fermi level. Experimentally, the extent to which multinucleon correlations contribute to the ground state wave function can therefore be determined directly by measuring the spectroscopic factor of normally unoccupied orbitals above the fermi level.

The utility of nucleon knockout reactions as a probe of single-particle wave functions has been well established. In 1957 Thyrén *et al.*[2,3,4] resolved the difference in binding energies due to knockout from two major shells in the $(p,2p)$ reaction, thereby providing a convincing confirmation of nuclear shell structure. Due to the uncertainties in the reaction mechanism for hadron-induced reactions, Jacob and Maris[5] suggested that the (e,e'p) reaction is more ideally suited for the

extraction of information pertaining to the single-nucleon nature of the nucleus. Due to improvements in experimental apparatus,[6] modern (e,e'p) experiments are now capable of resolving transitions to weakly populated final states in the residual A-1 nuclear system, thereby providing an accurate means for studying the details of the ground state nuclear wave function.

Several recent studies of the quasielastic (e,e'p) reaction have provided a wealth of information concerning the single-nucleon structure of the nucleus. One of the most profound discoveries of these studies has been the observance of a strong depletion of the summed spectroscopic strength, sometimes as much as 50%, from the valence orbitals in nuclei ranging from $^{12}$C to $^{208}$Pb. The (e,e'p) (and (d,$^3$He)) spectroscopic strengths for transitions leading to the valence orbitals for several nuclei are shown in Figure 1. These results, compiled by Kramer,[7] are a direct indication of the magnitude of the multinucleon correlation effects.

A previous measurement of the quasielastic $^{16}$O(e,e'p) reaction at Saclay by Bernheim *et al.*[10] confirmed the depletion of valence orbitals in $^{16}$O by measuring the spectroscopic factors for proton knockout leading to the two strongest $1p$ levels in $^{15}$N (the $1p_{1/2}$ ground state and the $1p_{3/2}$ third excited state). The spectroscopic factor of these two orbitals was found to be 1.18(15) and 2.28(29) protons respectively, which accounts for only about 60% of the independent particle shell model (IPSM) limit. The population of low-lying positive parity states, which would have provided insight to where the missing strength from the $1p$ shell resides, was not discussed in their analysis.

Much evidence exists on the depletion of strength from nuclear valence orbitals, but very little experimental work provides quantitative measurements of which orbitals are subsequently populated. The present $^{16}$O(e,e'p)$^{15}$N experiment, along with two previous experiments[8,9] on $^{12}$C and $^{40}$Ca, represents an effort to directly measure the occupation of normally unoccupied orbitals. For the $^{12}$C(e,e'p) experiment, the spectroscopic factors for transitions leading to states with spin and parity $J^\pi = 3/2^+$, $5/2^+$, $5/2^-$, and $7/2^-$ were extracted. Transitions to these states were interpreted to arise from proton knockout from the

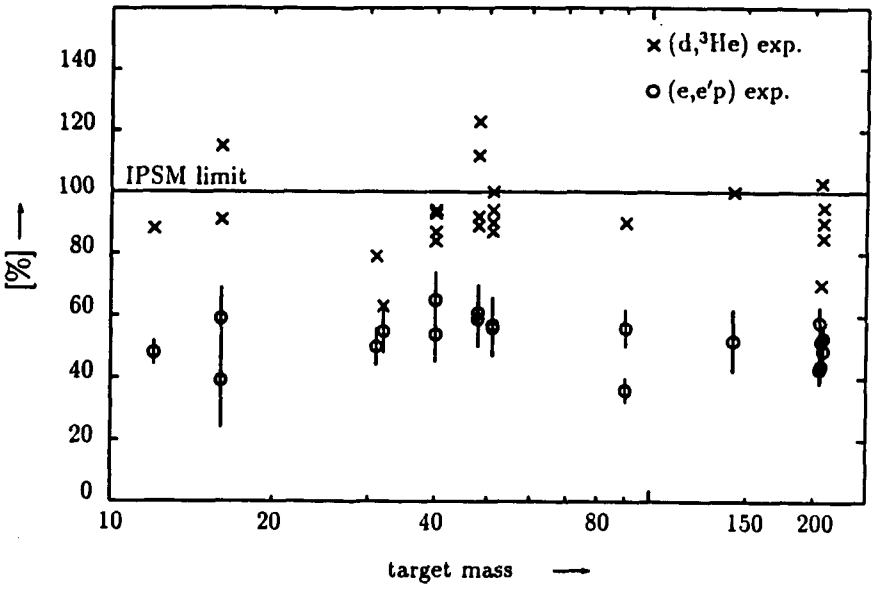


**Figure 1** Summed spectroscopic strength of the valence orbitals for various nuclei. The spectroscopic strengths are plotted as a percentage of the IPSM limit.

$2s1d$ and $1f$ shells of $^{12}$C. The summed spectroscopic factor for all transitions leading to these states was found to be $\Sigma S = 0.0268(18)$, which is much less than is required to account for the observed 43% depletion of the $1p$ shell.

For the $^{40}$Ca(e,e'p) experiment, spectroscopic factors for transitions to final states with spin and parity $J^\pi = 3/2^-$ and $7/2^-$ were extracted. Transitions leading to these final states was interpreted as evidence for the occupation of the $1f$ and-$2p$ orbitals of $^{40}$Ca. The extracted spectroscopic strength, summed over the excitation region 0-10 MeV of the final $^{39}$K nucleus, indicated a $5-6\%$ spectroscopic factor for the $1f$ shell and a $1-2\%$ spectroscopic factor for the $2p$ shell. The measured depletion of the $1d_{3/2}$ and $2s_{1/2}$ orbitals was found to be 35% and 45% respectively.

We have performed a measurement of the quasielastic $^{16}$O(e,e'p)$^{15}$N reaction

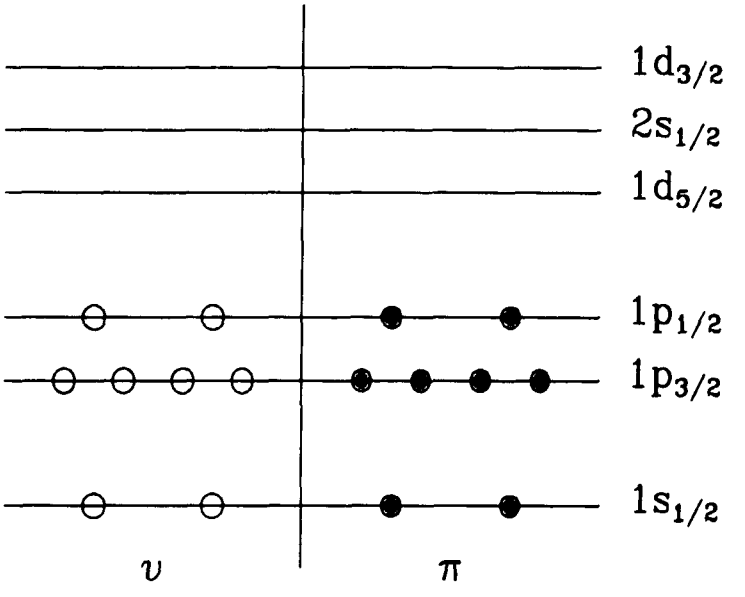


**Figure 2** Occupancy of the shell model orbitals for the $^{16}$O nucleus in the IPSM.

in order to obtain a direct quantitative measure of the effects of nucleon-nucleon correlations which lead to the spreading of proton occupancy to states above the fermi level. We have studied the depletion of the proton occupancy of the $1p$ shell in $^{16}$O, as well as the corresponding occupation of the $2s1d$ shell. The $2s1d$ shell proton occupancy was determined by measuring the spectroscopic strength for transitions leading to the positive parity doublet at $E_x = 5.3$ MeV in $^{15}$N.

The $^{16}$O nucleus is an excellent choice with which to investigate the role of multinucleon correlations using the (e,e'p) reaction. The ground state spin and parity of $^{16}$O is $0^+$, so when a proton is knocked out, the residual $^{15}$N nucleus is left with the spin and parity of the vacated hole state. The nuclear configuration of $^{16}$O in the independent particle shell model is $(1s)^4(1p)^{12}$ (see Figure 2), so the low-lying excitation spectrum of $^{15}$N populated by the $^{16}$O(e,e'p) reaction should be dominated by a $1/2^-$ state and a $3/2^-$ state, representing knockout from the valence $1p$ shell of $^{16}$O. The presence of low-lying positive parity states (see Figure

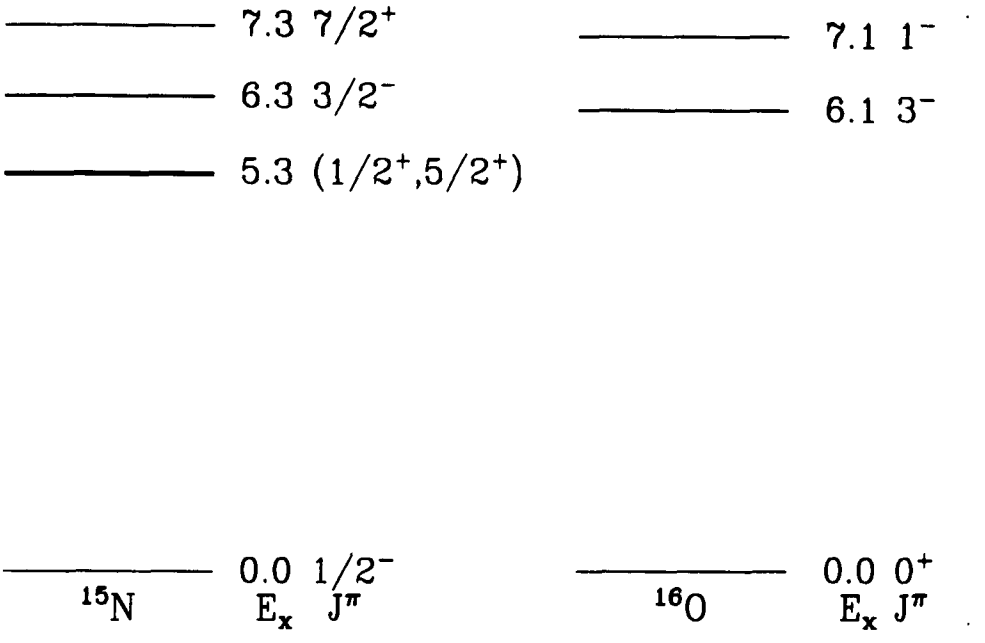


**Figure 3** Low-lying excitation spectrum for the $^{15}$N and $^{16}$O nuclei.

3) could only arise from the knockout of protons from the $2s1d$ shell of $^{16}$O. An unambiguous, quantitative, measure of the occupation of the $2s1d$ shell in $^{16}$O can therefore be obtained by extracting the spectroscopic factor arising from proton knockout leading to the population of the $(1/2^+, 5/2^+)$ doublet at $E_x = 5.3$ MeV in the $^{15}$N spectrum.

In chapter 2 we briefly outline the formalism of the impulse approximation in order to provide a concise framework in which to discuss the results. Chapter 3 describes the experimental setup and the data reduction. In chapter 4 we describe the distorted wave impulse approximation analysis of the $^{16}$O spectral function, including coupled channels effects. In the last chapter we present the conclusions of our analysis.

# 2. Description of the (e,e'p) Reaction

## 2.1 Introduction

The theoretical description of the (e,e'p) reaction in the plane wave impulse approximation (PWIA) and the distorted wave impulse approximation (DWIA) formalism is described in detail in several papers.[11] In this chapter we outline only the salient features in order to provide a framework for discussions in subsequent sections.

In order to derive an (e,e'p) cross section several approximations concerning the reaction process are necessary. First, the exchange of only one virtual photon (the Born approximation) between the incident electron and the target nucleus is considered. This approximation is easily justified since the probability for each additional photon exchange is known from quantum electrodynamics to decrease according to the fine structure constant $\alpha \sim 1/137$. The weakness of the electromagnetic interaction provides the additional advantage that the entire nuclear volume is probed, so that the wave functions of deeply bound protons can be studied. This is an important advantage over spectroscopic studies employing hadronic probes, which have larger cross sections and therefore higher event rates, but which are largely sensitive to the nuclear surface.

The second assumption commonly made in deriving the (e,e'p) cross section is that the total quasielastic cross section can be calculated from a coherent sum of amplitudes due to scattering from individual nucleons. Experimental evidence which supports this assumption exists[12] via the observation that inclusive electron scattering spectra for all nuclei exhibit a strong peak centered at an energy transfer consistent with elastic electron-proton scattering kinematics. The quasielastic kinematic requirement implies that the energy and momentum of the virtual photon are transferred to a single nucleon. From considerations of energy and momentum conservation this requirement can be written (nonrelativistically) as

$$\omega = \frac{q^2}{2m_p} + \langle B \rangle \tag{2.1}$$

where $\omega$ and $q$ are the energy and momentum transferred to the nucleon, and $m_p$ is the proton mass. The transferred energy of the quasielastic reaction is offset relative to that of true elastic scattering kinematics by an amount $B$, which is needed to overcome the binding energy of the initially bound nucleon and to transfer it into the continuum.

The final approximation contained within the PWIA and DWIA derivations of the (e,e'p) cross section is that the coupling of the virtual photon to the bound nucleon is the same as that for coupling to a free nucleon, but modified for off-shell effects. The most simple interpretation of the (e,e'p) cross section is that it is due to scattering from a collection of noninteracting nucleons, and that each nucleon has the same dynamical behavior as a free nucleon. This set of assumptions is commonly known as the *impulse approximation*. Bound nucleons are known to be off the free nucleon mass shell, however, so a prescription describing the off-shell nucleon current must be applied in the derivation of the cross section. The approach followed for the current analysis is based on the prescription due to Deforest,[13] which emphasizes current conservation.

In the following two sections we discuss the kinematics of the (e,e'p) reaction and the general formalism of electron-nuclear interactions. In section 4 we outline the derivation of the PWIA, and in section 5 we discuss the derivation of the DWIA. In the last section we briefly describe the calculation of the unfactorized cross section employed in the present analysis of the $^{16}$O spectral function.

## 2.2 Kinematics

The quasielastic (e,e'p) scattering reaction is illustrated schematically in Figure 5. The incoming electron with four-momentum $k$ scatters from the target nucleus and emerges from the reaction with four-momentum momentum $k'$, emitting a virtual photon with four-momentum $q$ in the process. The virtual photon is absorbed by a single nucleon within the target nucleus, which is then ejected with a final four-momentum $p'$. The initial nucleus is assumed to be at rest in the laboratory frame, and the residual nuclear four-momentum is denoted by $p_{A-1}$.

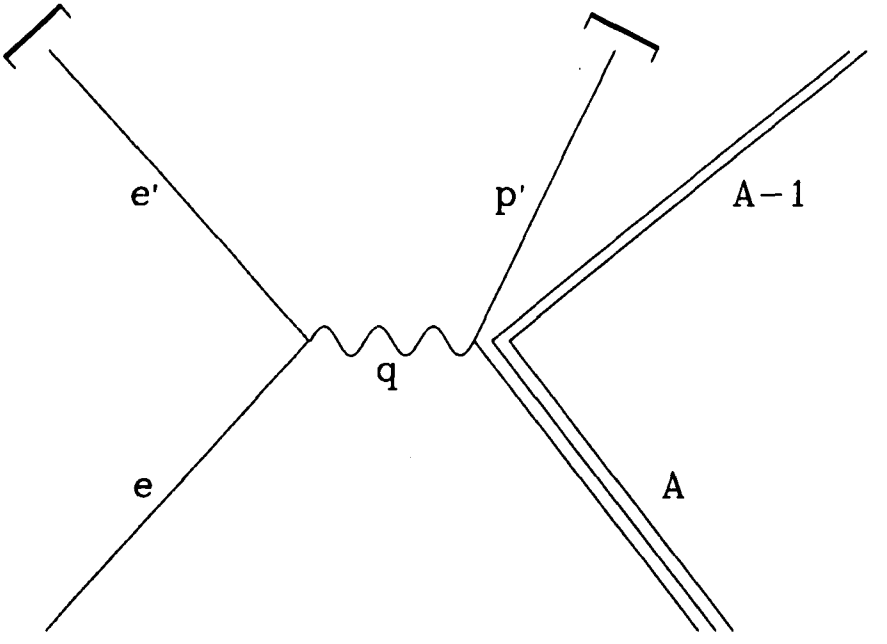


**Figure 4** Schematic illustration of the (e,e'p) reaction.

From the asymptotic particle vectors the missing four-momentum of the reaction (the momentum of the unobserved recoiling A-1 nucleus), $p_m = (E_m, \mathbf{p}_m)$, can be constructed. The missing energy $E_m$ is equal to the binding energy of the struck proton within the target nucleus, plus the possible excitation energy of the A-1 nucleus.

$$E_m = k - k' - T_{p'} - T_{A-1} = E_{sep} + E_{ex} \tag{2.2}$$

$$\mathbf{p}_m = \mathbf{e} - \mathbf{e}' - \mathbf{p}' = \mathbf{q} - \mathbf{p}' \tag{2.3}$$

The kinetic energy of the knocked out proton and residual nucleus are denoted by $T_{p'}$ and $T_{A-1}$ respectively, while the energies of the incident and scattered electrons are denoted by $k$ and $k'$. If one assumes that the ejected proton emerges from the target without additional interactions with the A-1 nucleus, then $-\mathbf{p}_m$ is equal to the momentum of the ejected proton in the nucleus before it absorbs the virtual photon. The four-momentum of the initial proton can then be written

as $p_m = (E_m, -\mathbf{p}_m)$ where the momentum component differs only in sign from the true missing momentum of the reaction. This sign convention for the missing momentum is followed henceforth in this text.

From the kinematical description of the (e,e'p) reaction it is apparent that nucleon knockout reactions can be used to measure the energy and momentum of individual bound nucleons. By extension, the entire energy and momentum distribution of the nucleus can be mapped out by varying the acceptance of the detection apparatus.

## 2.3 The (e,e'p) Differential Cross Section

The general form of the (e,e'p) differential cross section can be written, according to the derivation by Raskin and Donnelly,[14] as a contraction of two tensors

$$\frac{d\sigma}{d\epsilon' d\Omega_{\epsilon'} d\Omega_{p'}} = K \eta_{\mu\nu} W^{\mu\nu} \tag{2.4}$$

where $\eta_{\mu\nu}$ is the electron tensor and $W^{\mu\nu}$ is the nuclear tensor. The overall kinematical constants have been consolidated within the factor $K$, which is given in the lab frame by

$$K = \frac{\alpha^2 m_e^2 M_p M_{A-1}}{2\pi^3 M_A} \frac{k' p_{p'}}{k (Q^2)^2} \frac{1}{f_{rec}} \tag{2.5}$$

where $\alpha$ is the fine structure constant, $f_{rec}$ is the nuclear recoil factor, and $Q = (\omega, \mathbf{q})$ is the four-momentum transfer.

The electron tensor is well known from quantum electrodynamics,[15] while the nuclear tensor depends on the matrix elements of the unknown nuclear four-current $J^\mu = (\mathbf{J}, i\rho)$. The nuclear tensor, which contains all of the nuclear structure information which can be extracted from the (e,e'p) reaction, is given by[13]

$$W^{\mu\nu} = \overline{\sum_i} \sum_f \delta(E) \langle f, \mathbf{p}' \mid J^\mu(q) \mid i \rangle \langle f, \mathbf{p}' \mid J^\nu(q) \mid i \rangle^* \tag{2.6}$$

Where the summation over indices $i$ and $f$ indicate an average over initial states and a sum over allowable final states of the nuclear system, respectively. The delta function $\delta(E)$ indicates overall conservation of energy for the reaction.

The contraction of the electron and nuclear tensors is generally expressed as a sum of electromagnetic response functions. The differential cross section for electromagnetic scattering reactions in the center-of-mass can be written in the Born approximation as[14]

$$\frac{d\sigma}{d\epsilon' d\Omega_{\epsilon'} d\Omega_{p'}} = \frac{M_p M_{A-1} p_{p'}}{8\pi^3 W} \sigma_{Mott} \sum_j v_j R^j_{fi} \tag{2.7}$$

where the $v_j$ are kinematical factors and the $R^j_{fi}$ are the electromagnetic response functions. The invariant mass of the final hadronic system is denoted by $W$. The $v_j$ depend only on the electron kinematics (energy transfer, momentum transfer, and scattering angle), and contain no information about the structure of the target nucleus. The Mott cross section $\sigma_{Mott}$ is given by

$$\sigma_{Mott} = \left( \frac{\alpha \hbar c}{k_0} \frac{\cos \frac{\theta_{\epsilon'}}{2}}{\sin^2 \frac{\theta_{\epsilon'}}{2}} \right)^2 \frac{1}{1 + \frac{2k_0}{M_A} \sin^2 \frac{\theta_{\epsilon'}}{2}} \tag{2.8}$$

where $k_0$ is the incident electron energy and $\theta_{\epsilon'}$ is the angle of the scattered electron.

In the absence of polarized beams and polarized targets expression (2.7) reduces to

$$\frac{d\sigma}{d\epsilon' d\Omega_{\epsilon'} d\Omega_{p'}} = K \sigma_{Mott} \Big( v_L R^L_{fi} + v_T R^T_{fi} + v_{TT} R^{TT}_{fi} \cos(2\phi) + v_{LT} R^{LT}_{fi} \cos(\phi) \Big) \tag{2.9}$$

where $\phi$ is the azimuthal out-of-plane angle and the kinematical factor $K$ is the same as in expression (2.7). The four terms are the longitudinal, transverse, transverse-transverse interference, and longitudinal-transverse interference response functions respectively. The longitudinal and transverse directions, as well as the out-of-plane angles, are defined relative to the direction of the exchanged virtual photon. The longitudinal response functions are related to the matrix elements of the nuclear charge operator, and the transverse response functions are related to the matrix elements of the nuclear current operator. Expression (2.9) is simplified in the case of *parallel* kinematics, where the emerging

proton is detected in the direction parallel to the momentum transfer. In this case the two interference response functions $R^{TT}$ and $R^{TL}$ vanish, and only the longitudinal and transverse response functions contribute to the cross section.

Thus far we have developed the (e,e'p) formalism within the most general possible framework. The only approximation invoked in the preceding derivation was the Born approximation. In order to proceed further, however, more approximations must be made due to the complexity of the nuclear system. To calculate the nuclear tensor matrix elements of expression (2.6), an explicit form of the nuclear current $J^{\mu}(q)$ must be supplied. Furthermore, the calculation of the final state wave function is greatly complicated when final state interactions (FSI) are considered. The incorporation of FSI effects into the description of the (e,e'p) cross section is necessary because the knocked out proton and the residual A-1 nucleus interact via the strong interaction. In the following two sections we discuss two approximations of the (e,e'p) cross section; the plane wave impulse approximation and the distorted wave impulse approximation.

## 2.4 The Plane Wave Impulse Approximation

The PWIA provides the most straightforward framework in which to interpret (e,e'p) results. There are two essential approximations needed to derive the PWIA cross section; first, the impulse approximation (discussed above) is assumed to be appropriate, and second, the outgoing proton wave function is approximated as a plane wave (no final state interaction). In the IPSM, the hole state vacated by the knocked out proton is an eigenstate of the target nuclear potential, so the nuclear matrix element of expression (2.6) can be written

$$\langle f, \mathbf{p}' \mid J^{\mu}(q) \mid i \rangle = \int d\mathbf{r}_i e^{i\mathbf{q}\cdot\mathbf{r}_i} \langle \mathbf{p}' \mid o_{if}(\mathbf{r}_i) \rangle \tag{2.10}$$

where $o_{if}(\mathbf{r}_i)$ is the overlap between the initial and final state nuclear wave function. If a plane wave is substituted for the outgoing proton wave function, ex-

pression (2.10) becomes

$$\langle f, \mathbf{p}' \mid J^{\mu}(q) \mid i \rangle = \int d\mathbf{r}_i e^{i(\mathbf{q}-\mathbf{p}')\cdot\mathbf{r}_i} \phi_{if}(\mathbf{r}_i) \tag{2.11}$$

Expression (2.11) is the fourier transform of the overlap integral between the initial and final nuclear wave function. The factor $\mathbf{q} - \mathbf{p}'$ is the missing momentum $\mathbf{p}_m$ (see equation (2.3)) of the reaction. Combining expressions (2.4), (2.6), and (2.11), the PWIA expression for the (e,e'p) cross section can be written in the familiar factorized form

$$\frac{d^6\sigma}{d\mathbf{k}'\, d\mathbf{p}'} = p' E' \sigma_{ep} S(E_m, \mathbf{p}_m) \tag{2.12}$$

where $\sigma_{ep}$ is the elementary electron-proton cross section modified for off-shell effects, and $S(E_m, \mathbf{p}_m)$ is the spectral function. The scattered electron and outgoing proton three-momenta are denoted by $\mathbf{k}'$ and $\mathbf{p}'$ respectively. In the PWIA the missing energy and missing momentum are equal to the initial energy and momentum of the struck nucleon, hence the spectral function represents the probability that a nucleon in the nucleus has momentum $\mathbf{p}_m$ and energy $E_m$. It is written as

$$S(E_m, \mathbf{p}_m) = \sum_f \mid \phi_{if}(\mathbf{p}_m) \mid^2 \delta(E_m - E_f - E_i) \tag{2.13}$$

where $f$ denotes the final states of the A-1 system and $\phi_{if}(\mathbf{p}_m)$ is the fourier transform of the overlap integral. The overlap integral is generally replaced by a single-particle wave function

$$\phi_{if}(\mathbf{r}) = \langle \Psi_f(1..A-1) \mid \Psi_i(1..A) \rangle = A_\alpha \phi_\alpha(\mathbf{r}) \tag{2.14}$$

where the square of the amplitude $A_\alpha$ is the spectroscopic factor $S_\alpha$, and $\phi_\alpha(\mathbf{r})$ is a single-particle wave function with quantum numbers $\alpha$. In principle the overlap integral is more complicated than in the IPSM picture. Final state interactions and nucleon-nucleon correlations prevent the hole state from being a true eigenstate of the target nuclear system. In the context of the IPSM and PWIA, however, we can interpret $S_\alpha$ as the proton occupancy of the state $\phi_\alpha$.

One point of comparison between theory and experiment is the momentum distribution. The momentum distribution is calculated by integrating the spectral function over a missing energy interval of interest (usually a discrete transition)

$$\rho_\alpha(p_m) = \int S(E_m, \mathbf{p}_m)\, dE_m \tag{2.15}$$

The spectroscopic factor for a discrete state with quantum numbers $\alpha$ is then obtained by integrating the momentum distribution over all missing momenta

$$S_\alpha = 4\pi \int \rho_\alpha(p_m)\, p_m^2\, dp_m \tag{2.16}$$

In practice the spectral function is measured up to a missing momentum of about 300 MeV/c, and the integration is extended to higher missing momenta by extrapolating the calculated momentum distribution to 500 MeV/c.

The simple PWIA model illustrates the utility of the (e,e'p) reaction for obtaining spectroscopic information. Occupancies of single-particle orbitals can be extracted from the experimental (e,e'p) cross section by measuring the spectral function over a sufficient missing energy and missing momentum range.

## 2.5 The Distorted Wave Impulse Approximation

In order to provide a more realistic calculation of the (e,e'p) cross section the effects due to the final state interaction between the outgoing proton and the residual A-1 nuclear system must be accounted for. In the DWIA the plane wave assumed in the derivation of expression (2.12) is replaced by a distorted proton wave function generated in an optical potential. The general form of the optical potential is given by

$$U_{opt} = U_C(r) - U_R(r) + U_{so}(r)\sigma \cdot \mathbf{l} \tag{2.17}$$

where $U_C(r)$ is the Coulomb potential. The central ($U_R$) and spin-orbit ($U_{so}$)

terms of the optical potential contain both real ($V$) and imaginary ($W$) terms

$$U_R(r) = V f_v(r) + iW f_w(r) \tag{2.18}$$

$$U_{so}(r) = \left(\frac{\hbar}{m_\pi c}\right)^2 [V_{so} g_v(r) + iW_{so} g_w(r)] \tag{2.19}$$

where the $f_i(r)$ and $g_i(r)$ terms are the Woods-Saxon shape and the derivative of the Woods-Saxon shape respectively

$$f_i(r) = \frac{1}{1 + \exp[(r - R_i)/a_i]} \qquad \{i = V, W\} \tag{2.20}$$

$$g_i(r) = \frac{1}{r}\frac{d}{dr} f_i(r) = \frac{1}{a}\frac{\exp[(r - R_i)/a_i]}{1 + \exp[(r - R_i)/a_i]} \tag{2.21}$$

If one neglects the spin-orbit potential then the (e,e'p) cross section can still be written in a factorized form[11]

$$\frac{d^6\sigma}{d\mathbf{k}'\, d\mathbf{p}'} = p' E' \sigma_{ep} S^D(E_m, \mathbf{p}_m, \mathbf{p}') \tag{2.22}$$

where the distorted spectral function $S^D(E_m, \mathbf{p}_m, \mathbf{p}')$ is related to the momentum distribution in a manner analagous to expression (2.13)

$$S^D(E_m, \mathbf{p}_m, \mathbf{p}') = \sum_f \mid \phi^D_{if}(\mathbf{p}_m, \mathbf{p}') \mid^2 \delta(E_m - E_f - E_i) \tag{2.23}$$

and the distorted overlap integral $\phi^D_{if}(\mathbf{p}_m, \mathbf{p}')$ is written

$$\phi^D_{if}(\mathbf{p}_m, \mathbf{p}') = \int d\mathbf{r}_i \psi_{p'}(\mathbf{r}) e^{i(\mathbf{q} - \mathbf{p}')\cdot\mathbf{r}_i} \phi_{if}(r_i) \tag{2.24}$$

It can be easily seen that equation (2.24) reduces to the plane wave result of expression (2.10) if a plane wave is substituted for $\psi_{p'}$, which is the distorted wave function of the ejected proton calculated using the optical potential of expression (2.17). The factorization in expression (2.22) has been shown[16] to be nearly exact in the case of parallel kinematics.

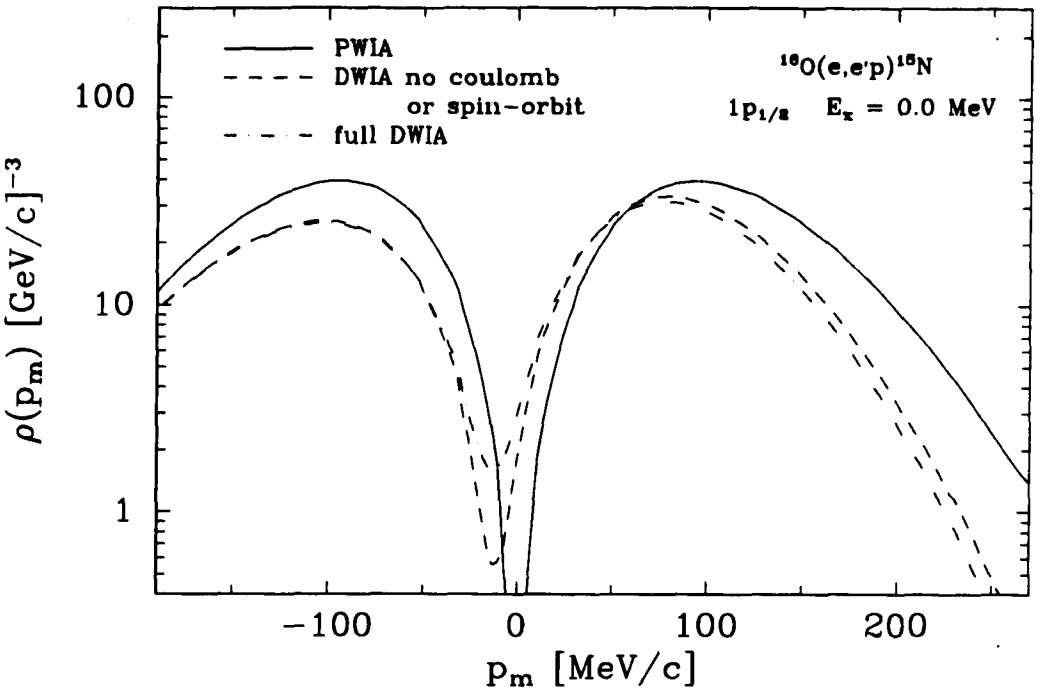


**Figure 5** Comparison of the $^{16}$O(e,e'p)$^{15}$N ground state $1p_{1/2}$ momentum distribution for the PWIA (solid), DWIA (dot-dashed), and DWIA not including spin-orbit and coulomb distortions (dashed).

Once proton distortions are included, the spectral function no longer depends solely on the energy and momentum of the bound proton, but also on the momentum with which it is ejected. The optical potential which describes the distortion of the outgoing proton must therefore reflect the kinematics of each reaction under consideration. Figure 5 illustrates the effect of the FSI on the momentum distribution for the $1p_{1/2}$ ground state of $^{15}$N. The major effect of the FSI on the momentum distribution is a shift towards negative missing momenta due to the real part of the optical potential, and a reduction of the magnitude of the momentum distribution due to the imaginary part of the optical potential. This absorption accounts for the proton flux which is removed from its original outgoing channel by final state interactions.

When the full description of the FSI is incorporated, including spin-orbit

couplings, the (e,e'p) cross section can no longer be factorized as in expressions (2.12) or (2.22). However, an *effective* spectral function can still be defined by dividing the unfactorized cross section by the electron-proton cross section

$$S^{eff}(E_m, \mathbf{p_m}) = \frac{d^6\sigma}{d\mathbf{k}'\, d\mathbf{p}'} \frac{1}{p' E' \sigma_{ep}} \tag{2.25}$$

The difference between the DWIA momentum distribution including spin-orbit distortions and the momentum distribution neglecting these terms is shown in figure 6. The major effect due to the spin-orbit potential is the filling in of the region surrounding $p_m = 0$ MeV/c. The overall normalization of the two calculations is nearly the same, indicating that to a first approximation the extracted spectroscopic factors are not highly sensitive to the spin-orbit interaction. The increasingly poor agreement between the two calculations at higher missing momenta leads to a difference in the extracted *rms* radius of the bound state wave function. The correlation between the spectroscopic strength and the *rms* radius of the bound state wave function is small, but not negligible, indicating that the spin-orbit effect must be carefully considered in the analysis of the (e,e'p) spectral function. The effect of the spin-orbit potential on the spectroscopic factor of the $1p_{3/2}$ state at $E_x = 6.3$ MeV in $^{15}$N is considered in detail in section 4.2.

One consequence arising from the optical potential description of proton distortions is that the bound and final state proton wave functions are not orthogonal, since they are generated from two different Hamiltonians. In order to confidently extract spectroscopic information from the (e,e'p) reaction the effect on the (e,e'p) cross section due to this *orthogonality defect* must be determined. In an investigation of this effect by Boffi *et al.*,[17] the (e,e'p) cross section calculated in the unfactorized DWIA approach, as discussed above, and the cross section orthogonalized in a Gram-Schmidt approach were compared. The results of the comparison indicated that the nonorthogonal component of the overlap integral was numerically small, thus preserving the interpretation of the overlap integral (equation (2.14)) as a bound state wave function. In the present analysis we have neglected the nonorthogonal component altogether.

## 2.6 SUMMARY

For the present analysis we have made use of an unfactorized DWIA calculation of the (e,e'p) cross section.[18] The prescription of DeForest[13] has been used for the off-shell electron-proton cross section $\sigma_{ep}$. In addition to the distortion of the outgoing proton wave, the distortion of the electron wave due to the nuclear coulomb potential is also calculated to first order in the eikonal approximation.[19,20] Since the optical potential is known to be non-local,[21] a correction is applied to the bound state and outgoing proton wave functions.[22]

# 3. Experiment and Data Reduction

All $^{16}$O(e,e'p) data were acquired at the Medium Energy Accelerator (MEA) at NIKHEF-K. The scattered electron and knocked out proton were detected in a pair of high resolution magnetic spectrometers. A cross section of the spectrometer setup is shown in Figure 4. The detection equipment in each spectrometer consisted of multiwire drift chambers, scintillators, and a Čerenkov counter to determine the energy, scattering angle, and type of the detected particles. The details of the accelerator and detection system are presented in detail by De Vries *et al.*[23]

The targets used for the $^{16}$O(e,e'p) experiment were liquid water ($H_2O$) and liquid heavy water ($^2H_2O$). The inelastic excitations of the contaminant nuclei in solid compound targets, such as lithium oxide or beryllium oxide, would have interfered with the $^{16}$O spectral function. Hydrogen, the "contaminant" nucleus in $H_2O$, produces a singular coincidence response at ($E_m = 0, \mathbf{p_m} = 0$) which is easily identified and separated in most cases from the $^{16}$O spectral function. At low missing momenta, however, it was found that the strong radiation tail from the hydrogen peak obscured much of the $^{16}$O spectrum. For measurements in this kinematical region, heavy water was used as a target. The (e,e'p) coincidence reaction from the contaminant deuteron nucleus produces a relatively low, broad response (since the final state momentum is shared by the undetected neutron) which was easily identified and subtracted from the $^{16}$O spectral function.

The water target apparatus employed was developed at Mainz[24,25] and consisted of a recirculation and cooling system which produced a thin waterfall in front of the beam. The waterfall was isolated from the vacuum of the spectrometers and beam transport system by a thin steel foil. The atmosphere surrounding the water film, which consisted of hydrogen or helium gas, was maintained at a pressure of approximately 1/10 atm. The effect of this atmosphere and the surrounding foil on the emerging electron and proton momenta was found to be negligible.

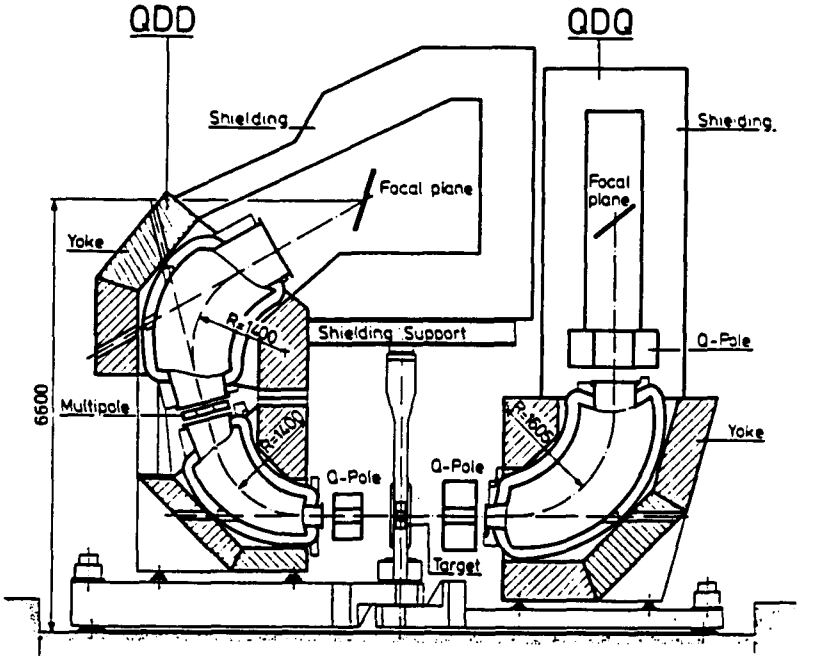


**Figure 6** The dual-spectrometer coincidence setup at NIKHEF. The QDD spectrometer (left) is used to detect the scattered electron, while the QDQ (right) is used to detect the knocked out proton.

The elastic $^{16}O(e,e')$ cross section was measured at regular intervals throughout the experiment using the water target apparatus. The absolute thickness of the water target was determined by comparing the elastic cross section to the elastic $^{16}O(e,e')$ cross section obtained from a previous measurement[26] using a solid target of known thickness. The water target thickness was found to be extremely stable, varying slowly within the range $30.9 - 33.4$ mg/cm$^2$ $\pm$ 5.1%. The uncertainty in the target thickness, which was mostly due to the statistical accuracy of the elastic measurements, was the single largest contribution to the total systematic error for the present experiment. The target thickness was monitored continuously during the intervals between elastic calibrations using the singles rates in each of the two magnetic spectrometers.

The systematic errors relating to the coincidence setup at NIKHEF have been

| quantity | uncertainty | % effect on the spectral function |
|---|---|---|
| incident beam energy | 0.1% | 0.3 |
| electron scattering angle | 1.0 mrad | 0.4 |
| proton scattering angle | 2.0 mrad | 0.2 |
| electron solid angle | 1.0% | 1.0 |
| proton solid angle | 1.9% | 1.9 |
| electron detection efficiency | 0.2% | 0.2 |
| $\varepsilon_p \varepsilon_{C'}$ | 0.7% | 0.7 |
| target thickness: | | |
| via relative normalization | 0.1-0.6% | 0.1-0.6 |
| via absolute normalization | 3.0-5.0% | 3.0-5.0 |
| total experimental uncertainty | | 3.8-5.5 |

**Table 1** Systematic errors in the $^{16}O(e,e'p)^{15}N$ experiment.

evaluated previously.[23,27,28] For the present experiment, systematic errors involving charge integration and target angle are contained within the uncertainty in the target thickness. The coincidence detection efficiency was measured several times via the kinematically overdetermined $^1H(e,e'p)$ reaction, yielding an average efficiency $\varepsilon_p \varepsilon_{C'} = 98.8\% \pm 0.7\%$. Table 1 lists the systematic errors in the measurement and their effect on the extracted momentum distributions. In some cases the error depends on the particular kinematical situation, so a range of errors is given. The total experimental systematic *rms* error for the present experiment has been determined to be 5.5%.

The coincidence reaction $^{16}O(e,e'p)^{15}N$ was measured in quasielastic parallel kinematics at three different beam energies: $E_0$ = 304.456, and 521 MeV. The total kinetic energy in the center of mass system between the outgoing proton and the recoiling $^{15}N$ nucleus was kept constant at 90 MeV. Since the center of mass energy was kept constant, effects due to the final state interaction remain the same for all kinematics. Table 2 lists the relevant kinematical parameters of

| $p_m$ MeV/c | E0 MeV | $\theta_{e'}$ deg | $P_{e'}$ MeV/c | $\theta_{p'}$ deg | $P_{p'}$ MeV/c | $T_{com}$ MeV | Q mC |
|---|---|---|---|---|---|---|---|
| -150.5 | 520.6 | 78.3 | 405.6 | 42.2 | 441.1 | 87.7 | 250.0 |
| -100.1 | 520.6 | 78.0 | 388.8 | 40.8 | 481.6 | 105.5 | 310.0 |
| -81.5 | 455.8 | 81.2 | 335.4 | 39.5 | 441.7 | 89.9 | 65.7 |
| -40.8 | 455.8 | 72.8 | 336.9 | 42.2 | 438.9 | 90.0 | 209.7 |
| 1.8 | 520.6 | 58.5 | 397.0 | 47.4 | 460.2 | 99.7 | 65.1 |
| 39.4 | 455.8 | 57.1 | 339.7 | 46.5 | 433.0 | 90.0 | 150.0 |
| 79.4 | 455.8 | 49.7 | 340.8 | 48.0 | 430.0 | 90.0 | 118.2 |
| 118.9 | 455.8 | 42.5 | 341.7 | 48.7 | 427.1 | 90.0 | 110.0 |
| 159.4 | 455.8 | 35.3 | 342.5 | 48.5 | 424.1 | 90.0 | 61.0 |
| 191.6 | 455.8 | 29.3 | 342.4 | 47.1 | 421.7 | 90.0 | 43.2 |
| 216.5 | 304.4 | 40.6 | 188.9 | 38.2 | 419.1 | 89.6 | 130.0 |
| 250.5 | 304.4 | 30.2 | 196.1 | 36.0 | 417.6 | 90.0 | 36.5 |

**Table 2** The kinematics of the $^{16}O(e,e'p)^{15}N$ experiment. $T_{com}$ is the total center of mass kinetic energy between the recoiling $^{15}N$ nucleus and the knocked out proton, and Q is the total charge accumulated at each kinematics.

the experiment.

The reduction of raw spectrometer data to the experimental spectral function proceeds through several stages. Selected spectrometer data are recorded event-by-event on magnetic tapes during the experiment for a later off-line analysis. To reduce the potentially high singles rate a hardware coincidence requirement between the two spectrometers is imposed on the data stream. The width of the coincidence (usually about 50 ns.) is chosen to allow for every conceivable path-length (and hence time-of-flight) difference between the proton and electron arms. For beam bursts in which the hardware coincidence is satisfied, the time for each singles event from each spectrometer is compared to the time of the hardware coincidence, and those events which fall within a selected time window are recorded on tape.

Coincident (e,e'p) events are selected in software from the recorded data by comparing the arrival times of each electron with each proton in a beam burst.

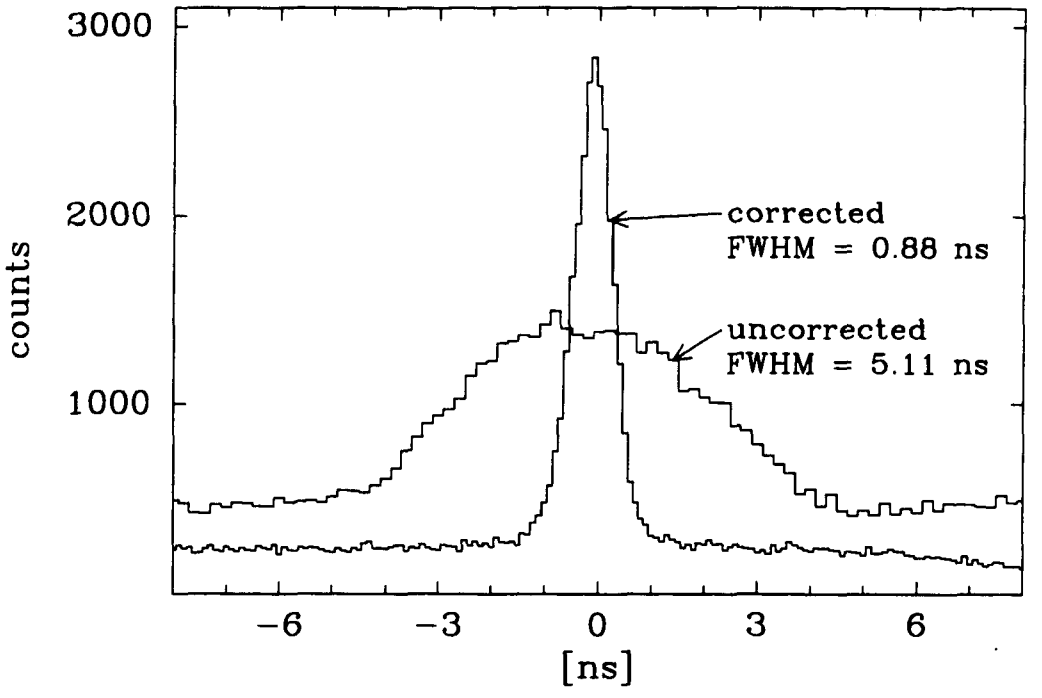


**Figure 7** The corrected and uncorrected coincidence timing spectra for the kinematics centered about $p_m$ = 160 MeV/c.

Beam bursts for which no unambiguous one-to-one electron-proton match can be made are not processed any further, and a corresponding deadtime correction is made at a later stage of the analysis. The trajectory for each particle through its spectrometer is then calculated for the remaining *singular coincidences*. From these orbits the true flight time of the particle from the reaction vertex to the spectrometer focal plane is calculated, and the coincidence timing is adjusted to compensate for differences in the length of the flight path for each particle. The resulting coincidence timing resolution was found to be better than 1 ns. for all kinematics. Figure 7 shows the uncorrected and corrected coincidence timing peaks for the kinematics centered about $p_m$ = 80 MeV/c.

Once the particle orbits through the spectrometers are known, it is possible to construct the particle vectors at the reaction vertex. From these vectors the missing energy and missing momentum ($E_m$,$\mathbf{p}_m$) of the reaction can be calculated.

Events which fall within a selected time gate (2.5 – 3.0 ns. wide) about the corrected coincidence timing peak are sorted into a two-dimensional histogram $N(E_m, p_m)$ of accepted events, while those which fall outside these limits are sorted into a histogram $A(E_m, p_m)$ of accidental coincidences. Since there exists a certain number of accidental events underneath the coincidence timing peak, an accidental subtraction must be made from the $N(E_m, p_m)$ spectrum to yield the true coincidence spectrum $T(E_m, p_m)$. Figure 8 shows the $N(E_m, p_m)$ and $A(E_m, p_m)$ spectra for the kinematics centered about $p_m$ = 220 MeV/c and $p_m$ = 250 MeV/c. The residual accidental background is easily seen as a low broad peak in both $N(\epsilon_m, p_m)$ spectra.

The six-fold differential cross section is related to the true coincidence spectrum as follows:

$$\frac{d^6\sigma}{d\mathbf{k}'\, d\mathbf{p}'} = K\sigma_{ep}\, \frac{N_{corr}}{N_t N_e}\, \frac{T(E_m, p_m)}{V(E_m, p_m)} \tag{3.1}$$

where $N_{corr}$ is the product of all the deadtime and efficiency correction factors, $N_t$ is the number of target nuclei per unit area, $N_e$ is the number of incident electrons, and $V(E_m, p_m)$ is the detection volume. The calculation of the detection volume is discussed in the following section. The factor $K\sigma_{ep}$ is applied separately for each event in the $T(E_m, p_m)$ spectrum, since there exist several different combinations of electron and proton momenta which can contribute to the same $(E_m, p_m)$ bin.

## 3.1 Calculation of the Detection Volume

The detection volume reflects the probability that an (e,e'p) event with missing energy $E_m$ and missing momentum $p_m$ can be detected within the experimental spectrometer acceptance. In laboratory coordinates the detection volume is uniform over the energy and angular acceptance of the detection system. However, when one wants to express the cross section in a spectral function representation then the detection volume must be mapped into the coordinates of missing energy

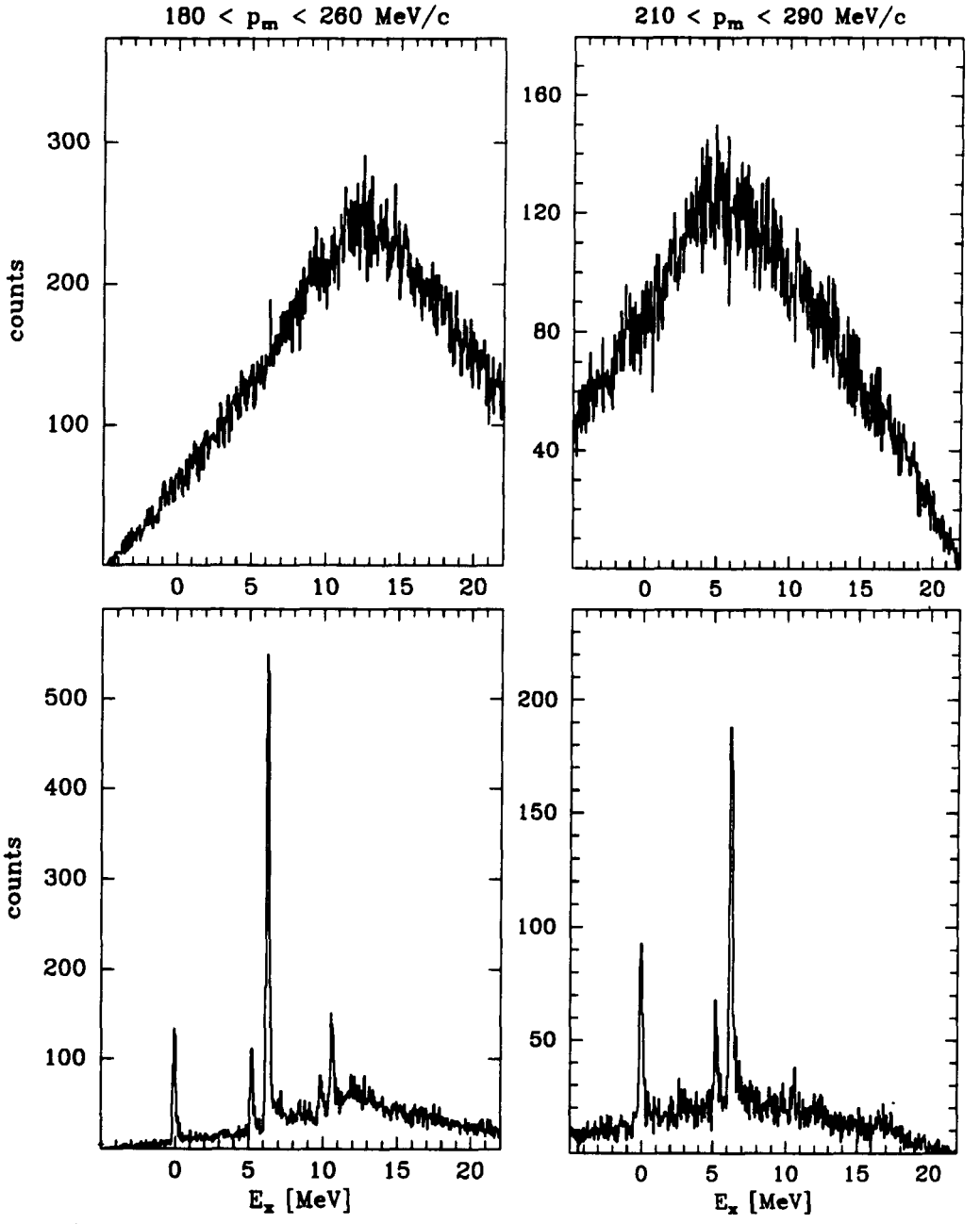


**Figure 8** Spectra of accidental coincidences $A(E_m)$ (top) and real coincidences $N(E_m)$ (bottom) for the kinematics centered about $p_m = 220$ MeV/c (left) and $p_m = 250$ MeV/c (right). The missing momentum has been integrated in each of the four graphs.

and missing momentum. The detection volume of a $(E_m, p_m)$ bin is given by

$$V(E_m, p_m) = \int_A \delta(E_m - E'_m)\delta(p_m - p'_m)\, dE_{e'}\, d\Omega_{e'}\, dE_{p'}\, d\Omega_{p'} \qquad (3.2)$$

where $e'$ and $p'$ denote the detected electron and proton, and the limits of integration $A$ run over the energy and angular acceptance of the two spectrometers.

The missing energy and missing momentum are complicated functions of the configuration space variables. In practice the integral in the above expression cannot be solved analytically, so instead a Monte Carlo method is used. For the Monte Carlo integration a distribution of random events is generated uniformly over the energy and angular acceptance of both spectrometers. The statistical error due to this integration can be made negligibly small by generating a large enough number of Monte Carlo events. For the present $^{16}$O analysis the detection volume was calculated for each kinematics from three million events. The resulting statistical integration error was less than one percent per ($E_m$,$p_m$) bin on an average.

The spectrum of accidental coincidences $A(E_m, p_m)$ can also be simulated via the same Monte Carlo method. In contrast to the detection volume integration, events for the accidental coincidence simulation are generated according to the experimentally observed energy and angular distribution of singles events in both spectrometers. The inclusive single arm data required for this calculation are recorded simultaneously during the experiment along with the coincidence data.

The extraction of the experimental spectral function is directly dependent upon the accurate determination of the detection volume, as can be seen from equation (3.1). It is therefore of crucial importance to determine the proper geometrical input (spectrometer angles and aperture positions) to the Monte Carlo calculation of the detection volume. Since the detection volume is not a direct experimental observable we have optimized the geometrical description of the spectrometer apparatus by comparing the experimental accidental coincidence spectrum to a Monte Carlo simulation of the same spectrum. A $\chi^2$ minimization

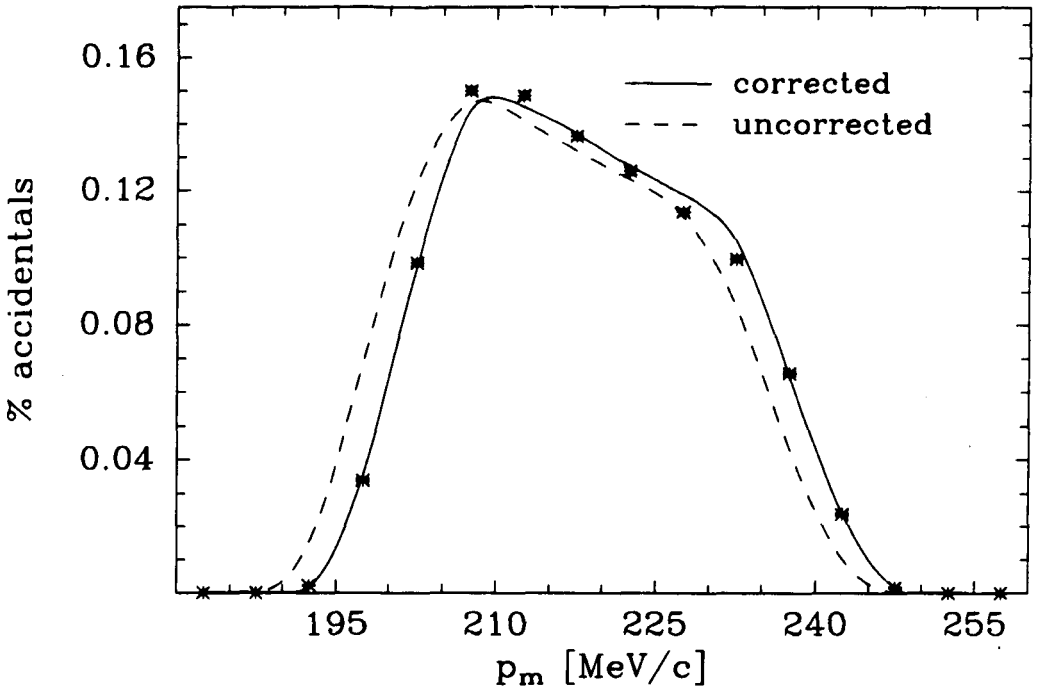


**Figure 9** Corrected and uncorrected simulated accidental spectrum for the kinematics centered about $p_m$ = 220 MeV/c. The data points represent the experimentally observed accidental distribution. The spectra have been integrated over missing energy.

was performed by dividing each spectrum into 160 bins ($8 \times \Delta p_m$ = 10 MeV/c, $20 \times \Delta E_m = 2MeV$) and adjusting the aperture positions for each spectrometer until the maximum agreement between the two spectra was found. In this manner we achieved a global optimization of the aperture positions which reflected the complete ($E_m$,$p_m$) dependence of the accidental coincidence spectrum on the spectrometer geometry.

For the present experiment, adjustments in the position of the electron spectrometer aperture of up to 5 mrad in the horizontal direction and 4 mrad in the vertical direction were required. Adjustments of these magnitudes are comparable to the likely error of the mechanical driving systems for each aperture. The optimization of the accidental calculation was found to be independent of the location

of the proton spectrometer aperture, due to the fact that in parallel kinematics one is mostly sensitive to the magnitude of the knocked out proton momentum, and relatively little by it's angle. Figure 9 compares an uncorrected and a corrected accidental spectrum for the kinematics centered about $p_m$ = 220 MeV/c. The difference between the corrected and uncorrected accidental simulations is due to a change in the location of the electron spectrometer aperture of 5 mrad in the horizontal direction and 2 mrad in the vertical direction. The effect of these aperture adjustments on the detection volume was found to be greater than 50% for some ($E_m$,$p_m$) bins.

The accuracy of the detection volume calibration was checked by comparing sets of redundant spectral function measurements, each made with a different spectrometer arrangement. The missing momentum acceptance of the NIKHEF QDD-QDQ spectrometer setup is approximately 80 MeV/c. The central missing momenta of the kinematics measured for the present experiment were separated by increments of 40 MeV/c, thus ensuring that there was a large overlapping ($E_m$,$p_m$) region sampled between neighboring measurements. The quality of the detection volume optimization becomes readily apparent since the momentum distribution is calculated at least twice for each missing energy and missing momentum bin. We observed no deviations between redundant measurements beyond the statistical accuracy of the data.

Figure 8 illustrates the influence of the experimental detection volume on the measurement of the spectral function. The distribution of accidental events is given by the shape of the detection volume folded with the singles distribution in each spectrometer. For many kinematics the shape of the accidental spectrum is essentially the same as the detection volume because the singles spectra are nearly flat. For the purposes of this discussion we will assume that they have the same shape. As figure 8 shows, the shape of the acceptance varies considerably across the ($E_m$, $p_m$) plane, thereby necessitating a proper positioning of the spectrometers so that the physical region of interest has the benefit of the maximum detection volume weight. For the present experiment we were primarily interested

in the positive parity doublet located at $E_x = 5.3$ MeV ($E_m = 17.4$ MeV), so the spectrometers were arranged at each kinematics to optimize the detection volume for this region. For the kinematics centered at $p_m = 220$ MeV/c the detectors were mistakenly positioned so that an *excitation* energy of $E_x = 17$ MeV fell at the center of the detection volume, rather than a missing energy of 17 MeV. The effect of this mistake is apparent on the $1p_{1/2}$ ground state, whose count rate is quenched almost to the level of the weakly populated $E_x = 5.3$ MeV doublet.

## 3.2 Radiative Corrections

In electron scattering experiments the electron is prone to energy losses via radiative processes in the target. As a result, events appear in the experimental spectrum at higher missing energies than the actual missing energy of the primary reaction. These radiative processes give rise to the *radiation tail* which is seen in all inclusive electron scattering spectra.

The radiation tail is generally not a problem in the analysis of inclusive (e,e′) data. Cross sections for discrete transitions can be extracted from the missing energy spectrum with fitting routines incorporating an empirical peak shape which also accounts for the radiation tail.

In (e,e′p) experiments this situation is complicated somewhat. Since the missing momentum depends on the momentum of both detected particles, as well as that of the initial electron, a radiative loss by any of these three external particles will result in an incorrect determination of the missing momentum. The radiation tail in the (e,e′p) spectral function will therefore propagate across the plane of the spectral function in both the missing energy direction *and* the missing momentum direction.

In order to calculate the momentum distribution for a discrete state accurately, the integration of the peak must be carried out over two dimensions (rather than one, as is the case for (e,e′) spectra). Due to the difficulty of such an integration, particularly in cases where the density of states is high, an alternative approach is followed whereby the spectral function strength resulting from events

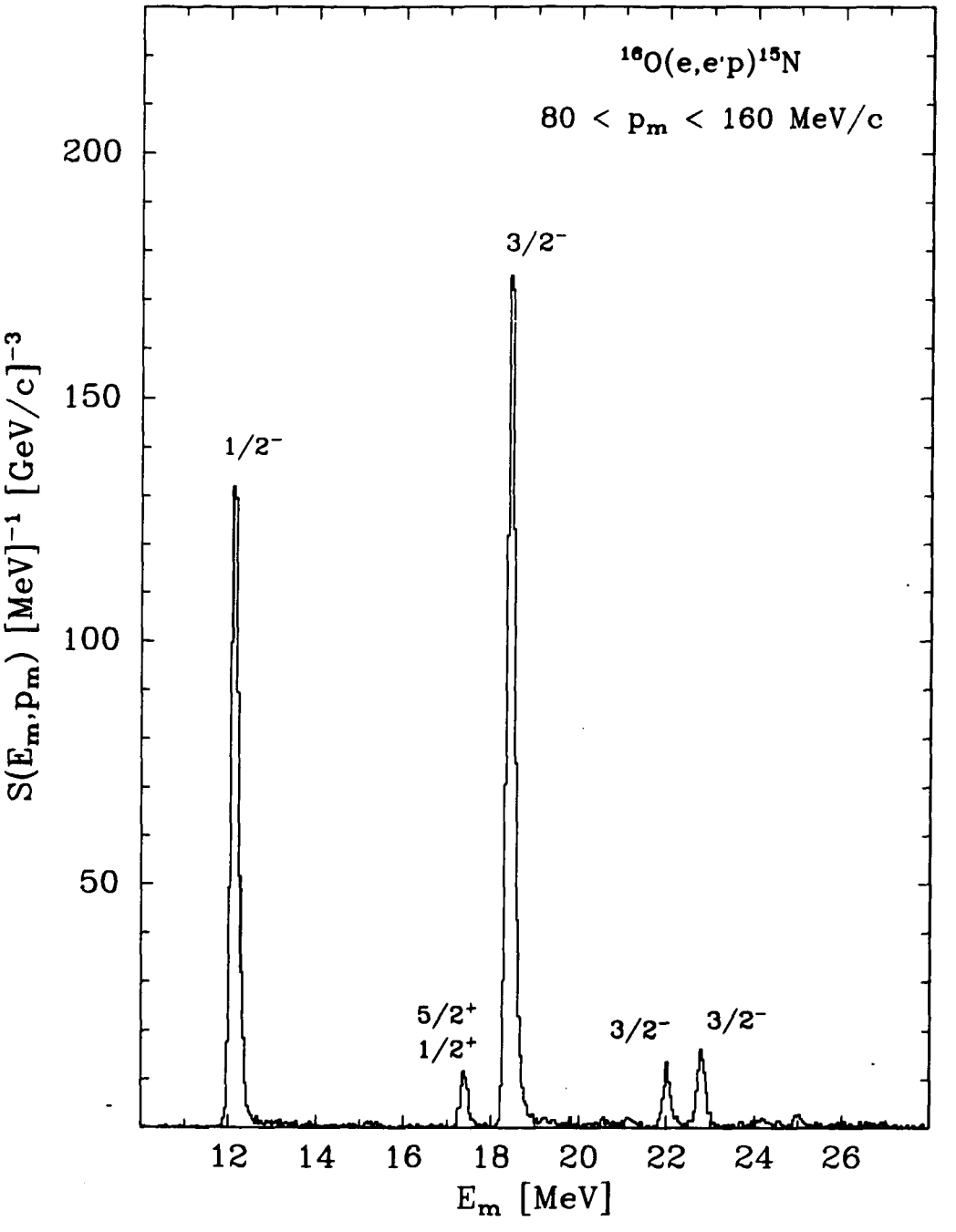


**Figure 10** Missing energy spectrum of the $^{16}$O(e,e'p)$^{15}$N reaction for the kinematics centered about $p_m$ = 120 MeV/c.

which have undergone radiative processes is folded back into the proper ($E_m$,$p_m$) bin. The unfolding procedure utilized for the present analysis, which accounts for Bremsstrahlung and ionization processes, is described in detail by E. Quint.[29]

## 3.3 Summary

For the present experiment we have measured the $^{16}$O spectral function in the range $0 < E_m < 40$ MeV and $-180 < p_m < 270$ MeV/c. The sign of the missing momentum refers to the projection of the initial nucleon momentum along the direction of the momentum transfer. In Figure 10 a missing energy spectrum of the reaction $^{16}$O(e,e'p)$^{15}$N is shown for the kinematics centered about $p_m$ = 120 MeV/c. The spectrum is dominated by two peaks at $E_m$ = 12.1 MeV and $E_m$ = 18.4 MeV, corresponding to proton knockout from the valence $1p$ orbitals in $^{16}$O. The peak at a missing energy of 12.1 MeV represents the minimal energy needed to remove a single proton from the $^{16}$O nucleus (from the least bound $1p_{1/2}$ orbital) and to leave the residual $^{15}$N nucleus in its ground state. Hence the missing energy of the $^{16}$O spectral function is offset from the $^{15}$N excitation spectrum by 12.1 MeV. The missing energy resolution obtained for the experiment varied between 150 keV and 200 keV for the different kinematics. Due to this excellent resolution the excitation of the $^{15}$N positive parity doublet at $E_x$ = 5.3 MeV ($E_m$ = 17.4 MeV) is also clearly evident. The momentum distribution can be calculated for each discrete state in the spectral function by integrating over the missing energy interval of interest (see expression (2.15)).

# 4. Data Analysis and Results

In this chapter we discuss the analysis of the $^{16}$O spectral function in the distorted wave impulse approximation. The first section describes the derivation of the optical potentials which were used to describe the distortions of the knocked out proton wave function. In section 2 the results of the DWIA analysis of the $1p$ momentum distributions are discussed, and in section 3 the DWIA analysis of the weak transitions is presented. Corrections for coupled channels effects are discussed in section 4, and in section 5 we present the results of a search for $7/2^+$ strength in the $^{16}$O spectral function. In section 6 the results of a multipole decomposition of the $^{16}$O spectral function are presented, and in the final section the results of the present analysis are compared to results from other experiments.

## 4.1 Derivation of the Optical Potential

Distortions of the knocked out proton wave function required for the DWIA analysis were calculated using five different optical potentials. Three of the optical potentials were phenomenological Woods-Saxon parameterizations. Of these, two were derived directly from elastic $^{16}$O(p,p$'$) data taken at an incident lab energy of 100 MeV.[30] The elastic cross section and analyzing power were fit[31] with a Woods-Saxon potential (WS) containing real, imaginary, and spin-orbit terms. A second potential (WS$_{dd}$) which included two additional derivative terms in the central potential was also used to fit the (p,p$'$) data. The center of mass kinetic energy of 90 MeV for the current (e,e$'$p) experiment corresponds to an equivalent incident proton lab energy of 96 MeV. The difference between the elastic (p,p$'$) cross section at 96 and 100 MeV was assumed to be small, so that the proton distortions in the $^{16}$O(e,e$'$p) reaction are sufficiently well characterized by the optical potential derived from the available 100 MeV $^{16}$O(p,p$'$) data.

The third Woods-Saxon optical potential (SC) was derived from the well known Schwandt parameterization.[32] Although the Schwandt parameterization is derived from nuclei in the range $24 < A < 208$, and is therefore not applicable to our case, we include it for the sake of comparison, since several other (e,e$'$p)

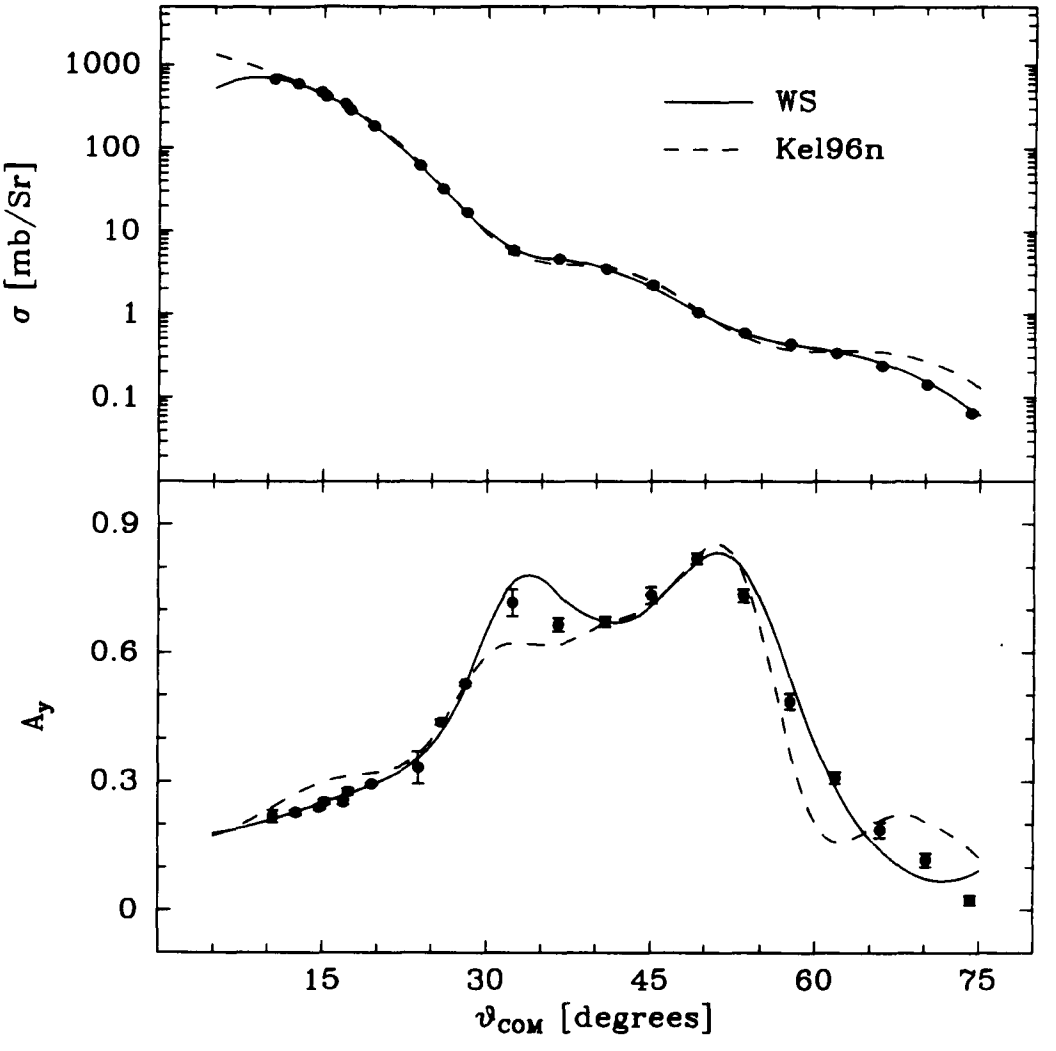


**Figure 11** Results of a Woods-Saxon potential fit to the elastic $^{16}$O(p,p′) cross section (top), and polarization asymmetry (bottom). The solid curves represent the fit due to the WS potential, while the dashed curves represent the Kel96n potential.

analyses have used the same parameterization to extract spectroscopic results. The Schwandt optical model parameterization is known to provide a good description of the systematics of elastic (p,p′) scattering data over a large range of target mass and incident proton beam energy. The parameters for the three

| potential | | V | $V_d$ | W | $W_d$ | $V_{so}$ | $W_{so}$ |
|---|---|---|---|---|---|---|---|
| SC | strength [MeV] | 28.359 | — | 6.876 | — | 4.808 | -0.869 |
| | radius [fm] | 1.255 | — | 1.434 | — | 0.997 | 0.968 |
| | diffuseness [fm] | 0.703 | — | 0.545 | — | 0.660 | 0.620 |
| WS | strength [MeV] | 29.121 | — | 10.052 | — | 3.181 | -0.707 |
| | ± | 0.708 | | 0.528 | | 0.186 | 0.061 |
| | radius [fm] | 1.101 | — | 1.412 | — | 0.934 | 1.620 |
| | ± | 0.015 | | 0.010 | | 0.005 | 0.015 |
| | diffuseness [fm] | 0.723 | — | 0.484 | — | 0.442 | 0.488 |
| | ± | 0.005 | | 0.017 | | 0.016 | 0.035 |
| $WS_{dd}$ | strength [MeV] | 27.932 | 0.820 | 10.077 | -0.309 | 3.010 | -0.722 |
| | ± | 0.111 | 0.112 | 0.377 | 0.156 | 0.146 | 0.050 |
| | radius [fm] | 1.087 | 0.988 | 1.414 | 1.150 | 0.940 | 1.604 |
| | ± | 0.007 | 0.025 | 0.016 | 0.045 | 0.006 | 0.014 |
| | diffuseness [fm] | 0.718 | 0.849 | 0.509 | 1.375 | 0.424 | 0.527 |
| | ± | 0.021 | 0.261 | 0.020 | 0.357 | 0.015 | 0.046 |

**Table 3** The optical model parameters for the Schwandt[32] (SC) and Woods-Saxon (WS and $WS_{dd}$) potentials. The Woods-Saxon potentials were derived from fits to elastic $^{16}O(p,p')$ data taken at an incident proton lab energy of 100 MeV.

Woods-Saxon potentials are listed in Table 3. It can be seen that the Schwandt potential parameters agree quite well with those obtained from the elastic $(p,p')$ fits.

In addition to the three Woods-Saxon parameterizations, two optical potentials were supplied by Kelly.[33] These potentials were derived from an effective density dependent nucleon-nucleon interaction which was fit to the *inelastic* states of $^{16}O$ in the Local Density Approximation. The first potential (Kel100o) was fit to the available proton scattering data at 100 MeV in lab frame (the same data that determined the WS and $WS_{dd}$ potentials discussed above). The second potential

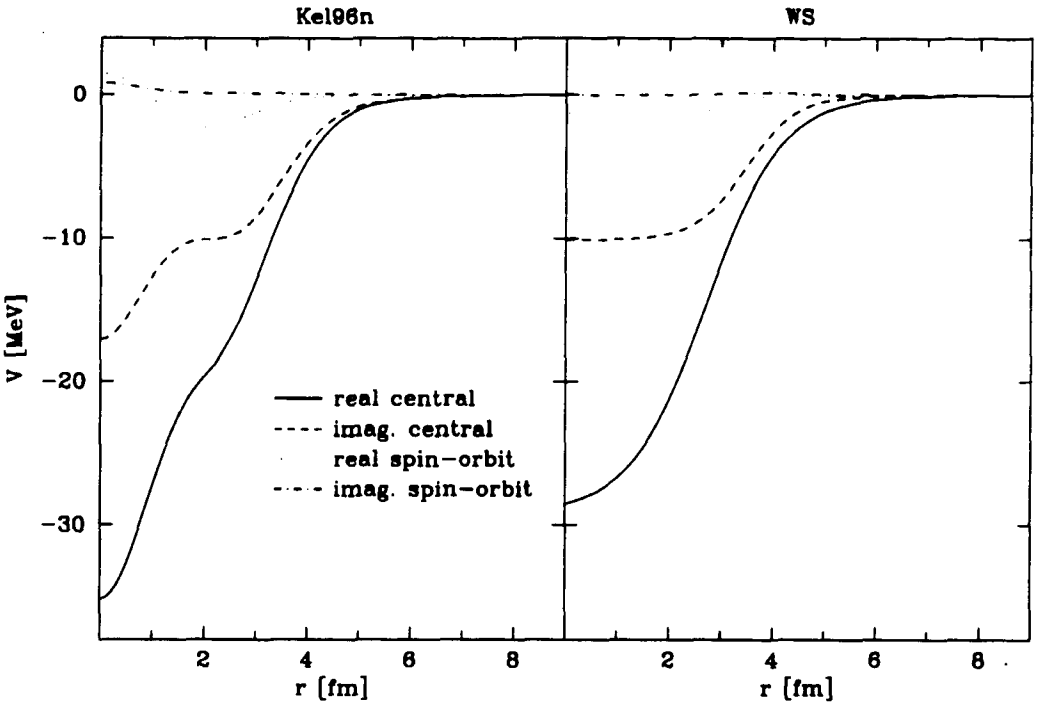


**Figure 12** The Kel96n and WS optical potentials.

(Kel96n) was extrapolated[30] to the case of 90 MeV in the center of mass, in order to correspond to the actual kinematics of the present $^{16}$O(e,e'p) experiment. The Kel96n and WS potentials are shown in Figure 12. The main qualitative difference between the Kelly and Woods-Saxon potentials is the additional structure found in the Kelly potential, where the upward slope of the central potential is seen to decrease at radii between 2 and 3 fermi. We have attempted to incorporate the additional structure of the Kelly potential into a Woods-Saxon parameterization by including two derivative terms in the central potential. The results of fit to the elastic (p,p') data using the new potential improves the phenomenological description of the experimental cross section and analyzing power ($\chi^2$ is reduced by 21%), although the strength of the derivative terms is insufficient to create the additional structure seen in the Kelly potentials.

## 4.2 DWIA ANALYSIS OF THE 1$p$ TRANSITIONS

The momentum distributions for 1$p$ proton knockout from $^{16}$O leading to final states in $^{15}$N were calculated according to equation (2.15). The experimental spectral function was sorted into bins of width $\Delta E_m$ = 40 keV and $\Delta p_m$ = 5 MeV/c. For each missing momentum bin, the strength under the 1$p$ peaks in the associated missing energy spectrum was integrated. Bins for which the detection volume weight was less than 25% of the maximum weight were omitted from the momentum distribution.

DWIA fits of the momentum distributions for each of the two strong 1$p$ states were performed. The bound state wave function of the orbital, $\phi_\alpha$ (see equation (2.14)), was calculated in a Woods-Saxon well with diffuseness $a$ = 0.65. The range parameter[22] of the bound state non-locality correction was held constant at $\beta$ = 0.85. To fit the momentum distribution the *rms* radius of the wave function, $r_{rms}$, and the spectroscopic factor $S_\alpha$ were adjusted. The remaining Woods-Saxon parameter, the well depth, was held constant at the value required to reproduce the experimentally observed separation energy of the bound final state. These fits were performed for each of the five optical potentials.

The final fitted DWIA results for the two strong 1$p$ transitions are shown in Figure 13. The extracted spectroscopic factors and *rms* radii for each state and each potential are listed in Table 4. All five potentials yield excellent fits for both states. The spectroscopic factors obtained from the current experiment are in general agreement with those of the previous $^{16}$O(e,e'p) experiment of Bernheim *et al.*, in which spectroscopic factors of 1.18(15) and 2.28(29) were reported for the $1p_{1/2}$ ground state and $1p_{3/2}$ third excited state respectively. The spectroscopic factor for the $1p_{1/2}$ ground state extracted from the Saclay data is 6% smaller than the average value of 1.25 obtained from the present analysis, while the extracted $1p_{3/2}$ spectroscopic factors differ only slightly ($< 1\%$) between the two experiments.

As Table 4 indicates, the consistency among the fitted parameters between the five potentials is excellent for the $1/2^-$ ground state transition, while the

| | | | $p_m > 0$ | | | all $p_m$ | | |
|---|---|---|---|---|---|---|---|---|
| state $J^\pi$ | $E_x$ MeV | potential | radius fm | $S_\alpha$ | $\chi^2$/d.f. | radius fm | $S_\alpha$ | $\chi^2$/d.f. |
| $1/2^-$ | 0.00 | WS | 2.918(32) | 1.261(13) | 0.64 | 2.898(31) | 1.275(18) | 0.72 |
| | | $WS_{dd}$ | 2.928(33) | 1.230(16) | 0.70 | 2.906(36) | 1.242(17) | 0.77 |
| | | SC | 2.828(31) | 1.222(11) | 0.60 | 2.835(30) | 1.220(11) | 0.57 |
| | | Kel96n | 2.958(31) | 1.249(18) | 0.63 | 2.943(30) | 1.260(13) | 0.67 |
| | | Kel100o | 2.991(31) | 1.221(13) | 0.67 | 2.970(29) | 1.234(16) | 0.85 |
| $3/2^-$ | 6.32 | WS | 2.775(21) | 2.047(14) | 1.16 | 2.771(20) | 2.059(16) | 0.98 |
| | | $WS_{dd}$ | 2.778(47) | 1.980(15) | 1.27 | 2.784(22) | 1.983(16) | 1.07 |
| | | SC | 2.677(21) | 2.132(14) | 0.66 | 2.680(19) | 2.132(12) | 0.69 |
| | | Kel96n | 2.727(25) | 2.339(18) | 0.70 | 2.719(24) | 2.348(19) | 0.72 |
| | | Kel100o | 2.793(23) | 2.232(15) | 0.77 | 2.805(15) | 2.215(12) | 0.92 |

**Table 4** Spectroscopic results for $^{16}$O proton knockout leading to the $1p_{1/2}$ $^{15}$N ground state and the $1p_{3/2}$ state at $E_x = 6.3$ MeV.

spectroscopic factors for the $3/2^-$ state at $E_x = 6.3$ MeV differ by almost 20% between the extreme values. A possible explanation of the discrepancy between the $1p_{3/2}$ spectroscopic factors lies in the observation that the spectroscopic results can be roughly categorized into two groups according to the manner in which the optical potential was calculated. On one hand, the results from the the WS and $WS_{dd}$ potential, which were both derived from *elastic* (p,p′) data, agree to within a few percent. The results from the two Kelly potentials, which were derived explicitly from *inelastic* (p,p′) data, are also close to one another. The magnitude of the spectroscopic factor due to the Schwandt parameterization falls between the first two groups. This would imply that the major discrepancy concerns results which were derived using optical potentials which describe elastic (p,p′) data, and optical potentials which describe inelastic (p,p′) data.

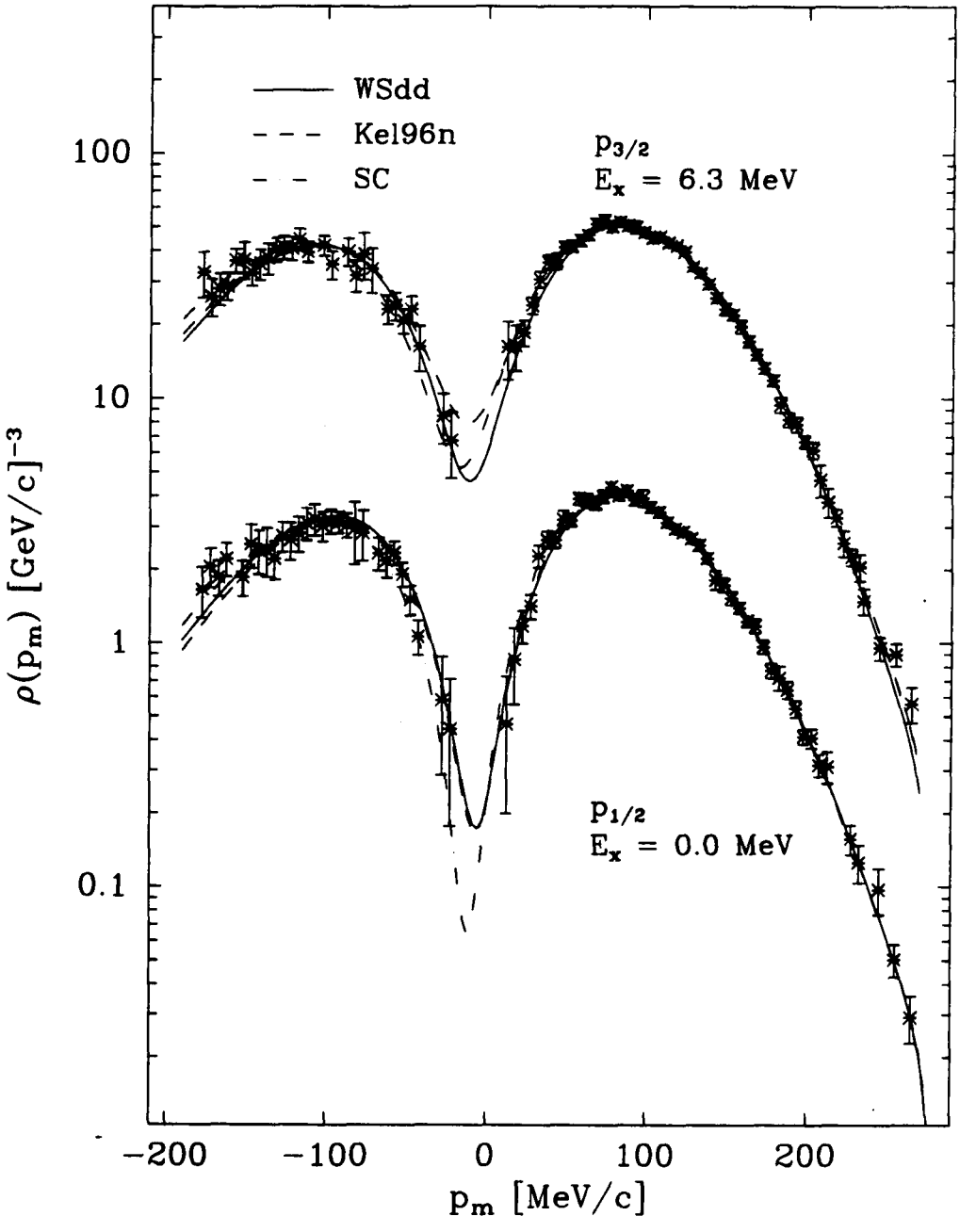


**Figure 13** The momentum distribution for $1p_{1/2}$ ground state (bottom) and the $1p_{3/2}$ state (top) at $E_x$ = 6.3 MeV. The curves represent DWIA fits using three different optical potentials.

| potential | $N_{vso}$ | $N_{wso}$ | radius (fm) | $S_\alpha$ | $\chi^2$/d.f. |
|---|---|---|---|---|---|
| WS | 2.09(17) | 1.98(70) | 2.708(4) | 2.245(17) | 0.67 |
| $WS_{dd}$ | 2.38(14) | 2.30(55) | 2.704(2) | 2.207(17) | 0.69 |
| SC | 1.14(11) | -0.09(56) | 2.682(2) | 2.196(16) | 0.66 |
| Kel96n | 0.99(3) | 2.54(71) | 2.735(6) | 2.299(17) | 0.68 |
| Kel100o | 1.14(3) | 3.67(68) | 2.765(2) | 2.184(16) | 0.72 |

**Table 5** $1p$ proton knockout from $^{16}$O, with adjustable spin-orbit strengths.

Since the knockout of a proton from the $1p_{3/2}$ orbital in $^{16}$O leaves the residual $^{15}$N nucleus in a highly excited state, there is some question as to whether the optical potential of the excited $^{15}$N nucleus is sufficiently similar to that of the ground state nuclear configuration. The variation between the present $1p_{3/2}$ spectroscopic results using different optical potentials suggests that the (e,e'p) reaction is indeed very sensitive to the details of the optical potential.

A second possible source of the $1p_{3/2}$ spectroscopic factor discrepancy lies in the observation that the ground state $1p_{1/2}$ level, for which all of the potentials yield spectroscopic factors in agreement with one another, and the $1p_{3/2}$ level are spin-orbit partners. This observation leads to the suspicion that the spin-orbit contribution to the optical potential may be the source of the discrepancies. To investigate this possibility we have performed a study of the sensitivity of the $1p_{3/2}$ momentum distribution to the spin-orbit strength of the optical potential. We have fit the $1p$ momentum distributions by adjusting $r_{rms}$ and $S_\alpha$, as above, and in addition we have applied an adjustable normalization factor to the real ($N_{vso}$) and imaginary ($N_{wso}$) spin-orbit strengths. The results of this investigation, listed in Table 5, are revealing. The adjustment of the spin-orbit strengths leads to an average $\chi^2$ reduction of 20%, indicating a strong sensitivity to the spin-orbit potential. The fits to the momentum distribution using the Woods-Saxon potentials yielded the most significant reductions in $\chi^2$ – 32% for the WS potential and 36% for the $WS_{dd}$ potential. These fits also resulted in a conver-

gence of the $1p_{3/2}$ spectroscopic factors, which had previously differed by 20%, to a difference of only 5%.

We note that the magnitude of the changes in the spin-orbit strengths required by the above analysis are disallowed by the 100 MeV $^{16}$O(p,p') data, since the normalization factors represent changes of about 20 standard deviations, on the average, from the extracted parameters of the (p,p') analysis listed in table 3. Nonetheless, the sensitivity of the (e,e'p) spectroscopic results makes it clear that further constraints must be identified and applied to the selection of the optical potential. In the absence of such constraints we are unable to determine the spectroscopic factor of the $1p_{3/2}$ orbital to better than a 20% uncertainty, not including the statistical (0.8%) and systematic (5.5%) uncertainties, because we cannot distinguish between the optical potentials based on the agreement of theoretical calculations with experimental data. For the present analysis we have seen that five optical potentials, each of which simultaneously describes the shapes of the elastic proton scattering data, the $1p_{1/2}$ momentum distribution, and the $1p_{3/2}$ momentum distribution, give different spectroscopic results for the $1p_{3/2}$ transition.

The $1p$ momentum distributions were measured in the range $-180 < p_m < 270$ MeV/c. If the spectral function is interpreted in terms of the PWIA, then the negative missing momentum data supply only redundant information. The spectral function in the PWIA interpretation reflects the probability of finding a proton in a given energy and momentum state, which must be independent of any preferred direction in space (with an unpolarized target) such as the momentum transfer. An analysis of only the positive missing momentum data should therefore yield the same spectroscopic information as that of the complete missing momentum distribution. Table 4 lists the results of the DWIA analysis when only the positive missing momentum data are considered, as well as the results for the complete $p_m$ distribution. It can be seen that the agreement between the fit with all missing momentum data and the fit with only positive missing momentum data is excellent for all five of the optical models considered, thus confirming the validity of

the spectral function interpretation of the momentum distribution.

Previous (e,e'p) studies[10,28] of the $^{16}$O and $^{12}$C nuclei have noted an anomalous enhancement of the experimental $1p$ momentum distributions, relative to the DWIA calculation, in the region $p_m < 0$. Both studies observed an asymmetry in the momentum distribution about $p_m = 0$ which could not be resolved by using alternative descriptions of the optical potential. In the case of $^{12}$C(e,e'p) this asymmetry was modeled by introducing an anomalous enhancement factor, $\eta$, to the transverse response function. To motivate such an approach it was noted that the kinematics for the negative missing momenta required a more backward electron angle, and hence a more transversely polarized virtual photon. It is precisely in this region that reaction mechanisms not included in the DWIA, such as meson exchange currents, are likely to contribute to the observed cross section.

The present $^{16}$O(e,e'p) data are well described by the conventional DWIA treatment for both sides of the $1p$ momentum distributions, for each of the five optical potentials considered. The quality of the fit, as evidenced by the $\chi^2$ values listed in Table 4, does not suffer with the inclusion of the data at $p_m < 0$. Furthermore, the extracted values of $r_{rms}$ and $S_\alpha$ do not depend on whether or not the $p_m < 0$ data is included in the fit.

Despite the lack of overt evidence for anomalous transverse behavior, we have performed an analysis analogous to that of van der Steenhoven[28] in order to determine the range of $\eta$ values allowed by our data. The values of $r_{rms}$ and $S_\alpha$, along with the additional parameter $\eta$, were adjusted to obtain the best agreement between the theoretical and experimental $1p$ momentum distributions. For the $1p_{3/2}$ state an average result of $\eta = 1.04 \pm 0.15$ was obtained between the five optical potentials, while the average value for the $1p_{1/2}$ ground state was $\eta = 1.05 \pm 0.17$. The effect of the $\eta$ enhancement factor on the spectroscopic factors was less than 3% in all cases. In conclusion, the present $^{16}$O(e,e'p) data excludes the possibility of anomalous transverse behavior at the level reported by van der Steenhoven *et al.* for $^{12}$C.

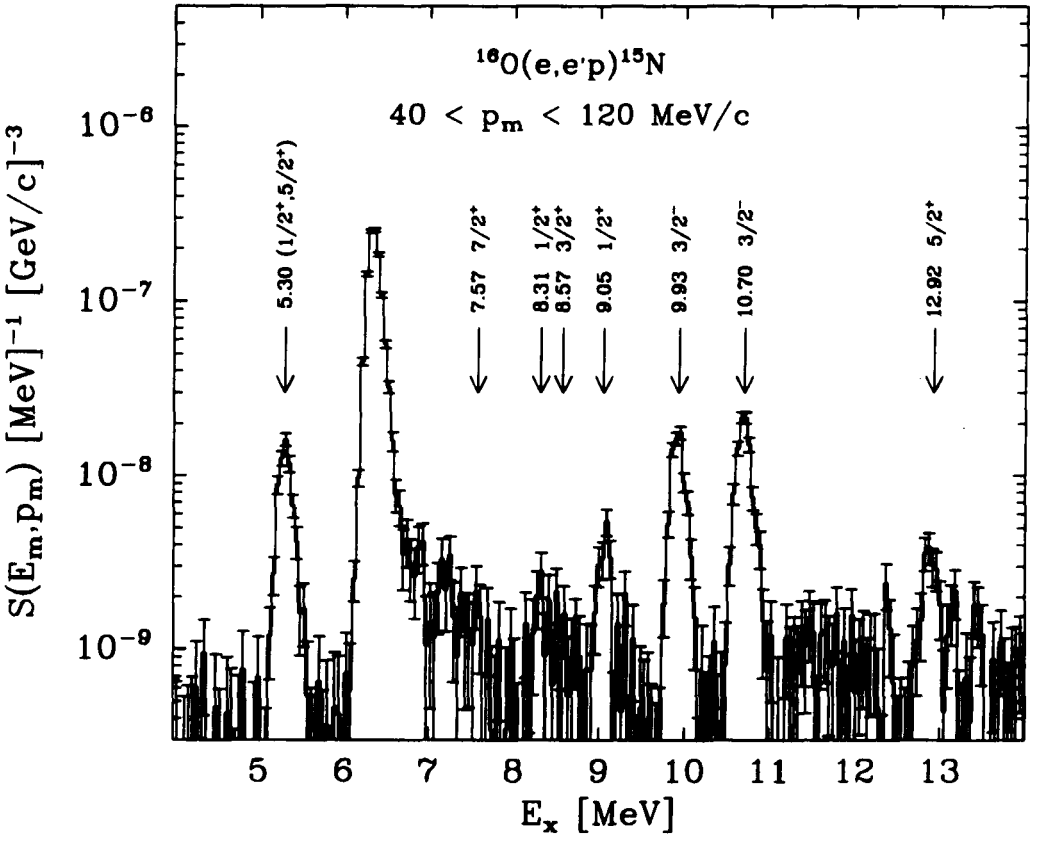


**Figure 14** Missing energy spectrum of the $^{16}$O(e,e'p)$^{15}$N reaction for the kinematics centered about $p_m$ = 80 MeV/c.

### 4.3 DWIA ANALYSIS OF THE WEAK TRANSITIONS

The weak positive parity states at $E_x$ = 5.3 MeV in $^{15}$N are of particular interest for determining the structure of $^{16}$O. The DWIA analysis of these states is complicated somewhat because they are not resolved in missing energy, since the 30 keV separation energy between the two states is considerably less than the experimental resolution of 150-200 keV. However, because the two states differ in their angular momentum, a separation in missing momentum can easily be performed. The momentum distribution for this doublet is shown in Figure 15.

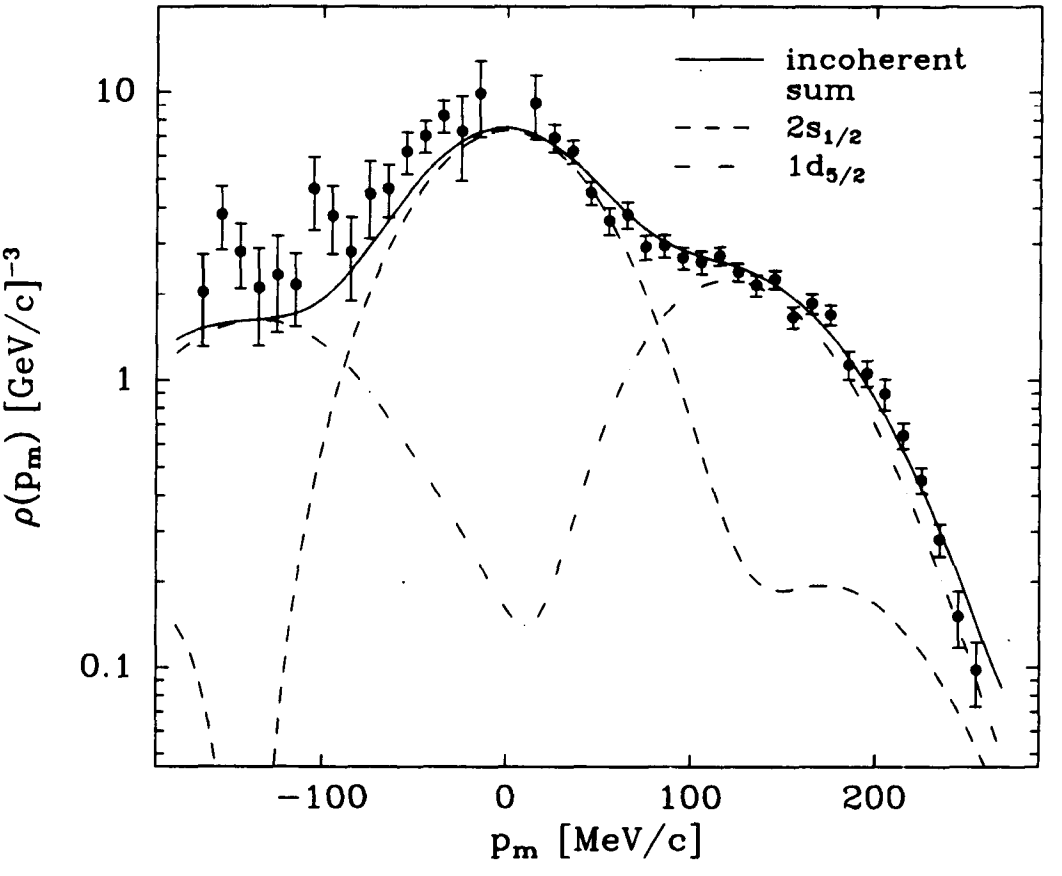


**Figure 15** The momentum distribution for the positive parity doublet at $E_x$ = 5.3 MeV. The curves represent the DWIA fit using the Kel96n potential.

In order to extract the *rms* radii and spectroscopic factors the 2*s*1*d* momentum distribution was fit with an incoherent sum of $2s_{1/2}$ and $1d_{5/2}$ momentum distributions. The radii and spectroscopic factors of each state were allowed to vary independently. The extracted spectroscopic results for these states are listed in Table 6 for each of the five optical potentials considered. The results due to the Kel96n potential indicate a spectroscopic factor of $0.0357 \pm 0.0015$ for the $2s_{1/2}$ orbital, while the spectroscopic factor of the $1d_{5/2}$ state was found to be $0.1140 \pm 0.0032$. This impressive accuracy reflects the precision of the (e,e'p) reaction as a probe of partially occupied nuclear orbitals.

| potential | $R_{1/2}$ fm | $R_{5/2}$ fm | $S_{1/2}$ | $S_{5/2}$ | $\chi^2$/d.f. |
|---|---|---|---|---|---|
| WS | 3.294(93) | 3.578(4) | 0.0342(14) | 0.0966(27) | 1.81 |
| $WS_{dd}$ | 3.287(94) | 3.594(4) | 0.0338(14) | 0.0929(26) | 1.80 |
| SC | 3.254(66) | 3.478(3) | 0.0376(15) | 0.1033(30) | 1.46 |
| Kel96n | 3.305(37) | 3.495(4) | 0.0357(15) | 0.1140(32) | 1.80 |
| Kel100o | 3.361(138) | 3.543(3) | 0.0350(15) | 0.1128(32) | 1.75 |

**Table 6** Spectroscopic factors and *rms* radii for $^{16}$O proton knockout leading to the $2s_{1/2}$ state at $E_x = 5.30$ and the $1d_{5/2}$ state at $E_x = 5.27$ MeV.

The sensitivity of the (e,e'p) reaction to small components of the $^{16}$O wave function is unfortunately obscured to a certain extent by the model dependence introduced by the optical potentials. The lack of agreement between the spectroscopic factors due to the different optical potentials, previously observed for the $1p_{3/2}$ state at $E_x = 6.3$ MeV, is also present for the results of the $E_x = 5.3$ MeV doublet. The spectroscopic factors for the $2s_{1/2}$ transition differ by 11% between extreme values, and the results for the $1d_{5/2}$ transition differ by 23%. These results support our earlier conclusion that the elastic (p,p') scattering data provides an insufficient constraint on the determination of the optical potential. The Kelly potentials yield spectroscopic results which are in excellent agreement with the Woods-Saxon potentials for the $1p_{1/2}$ ground state, while they have the added advantage that they are constrained by the inelastic $^{16}$O(p,p') scattering data. Therefore, we consider this potential (Kel96n) to be the best suited for the $^{16}$O(e,e'p)$^{15}$N analysis, especially for states at higher missing energies.

We have interpreted the population of the $1/2^+$ state at $E_x = 5.30$ MeV as arising from proton knockout from the $2s_{1/2}$ orbital of $^{16}$O. This assumption is mainly due to the low separation energy for the $1/2^+$ state, which is less than the separation energy for the $1p_{3/2}$ orbital (6.3 MeV). Since proton knockout from the $1s_{1/2}$ orbital can also contribute to the population of $1/2^+$ states in $^{15}$N, we

have repeated the analysis of the positive parity doublet by replacing the $2s_{1/2}$ momentum distribution with a $1s_{1/2}$ momentum distribution. The extracted *rms* radius for the $1s_{1/2}$ wave function was $R_{s1/2} = 3.49 \pm 0.32$, and the depth of the Woods-Saxon well required to reproduce the separation energy for this state was 27 MeV. In view of the unrealistically large radius and unphysically small well depth extracted from this analysis, the present data indicates that the $1/2^+$ state at $E_x = 5.30$ MeV is populated by knockout from the $2s_{1/2}$ orbital of $^{16}O$.

Momentum distributions for a total of 10 states have been extracted from the spectral function in the region $E_m < 25$ MeV. Excitation energies and spin/parity assignments for these states are listed in Table 7, along with the spectroscopic results obtained from the DWIA analysis. The results listed in Table 7 are those obtained from the DWIA analysis employing the Kelly (Kel96n) potential. The statistical accuracy of the momentum distributions for most of the weak states was not sufficient for a meaningful comparison of spectroscopic results between the five optical potentials employed in the analysis of the first four $^{15}N$ states.

The angular momentum assignments for the discrete states have been determined from the location of the peak in the missing momentum distribution. The peak contribution from each multipole is located at a unique missing momentum: at $p_m = 0$ MeV/c for $l = 0$ knockout, at about $p_m = 80$ MeV/c for $l = 1$, and at about $p_m = 120$ MeV/c for $l = 2$ knockout. As we discussed above, the DWIA analysis of the positive parity double at $E_x = 5.3$ MeV was possible because the dominant contribution to the momentum distribution from each multipole occurs 120 MeV/c apart from one another. The experimental missing momentum resolution was about 2 MeV/c for the present experiment. The data do not allow us to distinguish between the two total angular momentum states ($j = l \pm 1/2$), although it was possible to make a spin and parity assignment for each discrete state from it's location in the missing energy spectrum. All of the discrete states are sufficiently isolated in missing energy from other states with the same orbital angular momentum[34] to allow for an unambiguous assignment of the $j$ component of the total angular momentum.

| $E_x$ MeV | $J^\pi$ | $S_\alpha$ | radius fm |
|---|---|---|---|
| 0.00 | $1/2^-$ | 1.260(13) | 2.943(30) |
| 5.27 | $5/2^+$ | 0.1140(32) | 3.495(4) |
| 5.29 | $1/2^+$ | 0.0357(15) | 3.305(37) |
| 6.32 | $3/2^-$ | 2.348(19) | 2.719(24) |
| 7.57 | $7/2^+$ | 0.0023(25) | 3.500 |
| 8.31 | $1/2^+$ | 0.0411(28) | 1.813 |
| 8.57 | $3/2^+$ | 0.0210(28) | 2.842(242) |
| 9.05 | $1/2^+$ | 0.0418(38) | 1.813(394) |
| 9.93 | $3/2^-$ | 0.133(15) | 2.863(68) |
| 10.70 | $3/2^-$ | 0.222(4) | 2.700(52) |
| 12.10 | $5/2^+$ | 0.0225(18) | 3.334(209) |
| 12.92 | $3/2^-$ | 0.0347(23) | 2.728(207) |

**Table 7** Spectroscopic factors and *rms* radii for the discrete states observed in the $^{16}O(e,e'p)^{15}N$ reaction. The results were extracted from the DWIA analysis using the Kel96n optical potential.

Three $l = 0$ states at $E_x = 5.30, 8.31,$ and 9.05 MeV have been identified in the $^{16}O(e,e'p)^{15}N$ spectral function. The strength of the $E_x = 5.3$ MeV state has been determined to arise from the knockout of $2s_{1/2}$ protons, hence the nuclear overlap integral was replaced by a single $2s_{1/2}$ bound state wave function as indicated in expression (2.14). For the DWIA analysis of the other two $1/2^+$ states we have generalized the form of expression (2.14) to a coherent sum of $1s_{1/2}$ and $2s_{1/2}$ bound state wave functions, since in general both orbitals can contribute to the observed cross section. We have also performed the analysis of each state using pure $1s_{1/2}$ and $2s_{1/2}$ contributions to the overlap integral. The results of the analysis of the $1/2^+$ states are summarized in Table 8. The dependence of the spectroscopic factor and $\chi^2$ on the amplitude of the $2s_{1/2}$ component of the overlap integral is illustrated in figure 16. For the 8.31 MeV state the data show

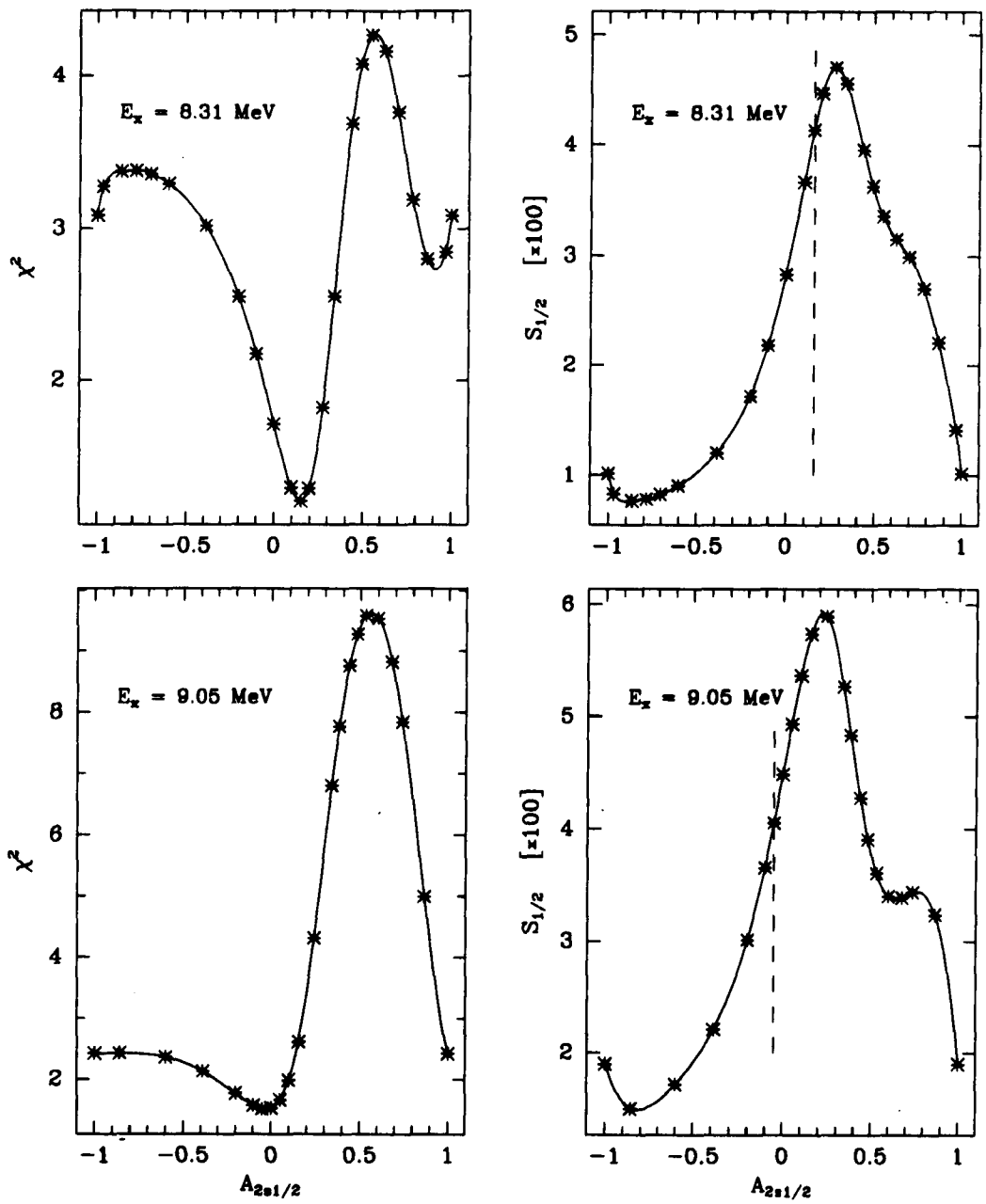


**Figure 16** Dependence of $\chi^2$ (left) and the spectroscopic factor (right) on the amplitude of the $2s_{1/2}$ component of the overlap integral for the $1/2^+$ states at $E_x$ = 8.31 MeV (top) and $E_x$ = 9.05 MeV (bottom). The vertical dashed lines coincide with the location of the $\chi^2$ minima.

| $E_x$ MeV | $A_{1s1/2}$ | $A_{2s1/2}$ | $S_\alpha$ | $\chi^2$ |
|---|---|---|---|---|
| 8.31 | 1.0 | 0.0 | 0.0283(20) | 1.71 |
| 8.31 | 0.0 | 1.0 | 0.0101(10) | 3.09 |
| 8.31 | 0.989 | 0.151(33) | 0.0411(28) | 1.20 |
| 9.05 | 1.0 | 0.0 | 0.0448(22) | 1.53 |
| 9.05 | 0.0 | 1.0 | 0.0190(10) | 2.42 |
| 9.05 | 0.999 | -0.021(41) | 0.0418(38) | 1.51 |

**Table 8** Spectroscopic factors for the $1/2^+$ states at $E_x = 8.31$ MeV and $E_x = 9.05$ MeV.

a preference for the $1s_{1/2}$ overlap, although the coherent addition of a small $2s_{1/2}$ component is seen to improve the description of the momentum distribution. For the 9.05 MeV state the data show a strong preference for the $1s_{1/2}$ form of the overlap integral. The extracted amplitude for the $2s_{1/2}$ component is consistent with zero. In addition, the analysis of this state using the pure $2s_{1/2}$ configuration leads to an unrealistically small value for the *rms* radius of the bound state wave function ($r_{rms} = 2.5$ fm.). The results indicate that the dominant contribution of the (e,e'p) reaction leading to the $E_x = 9.05$ MeV state arises from $1s_{1/2}$ knockout.

The momentum distributions of the three states at $E_x = 9.93, 10.70$, and 12.92 MeV are all clearly $l = 1$ in character. The extracted *rms* radii for these states are all in good agreement with that of the dominant $1p_{3/2}$ fragment at $E_x = 6.3$ MeV, although the radius of the $3/2^-$ state at $E_x = 9.93$ MeV is slightly larger. This is probably due to an unresolved admixture of $1d$ strength, which causes an enhancement of the $1p$ momentum distribution at higher missing momenta. The results of a multipole decomposition, discussed in section 4.6, are consistent with this observation.

Although we are unable to distinguish between $1d_{5/2}$ strength and $1d_{3/2}$ strength in the $^{16}O$ spectral function, we are able to exploit the low density of

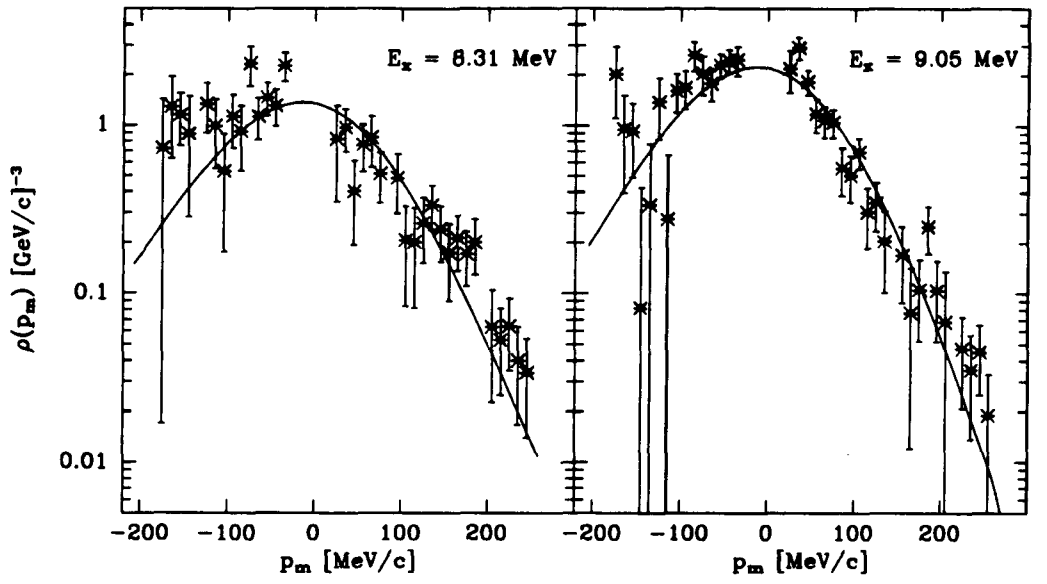


**Figure 17** Momentum distribution for the weak $l = 0$ states at $E_r = 8.31$ MeV and $E_r = 9.05$ MeV.

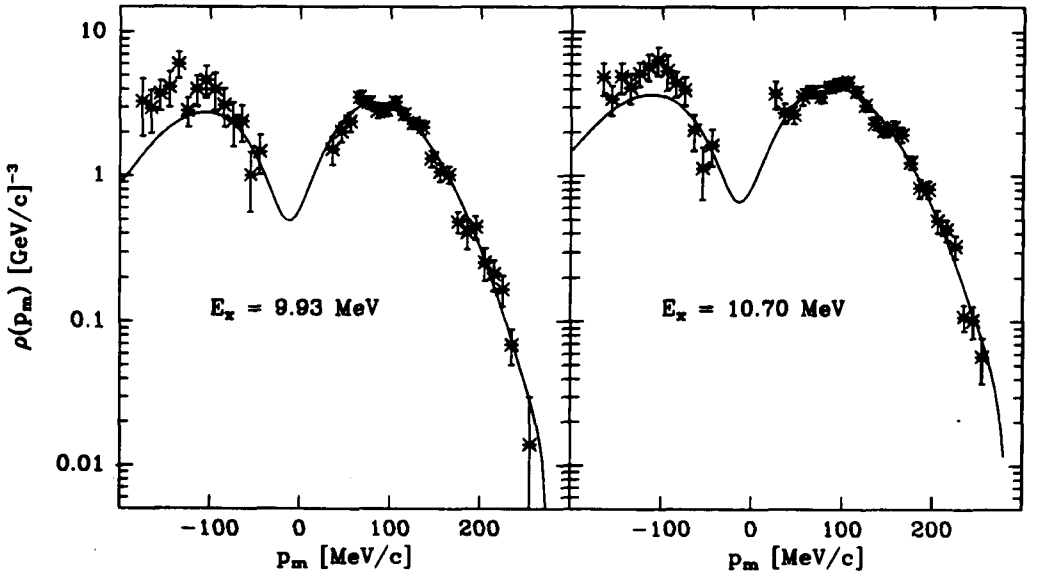


**Figure 18** Momentum distribution for the weak $l = 1$ states at $E_r = 9.93$ MeV and $E_r = 10.70$ MeV.

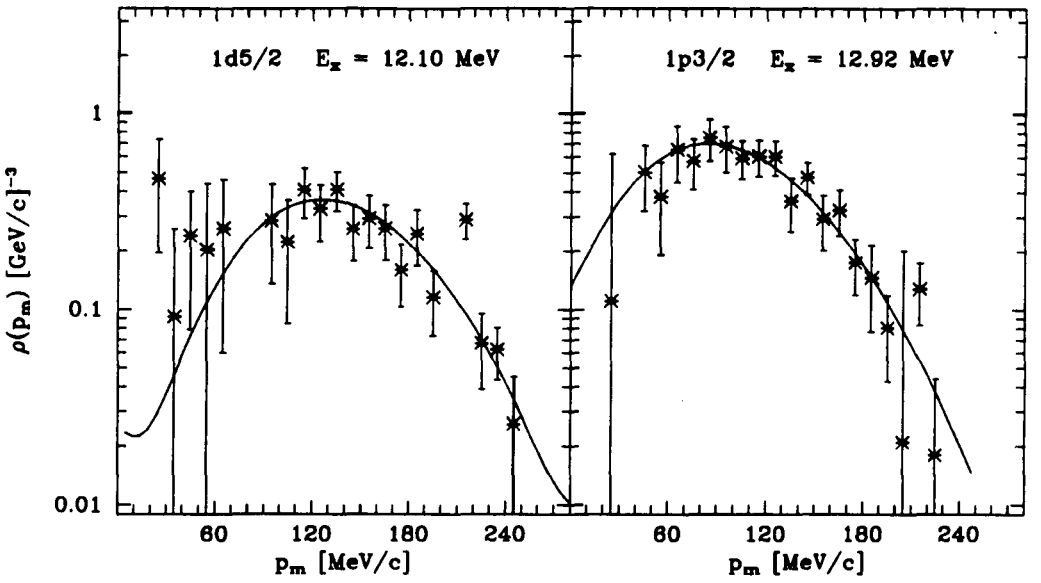


**Figure 19** Momentum distribution for the weak $1d_{5/2}$ state at $E_x = 12.10$ MeV and the $1p_{3/2}$ state at $E_x = 12.92$ MeV.

states in the $^{15}$N excitation spectrum to obtain a measurement of the $1d_{3/2}$ spectroscopic strength. There are only two states[34] in the excitation energy region $8 < E_x < 9$ MeV of the $^{15}$N spectrum. One, the $1/2^+$ state at $E_x = 8.31$ MeV ($E_m = 20.44$ MeV), has been resolved in the present experiment and its spectroscopic factor was extracted. The second state is a $3/2^+$ located at $E_x = 8.57$ MeV ($E_m = 20.70$ MeV). The superposition of the $1/2^+$ and $3/2^+$ momentum distributions was obtained by integrating the $^{16}$O spectral function over the region $20 < E_m < 21$ MeV. The spectroscopic factor and *rms* radius of the $3/2^+$ state was obtained by fitting an incoherent sum of $1s_{1/2}$ and $1d_{3/2}$ momentum distributions to the experimental momentum distribution. The results of this fit are shown in Figure 20. The spectroscopic factor extracted for the $1s_{1/2}$ component of the momentum distribution was $S_{1s1/2} = 0.0274(17)$, and the spectroscopic factor for the $1d_{3/2}$ component was $S_{d3/2} = 0.0210(28)$. The $1s_{1/2}$ spectroscopic is consistent with the value of $S_{1s1/2} = 0.0283(20)$ obtained from the discrete state analysis with a pure $1s_{1/2}$ amplitude. This agreement provides a confir-

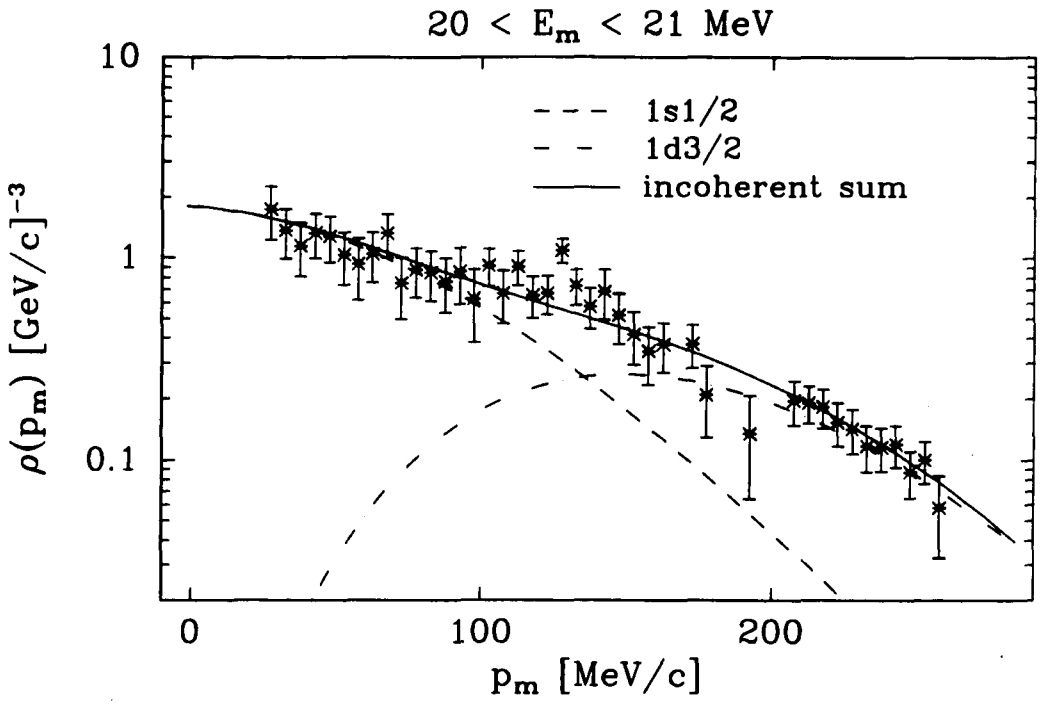


**Figure 20** The momentum distribution for the region $20 < E_m < 21$ MeV. The curves represent the DWIA fit using the Kel96n potential.

mation that there is no background contamination of the $20 < E_m < 21$ MeV momentum distribution, thereby allowing for the accurate extraction of the $1d_{3/2}$ spectroscopic factor.

### 4.4 CCIA Analysis

In the simplest model of the $^{16}$O nucleus the $1s$ and $1p$ shells are completely filled, while all other shells are empty. A consequence of this model is that the $5/2^+$ level at $E_x = 5.27$ MeV cannot be excited in a single step process via the (e,e'p) reaction. In order to confidently extract spectroscopic factors from weak transitions in the $^{16}$O(e,e'p)$^{15}$N reaction, the contribution to the momentum distribution due to two-step processes and coupled channels effects must be estimated. The observation of a significant $5/2^+$ strength can only be interpreted as an occupation of the $2s1d$ shell in $^{16}$O if a strong two-step process is absent.

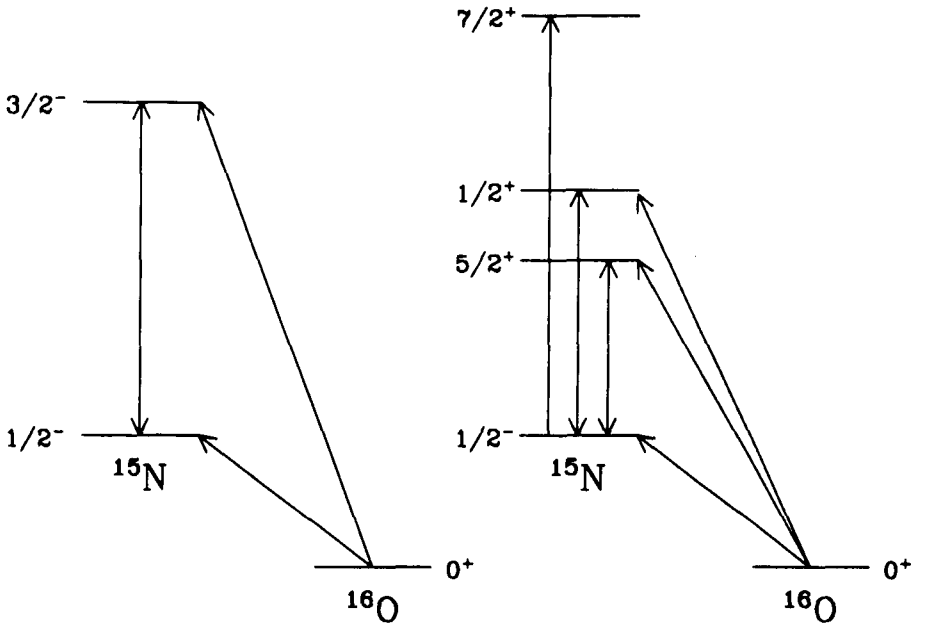


**Figure 21** Coupling scheme for CCIA calculation between the two $1p$ states (left) and the positive parity states (right) of $^{15}$N.

In the conventional DWIA analysis of (e,e'p) data, as outlined in the previous sections, the distortion of the outgoing proton wave is calculated in an optical potential. This treatment of the final state interaction does not account for the contribution to the cross section due to coupled channels effects in the final state. Previous calculations[28] of coupled channels effects for the $^{12}$C(e,e'p) reaction have shown that they can contribute appreciably to the cross section, in particular for parallel kinematics. We have calculated these effects for the $^{16}$O(e,e'p)$^{15}$N reaction according to the prescription previously employed by Blok *et al.*.[35,8] where the absorption of the virtual photon is simulated by the proton pickup of a fictitious light particle, whose mass and energy are chosen to reproduce the kinematics of the (e,e'p) reaction. The equivalence of the cross section calculated in the factorized DWIA (e,e'p) approach and this simulated pickup approach has been demonstrated.

Coupled channels impulse approximation (CCIA) calculations were performed for the $^{16}$O(e,e'p) reaction according to the coupling scheme illustrated in Figure 21. The coupling strength between the two $1p$ states ($\beta_2 = 0.177$) was obtained from a previous analysis of the $^{15}$N(p,p') reaction.[36] Similar coupling strengths for the positive parity doublet at $E_x = 5.3$ MeV in $^{15}$N, extracted from inelastic (p,p') data, were not available in the literature. In an previous analysis of the $^{16}$O(d,$^3$He)$^{15}$N reaction by Firestone *et al.*,[37] where coupled channels effects were also considered, it was reported that to a good approximation the $5/2^+$ state at $E_x = 5.27$ MeV in $^{15}$N can be regarded as a $1p_{1/2}$ hole coupled to the $3^-$ vibration at $E_x = 6.1$ MeV in $^{16}$O. Likewise, the $1/2^+$ state at $E_x = 5.29$ MeV can be considered as a $1p_{1/2}$ hole coupled to the $1^-$ vibration at $E_x = 7.1$ MeV in $^{16}$O. Based on these weak coupling model considerations we derived the coupling strengths for the $^{15}$N positive parity states from available inelastic $^{16}$O(p,p') scattering data[38] to the $3^-$ and $1^-$ states of $^{16}$O. The strength derived for the coupling between the ground state and the $2s_{1/2}$ state at $E_x = 5.29$ MeV was $\beta_1 = 0.0208$, and the strength for the coupling to the $1d_{5/2}$ state was $\beta_3 = 0.275$.

The contribution to the $1p_{3/2}$ momentum distribution due to the direct and indirect reaction processes is shown in Figure 22, along with the coupled channels result. The coupled channels result is barely distinguishable from the direct term, the only difference being a slight relative asymmetry. The pure indirect contribution to the $1p_{3/2}$ cross section is seen to be more than three orders of magnitude weaker than the direct contribution at the maximum of the $1p$ momentum distribution.

The analysis of the $^{15}$N discrete states, including coupled channels effects, is distinct from that of the uncoupled states in the following manner: The *rms* radius of the bound state wave functions and the spectroscopic factors $S_\alpha$ for all coupled states are adjusted *simultaneously* to obtain the best fit of the experimental momentum distributions. The effects of the CCIA analysis on the *rms* radii and spectroscopic factors for each state are listed in Table 9. The effect of the channel coupling on the *rms* radius of each state was found to be minimal (2.7%

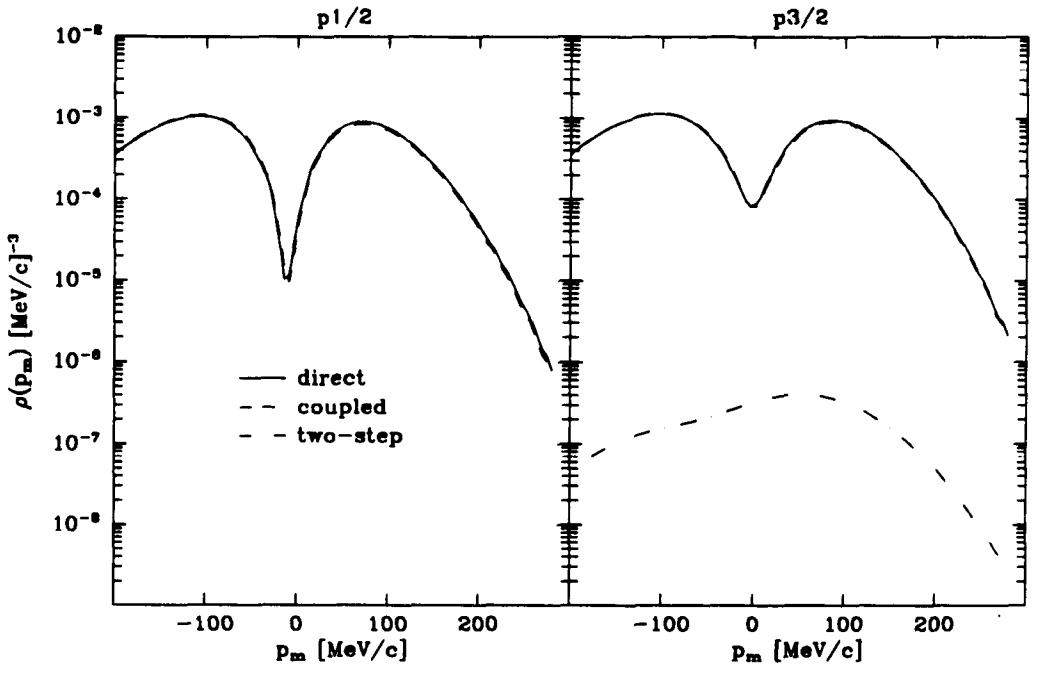


**Figure 22** Results of the CCIA calculation for the $1p_{1/2}$ ground state (left) and $1p_{3/2}$ state (right) at $E_x = 6.3$ MeV.

for the $1p_{1/2}$ ground state and 0.5% for the $1p_{3/2}$ state), while the modification to the spectroscopic factors was more significant. For each $1p$ orbital the spectroscopic factor was reduced - 7.4% for the $1p_{1/2}$ orbital and 4.8% for the $1p_{3/2}$ orbital - relative to the DWIA results. For the $1p_{1/2}$ orbital a spectroscopic factor of 1.17 is found, while the spectroscopic factor of the $1p_{3/2}$ orbital including coupled channels effects is 2.24. We note that the corrected $1p_{3/2}$ spectroscopic factor (for the Kel96n potential) is closer to the earlier value obtained by Bernheim,[10] although their analysis did not include a consideration of coupled channels effects. Although the coupled channels analysis does not alter our impression of these states as arising mainly from direct single-step processes, we conclude that the presence of channel coupling is not negligible and must therefore be considered in order to extract reliable spectroscopic results for the (e,e'p) reaction.

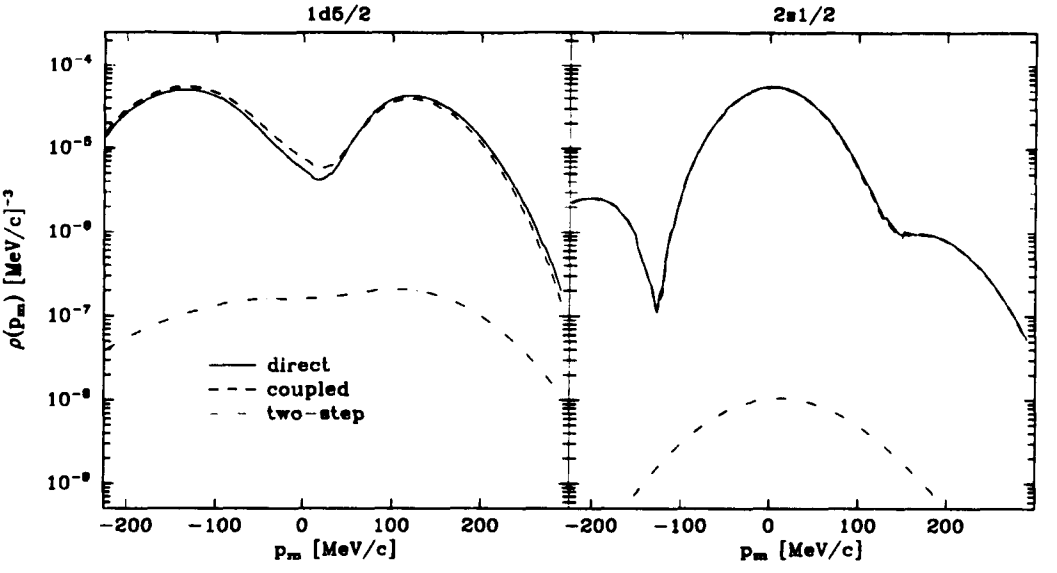


**Figure 23** Results of the CCIA calculation for the $1d_{5/2}$ state at $E_r = 5.27$ MeV (left) and the $2s_{1/2}$ state at $E_r = 5.30$ MeV (right).

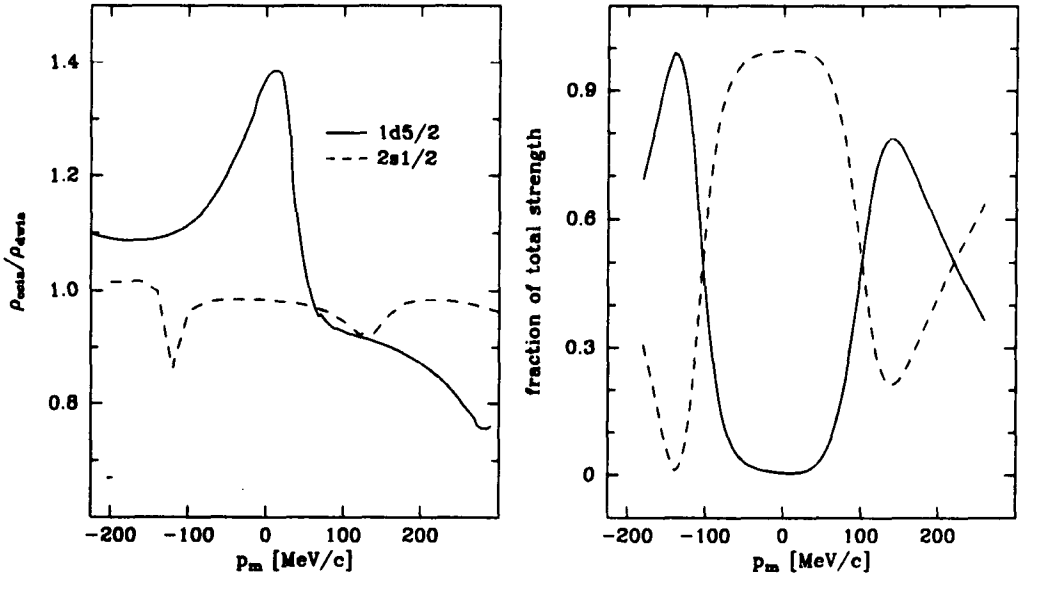


**Figure 24** Ratio of coupled channels calculation to direct knockout calculation for the $2s_{1/2}$ and $1d_{5/2}$ transition in $^{15}$N (left). On the right the fractional contribution to the total momentum distribution from each transition is shown.

| $E_x$ MeV | state $J^\pi$ | radius % | $S_\alpha$ % | $S_\alpha$ |
|---|---|---|---|---|
| 0.00 | $1/2^-$ | 2.7 | -7.4 | 1.167 |
| 5.27 | $5/2^+$ | -2.1 | 14.5 | 0.130 |
| 5.30 | $1/2^+$ | 0.8 | 0.1 | 0.036 |
| 6.32 | $3/2^-$ | 0.5 | -4.8 | 2.235 |

**Table 9** Modifications of the spectroscopic results for the ground state and first three excited states of $^{15}$N due to coupled channels effects in the $^{16}$O(e,e'p)$^{15}$N reaction. The last column lists the final spectroscopic results, including coupled channels effects, extracted with the Kel96n optical potential.

The results of the CCIA calculation for the $2s_{1/2}$ and $1d_{5/2}$ transitions are shown in Figure 23. Due to the weak coupling strength between the $1p_{1/2}$ and the $2s_{1/2}$ state the coupled channels calculation is barely distinguishable from the direct knockout calculation. The pure two-step process is also seen to be extremely weak, amounting to only about 1 part in $10^4$ of the direct knockout term. The indirect contribution to the $1d_{5/2}$ momentum distribution is much stronger than that for the $2s_{1/2}$ momentum distribution, but it still only amounts to about 1% of the overall cross section. As was the case for the $1p$ states, the limited effect due to coupled channels processes allows us to retain our interpretation of the strength in the $(2s_{1/2},1d_{5/2})$ doublet as arising from direct knockout processes. Furthermore, the lack of a strong indirect knockout contribution to the cross section for these positive parity states confirms our interpretation of their strength as arising from proton occupancy of the $2s1d$ shell in $^{16}$O.

Since the $^{16}$O $1^-$ state at $E_x = 7.1$ MeV is only weakly excited, relative to the $3^-$ state at $E_x = 6.1$ MeV, in 100 MeV proton scattering, one would expect that the corresponding effect of the $1p_{1/2} \leftrightarrow 2s_{1/2}$ coupling in $^{15}$N to be weak. This observation is born out in the present analysis, where the coupled channels calculation yields a negligible change to the *rms* radius and spectroscopic strength of the $2s_{1/2}$ state. The coupled channels analysis indicates a much larger effect

– almost 15% in the spectroscopic factor – for the $1d_{5/2}$ state. The effect of the coupled channels calculation on the *rms* radius and spectroscopic factors for the two positive parity states is listed in Table 9.

In addition to the weakness of the coupling strengths between the elastic and positive parity states of $^{15}$N, the coupled channels effects are largely obscured by the incoherent contribution of stronger direct knockout processes. Figure 24 shows the ratio of coupled to direct knockout strengths for the two positive parity states at $E_x$ = 5.3 MeV in $^{15}$N. The channel coupling produces its maximal effect at $p_m$ = 0 MeV for the $1d_{5/2}$ state, which is precisely where the $2s_{1/2}$ direct knockout strength dominates the momentum distribution. Likewise, the channel coupling for the $2s_{1/2}$ state produces its maximal effect at missing momenta of ±120 MeV/c, which are the regions where the $1d_{5/2}$ direct knockout strength is at a maximum. As a result of this fortuitous occurrence, coupled channels effects are obscured for the most part, thus allowing for the reliable extraction of spectroscopic results for these two states from the more straightforward one-step DWIA analysis.

The weak coupling model is often employed in the description of nucleon knockout[7] and stripping[39] reactions, although ideally the coupling strengths should be determined by the inelastic scattering data from the daughter nucleus. In the absence of inelastic proton scattering data for the positive parity states of $^{15}$N, we have derived the coupling strengths for the $(2s_{1/2}.1d_{5/2})$ states of $^{15}$N from the available inelastic (p,p′) scattering data leading to the $1^-$ and $3^-$ states of $^{16}$O. Although this is a commonly accepted procedure, it is still of interest to determine the sensitivity of the extracted (e,e′p) spectroscopic results to the coupling strengths. If the dependence is weak then the source of the coupling strength is irrelevant from a practical point of view, but if the dependence is strong then the weak coupling approach must be carefully scrutinized.

In order to determine the sensitivity of the $(2s_{1/2}.1d_{5/2})$ spectroscopic results on the coupling strengths $\beta$ we have repeated the coupled channels analysis several times using different coupling strengths. The results of this investigation are

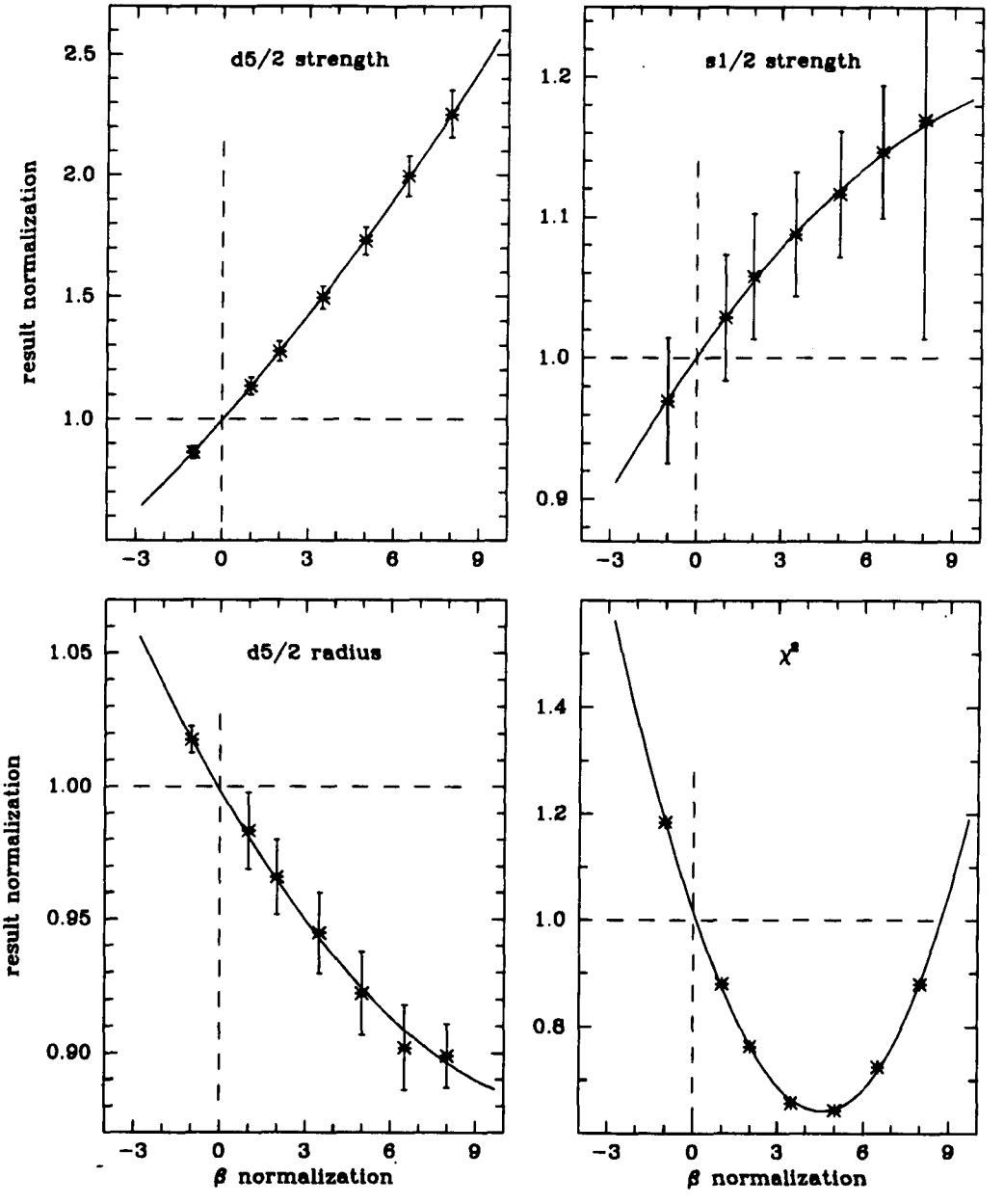


**Figure 25** Dependence of the $(2s_{1/2},1d_{5/2})$ spectroscopic results on the channel coupling strengths $\beta$. The horizontal axis units are defined relative to the nominal $\beta$ values listed in the text, and the vertical axis units are defined relative to the DWIA results with no channel couplings ($\beta = 0$).

shown in figure 25. The coupling strengths $\beta_1$ and $\beta_3$ were both scaled by a single common factor for each analysis. The solid line in each frame is a $2^{nd}$ order polynomial interpolation of the analysis results, and the dashed lines intersect at the results of the DWIA analysis with no channel couplings ($\beta = 0$). It can be seen that the spectroscopic results are all smoothly varying functions of the coupling strengths, and that the behavior of each curve in the vicinity of the nominal $\beta$ value is nearly linear. A doubling of the $\beta$ values derived from the weak coupling model results in an increase of 11% for the $1d_{5/2}$ spectroscopic factor, and 3% for the $2s_{1/2}$ spectroscopic factor. Although these differences are not negligible compared to the precision of the present (e,e'p) results, they are rather modest considering the drastic change in the $\beta$ parameters required to produce them. From the results of this investigation we conclude that the low level of sensitivity displayed by the extracted spectroscopic factors does not warrant concern over the validity of the weak coupling model.

## 4.5 The Search for $7/2^+$ Strength

In the weak coupling model the $3^-$ state in $^{16}O$ can couple to a $1p_{1/2}$ hole to form either a $5/2^+$ or a $7/2^+$ state. The CCIA results pertaining to the $5/2^+$ have already been discussed, but no discrete $7/2^+$ state was observed in the present $^{16}O(e,e'p)^{15}N$ spectral function, although such states have been observed in pickup reactions[40,37] which measure the spectroscopic factors of single particle orbitals in $^{16}O$. In a (d,$^3$He) study of the $^{16}O$ spectral function by Firestone *et al.*,[37] a $7/2^+$ state was observed at $E_x = 7.57$ MeV. Since the (d,$^3$He) interaction is predominately sensitive to the nuclear surface, it is no surprise that a state with high angular momentum such as the $7/2^+$ ($l = 4$) state would appear strongly in the (d,$^3$He) reaction, relative to the (e,e'p) spectrum. The spectroscopic factor deduced from their analysis, assuming a direct knockout from the $1g_{7/2}$ orbital, was 0.45. Noting that an occupation this large was not realistic, they attributed the strength to a strong two-step process. In order to have full confidence in the CCIA analysis of the (e,e'p) results, it is necessary to reconcile the observance of

$5/2^+$ strength and the nonobservance of $7/2^+$ strength in the spectral function of $^{16}$O.

The momentum distribution for the $7/2^+$ state $E_x$ = 7.57 MeV, shown in Figure 26, was obtained by integrating the $^{16}$O spectral function over the missing energy region $19 < E_m < 20$ MeV. This missing energy region contains only three states: a $5/2^+$ at $E_m$ = 19.29 MeV, a $3/2^+$ at $E_m$ = 19.43 MeV, and the $7/2^+$ state at $E_m$ = 19.70 MeV ($E_x$ = 7.57 MeV). The momentum distribution is predominantly $l = 2$ in nature, and a DWIA analysis employing an incoherent sum of $1d_{5/2}$ and $1g_{7/2}$ momentum distributions yielded an upper limit for the $1g_{7/2}$ spectroscopic factor of $S_{g7/2} < 0.0048$.

We have calculated the momentum distribution for the two-step process leading to the $7/2^+$ state in $^{15}$N according to the coupling scheme presented in Figure 21. The best fit of the experimental momentum distribution can be obtained with an incoherent sum of the $1d_{5/2}$ momentum distribution ($S_{d5/2}$ = $0.0431 \pm 0.0029$) and the two-step $1g_{7/2}$ momentum distribution normalized by a factor of $1.083 \pm 0.058$. The magnitude of the (e,e'p) two-step process is sufficient to explain the spectroscopic strength of the transition leading to the $7/2^+$ state at $E_x$ = 7.57 MeV.

## 4.6 Multipole Decomposition of the Continuum

Although no discrete transitions are apparent above $E_m$ = 25 MeV ($E_x$ = 13 MeV) there still exists a sizable amount of strength in the $^{16}$O spectral function. This is due to proton knockout from $^{16}$O leading to highly excited, but unresolved, final states in $^{15}$N. Although this strength cannot be resolved into individual peaks according to missing energy, it can be separated according to its missing momentum dependence in a manner analogous to the analysis of the $(2s_{1/2},1d_{5/2})$ doublet at $E_x$ = 5.3 MeV.

We have performed a multipole decomposition of the $^{16}$O(e,e'p)$^{15}$N spectroscopic strength by dividing the experimental spectral function into missing energy bins of 1 MeV width. Three DWIA momentum distributions were calculated for

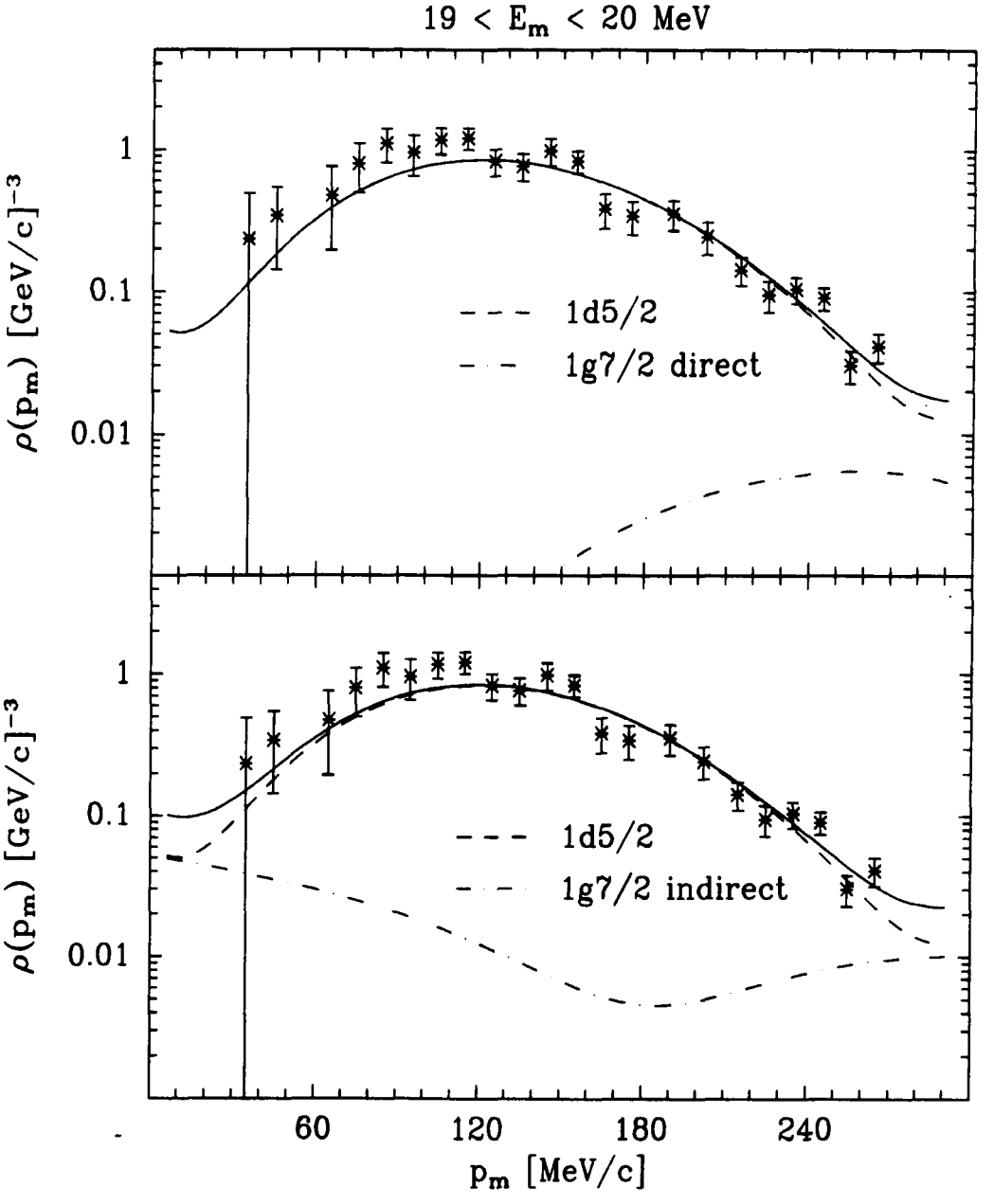


**Figure 26** The momentum distribution for the region $19 < E_m < 20$ MeV. The curves in the top figure represent a DWIA fit assuming direct knockout from the $1g_{7/2}$ orbital of $^{16}O$. In the bottom figure the results of a DWIA+CCIA fit assuming a two-step knockout are shown.

every missing energy interval, one for each angular momentum transfer between $l = 0$ and $l = 2$. The data were not sensitive enough to distinguish between the spin-orbit partners ($j = l \pm 1/2$) for any of the angular momentum multipoles. For the $l = 0$ transfer we used a pure $1s_{1/2}$ overlap for missing energy bins above $E_m = 20$ MeV, and a pure $2s_{1/2}$ overlap for bins below $E_m = 20$ MeV. This approach was motivated from the results of the discrete state analysis, which indicated that all of the $1/2^+$ strength above $E_m = 17.43$ MeV is predominantly $1s_{1/2}$ in nature. We were unable to consider coherent interference between $1s_{1/2}$ and $2s_{1/2}$ amplitudes for any of the $E_m > 20$ MeV bins because contributions from $l = 1$ and $l = 2$ multipoles obscured the high missing momentum shape of the $l = 0$ momentum distributions. The *rms* radii of the bound state wave functions were held constant at the values obtained from the discrete state analysis: $r_{rms} = 1.80$ fm. for the $l = 0$ bound state, 2.74 fm. for $l = 1$, and 3.50 fm. for $l = 2$. The calculation of each bound state wave function was further constrained by selecting the depth of the Woods-Saxon well to reproduce the experimentally observed separation energy for the bin. Each continuum momentum distribution was fit with an incoherent sum of the three DWIA momentum distributions

$$\rho(p_m) = \sum_{l=0}^{2} a_l^2 \rho_l(p_m) \tag{4.1}$$

Where the amplitude $a_l$ is the square root of the spectroscopic factor. The amplitudes $a_l$, rather than the spectroscopic factors, were fit in order to insure that the final fitted spectroscopic factors were all positive.

The results of the multipole decomposition are shown in Figure 27, and the numerical results are tabulated in appendix C. The histograms indicate the results of the multipole decomposition for each of the three multipoles, and the data points indicate the spectroscopic factors obtained from the discrete state analysis. The spectroscopic factors from the multipole decomposition are in excellent agreement with those obtained from the discrete state analysis for intervals that contain discrete states. This observation confirms the general validity of the analysis technique.

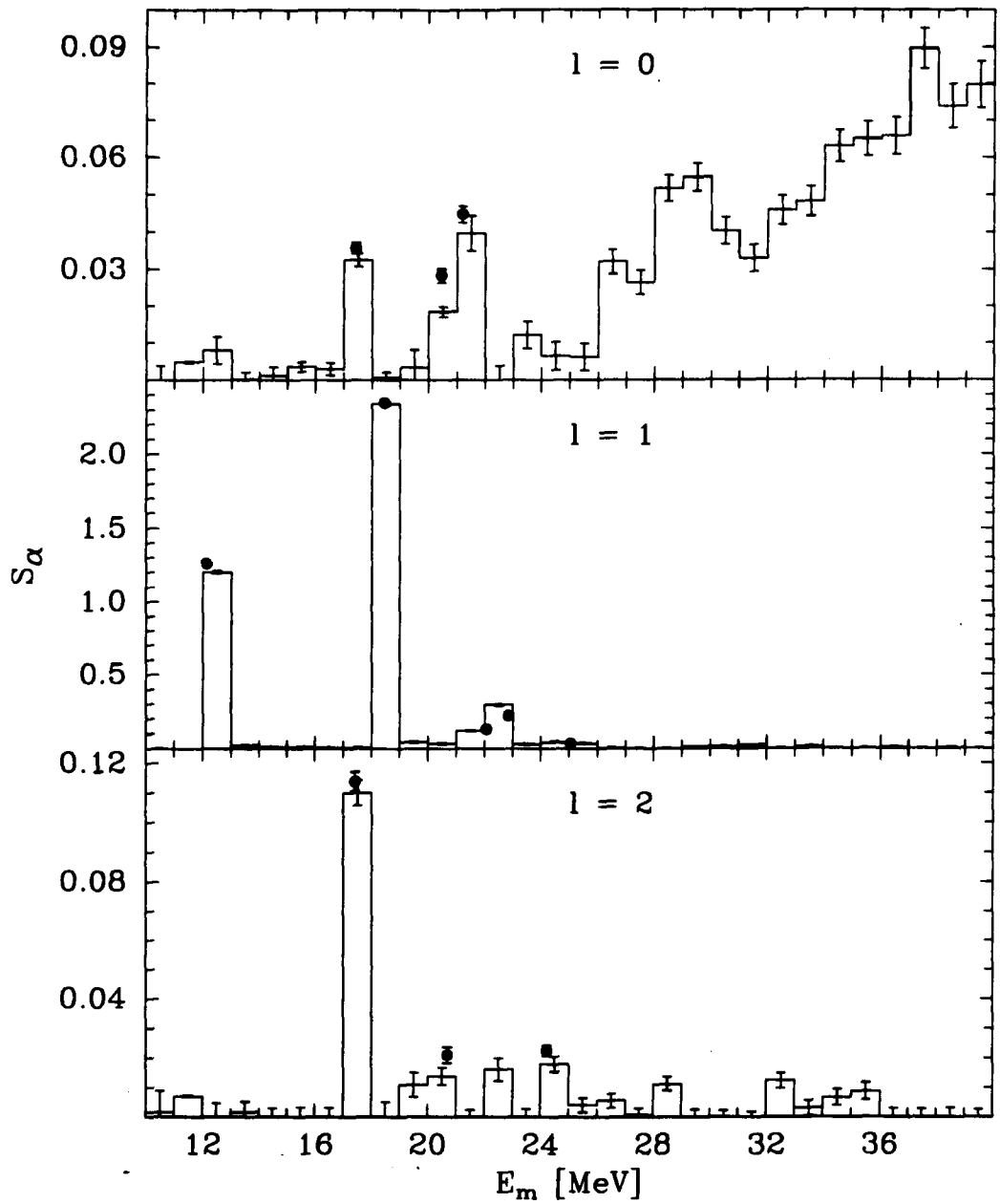


**Figure 27** Multipole decomposition of the $^{16}O(e,e'p)^{15}N$ spectral function. The darkened circles represent the values of the spectroscopic factors extracted from the discrete state analysis.

Most of the $1p$ strength, totaling about 60% of the IPSM sum rule limit, is concentrated in the two states at $E_m = 12.1$ MeV (the $1p_{1/2}$ ground state) and $E_m = 18.4$ MeV ($1p_{3/2}$), while an additional 12% resides in $1p_{3/2}$ fragments at missing energies greater than 19 MeV. The $1p$ strength integrated out to $E_m = 40$ MeV accounts for only 72% ($4.296 \pm 0.024$ protons) of the IPSM limit.

The $l = 0$ spectrum confirms the presence of at least three discrete transitions, each of which was identified and discussed earlier. In addition to these three discrete transitions below $E_m = 22$ MeV, there is also a broad continuum of $l = 0$ strength with a threshold at about $E_m = 25$ MeV, which extends to the limit of the experimental missing energy acceptance at $E_m = 40$ MeV. The summed $l = 0$ spectroscopic strength measured in the present experiment is $0.909 \pm 0.020$. The majority of this strength is consistent with knockout from the $1s_{1/2}$ orbital, as evidenced by the small *rms* radii of the bound state wave functions extracted from the analysis of the discrete states above $E_x = 8$ MeV. Evidence of proton knockout from the $2s_{1/2}$ orbital is found only in the $E_x = 5.30$ MeV state, for which a spectroscopic factor of $S_{2s1/2} = 0.0357 \pm 0.015$ was extracted.

In a recent study of the $^{16}O(e,e'p)^{15}N$ reaction at Saclay,[41,42] where the missing energy spectrum was measured out to 100 MeV, the data exhibit a broad peak in the region 25 MeV $< E_m <$ 65 MeV which is roughly symmetric about its central value of $E_m = 45$ MeV. Since $E_m = 40$ MeV falls just below the maximum of the peak in the Saclay missing energy spectrum, the data suggest that slightly less than one half of the $1s_{1/2}$ strength resides at $E_m < 40$ MeV. On the basis of this comparison it appears that the summed spectroscopic factor of the $1s_{1/2}$ orbital, extrapolated from the results of the present experiment, is close to the IPSM limit of 2.

It is interesting to note that the onset of the broad $l = 0$ response at $E_m = 25$ MeV corresponds roughly to the threshold for two nucleon knockout at $E_m = 22.2$ MeV. It is not well understood how the presence of this additional reaction channel affects the interpretation of the spectroscopic results as occupation probabilities.

Approximately one half of the $l = 2$ strength found in the present $^{16}O$ spectral

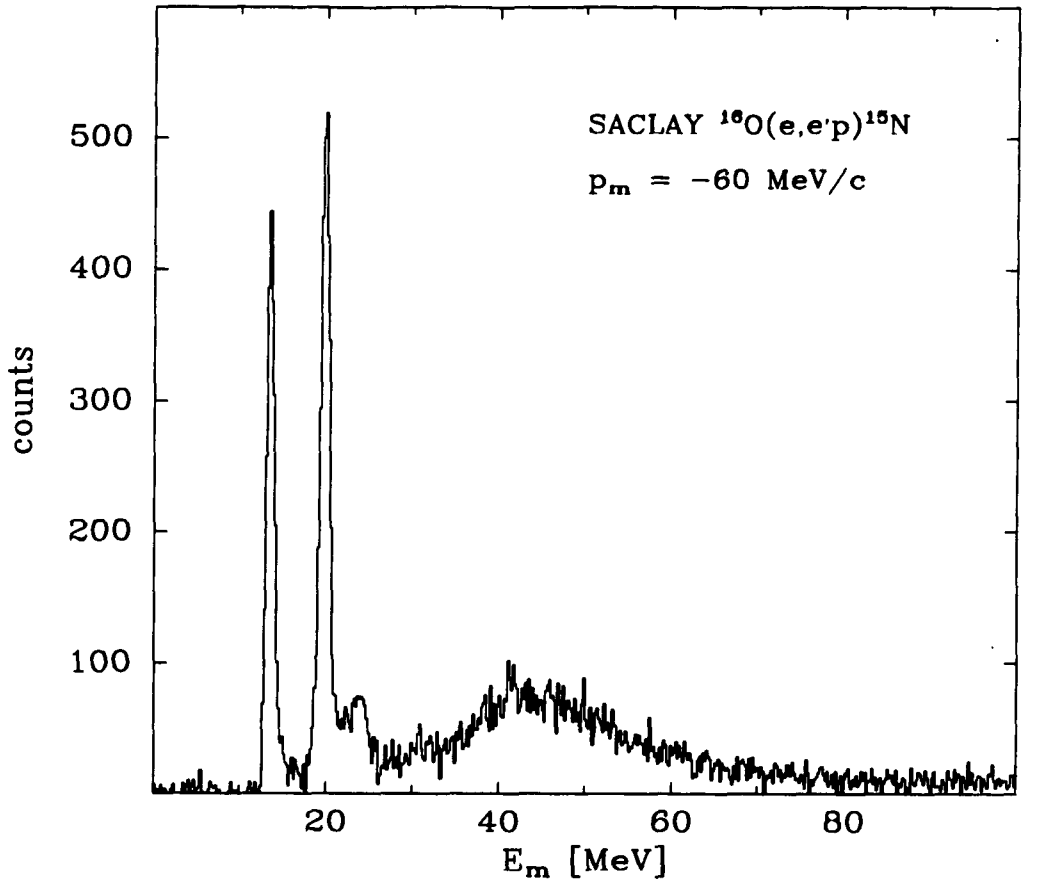


**Figure 28** Missing energy spectrum from the $^{16}$O(e,e'p)$^{15}$N measurement at Saclay. The missing momentum is held constant at -60 MeV/c.

function resides in the $5/2^+$ state at $E_m$ = 17.40 MeV, while the rest resides in fragments extending out to a missing energy of 37 MeV. Although the analysis of the $20 < E_m < 21$ MeV momentum distribution, discussed in the previous section, confirms the presence of at least one $3/2^+$ state in the $^{16}$O spectral function, we are otherwise unable to distinguish between knockout from the $1d_{3/2}$ orbital and the $1d_{5/2}$ orbital. For the multipole analysis we have assumed that all $l = 2$ strength arises from $1d_{5/2}$ proton knockout. The summed spectroscopic strength of the $1d_{5/2}$ orbital, measured out to $E_m$ = 40 MeV, is found to be $S_{d5/2} = 0.233 \pm 0.017$.

There was no evidence found in the present $^{16}$O spectral function for the occupation of the $1f_{7/2}$ ($l = 3$) or $1g_{7/2}$ ($l = 4$) orbitals. A multipole analysis of the continuum with these two multipoles included confirmed this result, as there was no statistically significant improvement in the quality of the fit (in terms of $\chi^2$) with these multipole included, and the strengths of the three lower multipolarities were not affected.

Since the spectroscopic strengths are statistically correlated in such an analysis, it is likely that strength is "borrowed" between adjacent multipolarities, particularly in missing energy intervals where there is no dominant multipole contributing to the observed strength. This unfortunate circumstance imposes a limit to the validity of the multipole decomposition technique. The tendency for the spectroscopic factors obtained from the multipole decomposition to be a few percent lower than those obtained from the discrete state analysis provides a measure of this limitation.

The effect of the spreading of multipole strength between adjacent multipoles can be quite important in missing energy regions containing only weak transitions. This is particularly evident in the missing energy region $20 < E_m < 21$ MeV. The analysis of this region was discussed in section 4.3, where it was determined that the momentum distribution is well described by an incoherent sum of $1s_{1/2}$ and $1d_{3/2}$ momentum distributions. For the present multipole decomposition analysis, however, in which a $l = 1$ ($1p_{3/2}$) contribution is also included, it is seen that the extracted spectroscopic factor for the $l = 1$ component, $S_{1p3/2} = 0.033 \pm 0.004$, is larger than either the $1s_{1/2}$ ($S_{1s1/2} = 0.018 \pm 0.002$) or $1d_{3/2}$ ($S_{1d3/2} = 0.014 \pm 0.003$) spectroscopic factors. The reduction of the spectroscopic factors extracted from the multipole decomposition, relative to those extracted from the analysis of section 4.4, is 33% for the $l = 0$ transition and 34% for the $l = 2$ transition.

On the basis of the multipole decomposition we have determined that the total spectroscopic strength for $^{16}$O summed up to a missing energy of $E_m = 40$ MeV is $5.42 \pm 0.04$. An extrapolation of this sum out to a missing energy of

$E_m$ = 65 MeV on the basis of a comparison of our missing energy spectrum to that of the Saclay measurement yields a total spectroscopic strength of only 80% of the IPSM limit for $^{16}$O. This suggests that the remaining 20% of the proton spectroscopic strength resides at separation energies beyond 65 MeV. The lack of observed strength gives us an indirect measure of the number of protons in $^{16}$O engaged in nucleon-nucleon correlations.

## 4.7 Comparison with Other Experiments

Several studies have been performed on the $^{16}$O nucleus with the objective of measuring the spectroscopic strengths of transitions leading to the discrete final of $^{15}$N. Prior to the $^{16}$O(e,e'p)$^{15}$N experiment of Bernheim *et al.*,[10] published in 1982, all of these studies involved hadronic pickup reactions. A representative sample of results from these experiments is presented in Table 10, along with the results from the (e,e'p) experiments. Neutron pickup reactions have also been included for comparison, since the low-lying states of the $^{15}$N spectrum are all present in the mirror $^{15}$O nucleus as well.

The differences among the extracted spectroscopic factors between the various hadron-induced reactions are seen to be very large for each of the four $^{15}$N levels tabulated. For the (d,$^3$He) reaction the spectroscopic factors for the $1p$ states exceed the IPSM limit in some cases. In view of these unphysical results, it is not possible to associate realistic occupation numbers with the spectroscopic factors deduced from hadronic interactions. The large differences between the results deduced from the various nucleon stripping and pickup reactions is a reflection on the model dependence of the description of the nucleon-nucleon interaction employed in the analysis.

The results of a complementary study of the (e,e'p) and (d,$^3$He) reactions by Kramer[7] indicate that the model dependence of the (d,$^3$He) reaction can be reduced, and that the spectroscopic results of the (d,$^3$He) and (e,e'p) reaction can be brought into agreement with one another. Spectroscopic factors from the (e,e'p) and (d,$^3$He) reaction were compared for the valence orbitals of nuclei

| reaction | $1/2^-$ 0.00 MeV | $5/2^+$ 5.27 MeV | $1/2^+$ 5.30 MeV | $3/2^-$ 6.32 MeV | ref. |
|---|---|---|---|---|---|
| (p,d) | 1.80 | 0.11 | 0.02 | 2.60 | Snelgrove[40] |
| (d,$^3$He) | 2.60 | 0.26 | 0.06 | 5.60 | Firestone[37] |
| (d,$^3$He) | 2.30 | 0.31 | 0.038 | 3.64 | Hiebert[43] |
| (d,$^3$He) | 2.18 | 0.16 | 0.10 | 3.32 | Hartwig[44] |
| (d,t) | 1.50 | 0.043 | 0.027 | 3.10 | Purser[45] |
| ($^3$He,$\alpha$) | 1.00 | 0.58 | 0.22 | 2.11 | Bohne[46] |
| (e,e'p) | 1.18 | — | — | 2.24 | Bernheim[10] |
| (e,e'p) | 1.26(1) | 0.114(3) | 0.036(2) | 2.38(2) | present results |

**Table 10** Spectroscopic factors for the first four levels in $^{15}$N from various knockout and pickup reactions.

ranging from $^{16}$O (using the results of the present analysis) to $^{208}$Pb. On an average, the spectroscopic factors extracted from the (d,$^3$He) analyses were found to be a factor of 2 greater that the corresponding (e,e'p) results. The (d,$^3$He) data were then reanalyzed using the BSWF parameters deduced from the (e,e'p) DWIA analysis of the same nucleus. The resulting spectroscopic factors were reported to deviate from the (e,e'p) spectroscopic factor by an average of only 1%, with a spread of 25%.

## 4.8 Discussion of Results

In this chapter we have presented the results of our analysis of the $^{16}$O spectral function. Of particular interest is the depletion of the summed spectroscopic strength for orbitals below the fermi level, relative to the IPSM limit, and the nonzero spectroscopic strength for orbitals above the fermi level. The spectroscopic strength of the orbitals above the fermi level is found to be insufficient to

account for the depletion of the orbitals below the fermi level. In order to draw physically significant conclusions from these results, however, the validity of the underlying assumptions of the analysis must be considered.

The quasielastic (e,e'p) reaction was utilized due to its relative model independence, as compared to hadron-induced reactions. Three implicit assumptions are made in deriving the final expression for the (e,e'p) cross section: the Born approximation, the quasielastic assumption, and the impulse approximation. The Born (single photon exchange) approximation is easily justified due to the weakness of the electromagnetic interaction. The probability for multiple photon exchanges is well known from quantum electrodynamics to decrease by a factor of the fine structure constant for each additional photon exchange. Evidence which supports the quasielastic assumption is observed in the systematics of inclusive electron scattering spectra for all nuclei,[12] in which a peak centered about elastic electron-proton scattering kinematics is observed.

The impulse approximation, in which the coupling of a bound nucleon to the virtual photon is assumed to be the same as the coupling of free nucleon, is the subject of considerable debate. Longitudinal-Transverse separations of the inclusive (e,e') quasielastic cross section[47,48] indicate deviations from the impulse approximation picture. In particular, the Coulomb sum rule is depleted by approximately 40%, and the ratio of the longitudinal/transverse response functions is smaller than expected. Several models have been proposed to explain these discrepancies, involving for instance medium modifications of nucleon properties such as swelling[49] and six-quark bags,[50] although none have been successful.

The apparent breakdown of the impulse approximation indicates the presence of a reaction mechanism other than one-body knockout in the quasielastic region. Experimental evidence for additional reaction channels has been obtained from two recent experiments at the Bates-MIT linear accelerator. Ulmer *et al.*[51] performed a separation of the longitudinal and transverse response functions for the quasielastic $^{12}$C(e,e'p) reaction. Both response functions exhibit peaks representing knockout from the $1p$ and $1s$ shells. The longitudinal response function

vanishes at a missing energy $E_m$ = 48 MeV, while the transverse response function exhibits a significant strength all the way out to the experimental limit of $E_m$ = 65 MeV. The additional transverse strength is remains unexplained in terms of single-particle knockout mechanisms.

A measurement of the $^{12}$C(e,e'p) reaction[52] in the intermediate region between the quasielastic and delta peaks, known as the "dip" region, provides additional evidence for the breakdown of the impulse approximation. The missing energy spectrum contains the familiar features of $1p$ and $1s$ knockout, and beyond the $1s$ peak there exists a level continuum of knockout strength extending to the experimental limit of $E_m$ = 150 MeV. The existence of the coincidence knockout strength in a kinematical region beyond the quasielastic peak suggests the presence of multinucleon knockout mechanisms. In addition, the high missing energy continuum cannot be explained by single nucleon knockout mechanisms. A calculation by Takaki[53] shows that at least three-nucleon knockout mechanisms are required to populate the missing energy regions beyond $E_m$ = 60 MeV.

There exists much experimental evidence which suggests the breakdown of the impulse approximation. The exact nature of the breakdown has not been specified experimentally, nor have the currently measured deviations from the impulse approximation predictions been explained theoretically. A breakdown of the impulse approximation will affect the electron-proton cross section $\sigma_{ep}$, and therefore change the normalization of the experimental spectral functions extracted from (e,e'p) measurements. It is therefore of considerable interest to determine the exact nature of the breakdown so that it can be incorporated into the model description of coincidence reactions. In 1989 the first measurement of the triple coincidence (e,e'pp) reaction was performed at NIKHEF by a collaboration which included the UNH nuclear physics group. This measurement was the first of a developing program, to be continued in the near future at CEBAF and Bates-MIT (with the CLAS and BLAST detectors, respectively), aimed at defining the reaction mechanism more exclusively so that progress can be made in this important area.

# 5. Conclusions

We have measured the quasielastic $^{16}O(e,e'p)$ reaction in order to determine the distribution of spectroscopic strength in $^{16}O$. The $^{16}O$ spectral function was measured in parallel kinematics over an extended region of missing energy and missing momentum. The total kinetic energy in the center of mass of the final hadronic system was kept constant, thereby insuring that effects due to proton distortions remained the same for all kinematics. The utilization of this kinematical arrangement allowed us to extract an experimental spectral function free from contributions due to unknown variations of the final state interaction across the $(E_m,p_m)$ spectrum.

The distortions of the outgoing proton wave functions were calculated in five different optical potentials. The optical potentials were derived from three sources; two were derived from fits to elastic $^{16}O(p,p')$ scattering data at an incident energy of 100 MeV in the lab, two were derived from fits to inelastic $^{16}O(p,p')$ data at the same energy using the LDA calculations of Kelly, and the fifth optical potential was calculated from the global energy dependent parameterization due to Schwandt.

The DWIA analysis of the $1p$ states utilizing the five optical potentials yielded spectroscopic results which were in excellent agreement with one another for the ground state $1p_{1/2}$ transition at $E_m$ = 12.1 MeV. The spectroscopic factor of this state was determined to be $1.17 \pm 0.07$ (including statistical and systematic uncertainty), corresponding to 63% of the IPSM limit. The same consistency was not observed among the spectroscopic results for proton knockout leading to the $3/2^-$ state at $E_m$ = 18.4 MeV. For this transition the spectroscopic factors differed by almost 20% between the extreme values. The lowest values for the $1p_{3/2}$ spectroscopic factor were obtained from the DWIA analysis using optical potentials derived from elastic (p,p') scattering data, while the highest values were obtained with optical potentials derived from inelastic (p,p') scattering data. Since all five optical potentials give excellent descriptions of the shape of both $1p$ momentum distributions, including the negative missing momentum regions, we

have ruled out the possibility that the differences arise from an anomalous effect not contained within the description of the DWIA. Rather, we are convinced that the effect arises from an ambiguity in the description of the final state interaction itself.

Special emphasis was placed on the determination of spectroscopic factors for the low-lying positive parity states of $^{15}$N. In particular, knockout strength leading to the positive parity ($1/2^+, 5/2^+$) doublet at $E_x$ = 5.3 MeV reflects the presence of multinucleon correlations leading to the partial occupancy of the $2s1d$ shell in $^{16}$O. The results of the DWIA analysis, including coupled channels effects, indicate a spectroscopic factor of $0.0357 \pm 0.0020$ for the $2s_{1/2}$ orbital, and $0.1305 \pm 0.0072$ for the $1d_{5/2}$ orbital. The absolute uncertainty in the spectroscopic factor of these orbitals, amounting to only 7 parts in 1000, provides an impressive indication of the accuracy of the (e,e'p) reaction as a spectroscopic tool.

A measurement of the spectroscopic factor leading to the $3/2^+$ state at $E_x$ = 8.57 MeV was possible despite the fact that the state was not resolved in missing energy. An angular momentum decomposition of the missing energy region surrounding this well isolated state yielded a spectroscopic strength of $S_{d3/2}$ = 0.0210(28). An upper limit of $S_{g7/2} < 0.0048$ was established for the spectroscopic factor of the $7/2^+$ state at $E_x$ = 7.57 MeV. A calculation of the two-step process leading to this state was consistent with the magnitude of this strength however, so we are unable to interpret it as arising from an occupation of the $1g_{7/2}$ orbital in $^{16}$O.

Coupled channels calculations were performed for the $^{16}$O(e,e'p)$^{15}$N reaction leading to the ground state of $^{15}$N, as well as for the first three excited states. The inclusion of coupled channels effects did not significantly alter the spectroscopic results relative to the direct knockout results for any of these states. For the $1p$ states, the channel coupling interferes constructively with both states, leading to reductions in the spectroscopic factor of 7.4% for the $1p_{1/2}$ ground state and 4.6% for the $1p_{3/2}$ state at $E_m$ = 18.4 MeV. The coupled channels calculations induce only minimal (< 3%) changes in the *rms* radii of these states. The coupled chan-

nels calculations for the $(1/2^+, 5/2^+)$ doublet at $E_x = 5.3$ MeV were performed using a prescription based on the weak coupling model for the coupling between the ground state and the positive parity states. The results of this analysis indicate a modest (15%) enhancement of the spectroscopic factor of the $1d_{5/2}$ state, while all of the other adjustable spectroscopic parameters incurred only slight (less than 2%) changes.

A multipole decomposition of the missing energy region $10 < E_m < 40$ MeV was performed using angular momentum multipoles $l = 0$ through $l = 2$. The spectroscopic results from the multipole decomposition were found to be in excellent agreement with those from the discrete state analysis. A slight ($< 3.0\%$) systematic reduction of the spectroscopic factors obtained from the multipole decomposition relative to those obtained from the discrete state analysis was observed. This reduction arises from the fact that spectroscopic strengths of the multipoles are all positively correlated with one another, which leads to a slight spurious spreading of strength among the multipoles.

Momentum distributions for a total of 10 discrete states were extracted from the $^{16}$O spectral function. The DWIA analysis of these states yielded spectroscopic factors as small as $S_\alpha = 0.0225$, reflecting the impressive sensitivity of the (e,e'p) reaction as a probe of single nucleon wave functions. For the missing energy region $10 < E_m < 40$ MeV only $68\% \pm 5.5\%$ of the total IPSM strength is observed in the $^{16}$O spectral function. The depletion of strength is most pronounced in the $1p$ shell, where only 72% of the IPSM limit is observed. A comparison of the continuum $1s$ strength observed in the present experiment to that observed in a recent experiment at Saclay indicates a summed spectroscopic strength close to the IPSM-limit of 2 for the $1s_{1/2}$ orbital.

# REFERENCES


1. P. J. Brussaard and P. W. M. Glaudemans, *Shell-Model Applications in Nuclear Spectroscopy*, North-Holland, Amsterdam (1977)
2. H. Tyreń, Th. A. J. Maris and P. Hillman, *Il Nuovo Cimento* **6** (1957) 1507.
3. H. Tyreń, P. Hillman and Th. A. J. Maris, *Il Nuovo Cimento* **7** (1958) 10.
4. Gerard van der Steenhoven, Ph.D. thesis, Vrije Universiteit, 1987, unpublished
5. G. Jacob and Th. A. J. Maris, *Nucl. Phys.* **32** (1962) 139.
6. P. K. A. de Witt Huberts, *J. Phys. G.* **16** (1990) 507.
7. G. J. Kramer, Ph.D. thesis, Universiteit van Amsterdam, 1990, unpublished
8. G. van der Steenhoven, H. P. Blok, E. Jans, L. Lapikás, E. N. M. Quint and P. K. A. de Witt Huberts, *Nucl. Phys.* **A484** (1988) 445.
9. G. J. Kramer *et al.*, *Phys. Lett.* **B227** (1989) 199.
10. M. Bernheim *et al.*, *Nucl. Phys.* **A375** (1982) 381.
11. S. Frullani and J. Mougey, *Adv. Nucl. Phys.* **14** (1984) 1.
12. R. R. Whitney, I. Sick, J. R. Ficenec, R. D. Kephart and W. P. Trower, *Phys. Rev.* **C9** (1974) 2230.
13. T. de Forest Jr., *Nucl. Phys.* **A392** (1983) 232.
14. A. S. Raskin and T. W. Donnelly, *Polarization in Coincidence Electron Scattering from Nuclei*, preprint
15. I. J. R. Aitchison and A. J. G. Hey, *Gauge Theories in Particle Physics*, Adam Hilger, Bristol (1989)
16. S. Boffi, C. Giusti, F. D. Pacati and S. Frullani, *Nucl. Phys.* **A319** (1979) 461.

17. S. Boffi, F. Cannata, F. Capuzzi, C. Giusti and F. D. Pacati, *Nucl. Phys.* **A379** (1982) 509.

18. S. Boffi, C. Giusti and F. D. Pacati, *Nucl. Phys.* **A336** (1980) 437.

19. C. Giusti and F. D. Pacati, *Nucl. Phys.* **A473** (1987) 717.

20. C. Giusti and F. D. Pacati, *Nucl. Phys.* **A485** (1988) 461.

21. G. R. Satchler,*Direct Nuclear Reactions*, Claredon Press, New York (1983)

22. F. G. Perey,*Direct Interactions and Nuclear Reaction Mechanism*, edited by Clementel and Villi, Gordon and Breach, New York (1963)

23. C. de Vries, C. W. de Jager, L. Lapikás, G. Luijckx, R. Maas, H. de Vries and P. K. A. de Witt Huberts, *Nucl. Instr. and Meth.* **223** (1984) 1.

24. C. Bibo, Diplomarbeit, Mainz, 1984, unpublished

25. N. Voegler and J. Friedrich, *Nucl. Instr. and Meth.* **198** (1982) 293.

26. H. de Vries, C. W. de Jager and C. de Vries, *Atom. Data and Nucl. Data Tables* **36** (1987) 495.

27. J. W. den Herder, H. P. Blok, E. Jans, P. H. M. Keizer, L. Lapikás, E. N. M. Quint, G. van der Steenhoven and P. K. A. de Witt Huberts, *Nucl. Phys.* **A490** (1988) 507.

28. G. van der Steenhoven, H. P. Blok, E. Jans, M. de Jong, L. Lapikás, E. N. M. Quint and P.K.A. de Witt Huberts, *Nucl. Phys.* **A480** (1988) 547.

29. E. N. M. Quint, Ph.D. thesis, Universiteit van Amsterdam, 1988, unpublished

30. J. J. Kelly, University of Maryland, College Park, Md., private communication

31. computer code ECIS, *NIKHEF-K*, Amsterdam, The Netherlands

32. P. Schwandt, H. O. Meyer, W. W. Jacobs, A. D. Bacher, S. E. Vigdor, M. D. Kaitchuck and T. R. Donoghue, *Phys. Rev.* **C26** (1982) 55.

33. J. J. Kelly, *Phys. Rev.* **C39** (1989) 2120.

34. edited by C. Michael Lederer and Virginia S. Shirley *Table of Isotopes, 7th ed.*, John Wiley and Sons, New York

35. H. P. Blok and G. van der Steenhoven, *Phys. Rev.* **C35** (1987) 2347.

36. H. Fabrici, S. Micheletti, M. Pignanelli, F. G. Resmini, R. de Leo, G. D'Erasmo and A. Pantaleo, *Phys. Rev.* **C21** (1980) 844.

37. M. A. Firestone, J. Jänecke, A. Dudek-Ellis, P. J. Ellis and T. Engeland, *Nucl. Phys.* **A258** (1976) 317.

38. K. Amos *et al.*, *Nucl Phys* **A413** (1984) 255.

39. S. Lie, T. Engeland and G. Dahll, *Nucl. Phys.* **A156** (1970) 449.

40. J. L. Snelgrove and E. Kasky, *Phys. Rev.* **187** (1969) 1246.

41. L. Chinitz *et al.*, *Phys. Rev. Lett.* **67** (1991) 568.

42. L. Chinitz, University of Virginia, Charlottesville, Va., private communication

43. J. C. Hiebert, E. Newman and R. H. Bassell, *Phys. Rev.* **154** (1967) 898.

44. D. Hartwig, Doctoral Thesis, Karlsruhe, 1971, unpublished

45. K. H. Purser *et al.*, *Nucl. Phys.* **A132** (1969) 75.

46. W. Bohne *et al.*, *Nucl. Phys.* **A113** (1968) 97.

47. Z. E. Meziani *et al.*, *Phys. Rev. Lett.* **52** (1984) 2130.

48. M. Deady *et al.*, *Phys. ReV.* **C33** (1986) 1897.

49. L. B. Weinstein, Ph.D. thesis, MIT, 1988, unpublished

50. P. J. Mulders, *Nucl. Phys.* **A459** (1986) 525.

51. P. E. Ulmer *et al.*, *Phys. Rev. Lett.* **59** (1987) 2259.

52. R. W. Lourie *et al.*, *Phys. Rev. Lett.* **56** (1986) 2364.

53. T. Takaki, *Phys. Rev. Lett.* **62** (1989) 395.

54. William H. Press, Brian P. Flannery, Saul A. Teukolsky and William T. Vetterling, *Numerical Recipes, the Art of Scientific Computing*, Cambridge University Press, 1987

55. F. W. Hersman, University of New Hampshire, Durham, NH., private communication

56. F. W. Hersman, University of New Hampshire, Durham, NH., computer code minim, 1989

# APPENDIX A

## Least Squares Fitting Techniques

In this section we discuss the various methods used to model experimental data in the present (e,e'p) analysis. The notation of Press[54] *et al.* is followed as closely as possible for the discussion of conventional general least-squares fitting. For a more detailed discussion concerning these methods one should consult chapters 10 and 14 of *Numerical Recipes, the Art of Scientific Computing.* In addition to the discussion of conventional least-squares fitting methods, we also discuss a new, fully generalized, multi-parameter nonlinear least-squares fitting procedure developed and implemented at UNH.

Traditional fitting procedures are designed to describe a set of experimental data points with a model which relates the dependent and independent variables of a function, and which depends upon a set of adjustable parameters. One then attempts to adjust these parameters to achieve maximal agreement between the model function and the experimental data, via the minimization of a prescribed figure-of-merit function. Throughout the present analysis we have used $\chi^2$ as a figure-of-merit function:

$$\chi^2 = \sum_{i=1}^{N} \left( \frac{y_i - y(x_i; \mathbf{a})}{\sigma_i} \right)^2 \qquad \mathbf{a} = \{a_1, a_2, \ldots, a_M\} \tag{A1}$$

where $(x_i, y_i)$ $i = 1, \ldots, N$ are the experimentally observed set of data points (independent and dependent variables, respectively), $\sigma_i$ is the uncertainty in the measurement, and $y(x; \mathbf{a})$ is the model function which depends on parameters $\mathbf{a}$.

Depending on the type of model function, and the relation of the adjustable parameters to the model function, the task of minimizing the figure-of-merit function may be quite trivial or very difficult. In the case of the general *linear* least squares fit the model function is generated as a linear combination of a set of

basis functions:

$$y(x;\mathbf{a}) = \sum_{k=1}^{M} a_k X_k(x) \tag{A2}$$

where the adjustable parameters $a_k$ are simply expansion coefficients, and the $X_k(x)$ are the basis functions. In this case the basis functions themselves are not explicitly dependent on the adjustable parameters. To minimize $\chi^2$ for the general linear least-squared system the derivative of $\chi^2$ with respect to each of the adjustable parameters must equal zero. The set of these derivative equations, known as the *normal equations* of the least-squares problem (one for each parameter), are given by:

$$\sum_{i=1}^{N} \frac{1}{\sigma_i^2}\Big[y_i - \sum_{j=1}^{M} a_j X_j(x_i)\Big] X_k(x_i) = 0 \qquad k = 1 \ldots M \tag{A3}$$

In matrix form, this equation can be rewritten as

$$\sum_{j=1}^{M} \alpha_{kj} a_j = \beta_k \tag{A4}$$

$$\alpha_{kj} \equiv \sum_{i=1}^{N} \frac{X_j(x_i) X_k(x_i)}{\sigma_i^2} \qquad \beta_k \equiv \sum_{i=1}^{N} \frac{y_i X_k(x_i)}{\sigma_i^2} \tag{A5}$$

This set of coupled equations can easily be solved using a number of conventional matrix inversion techniques.

When the model function is nonlinearly dependent on the adjustable parameters, an iterative procedure must be used to minimize $\chi^2$. A taylor expansion of $\chi^2$ about a coordinate $\mathbf{a}$ in the parameter space is given by

$$\chi^2(\mathbf{x}) = \chi^2(\mathbf{a}) + \sum_i \left.\frac{\partial \chi^2}{\partial x_i}\right|_{x_i = a_i} (x_i - a_i) + \frac{1}{2}\sum_{i,j} \left.\frac{\partial^2 \chi^2}{\partial x_i \partial x_j}\right|_{\substack{x_i = a_i \\ x_j = a_j}} (x_i - a_i)(x_j - a_j) + \cdots \tag{A6}$$

$$\approx c - \mathbf{b}\cdot\mathbf{x} + \frac{1}{2}\cdot\mathbf{x}\cdot\mathbf{A}\cdot\mathbf{x} \tag{A7}$$

$$c \equiv \chi^2(\mathbf{a}) \qquad \mathbf{b} \equiv -\nabla \chi^2\Big|_{\mathbf{a}} \qquad A_{ij} \equiv \frac{\partial^2 \chi^2}{\partial x_i \partial x_j}\Big|_{\substack{x_i=a_i \\ x_j=a_j}} \tag{A8}$$

The gradient of $\chi^2$ is then given by

$$\nabla \chi^2 = \mathbf{A} \cdot \mathbf{x} - \mathbf{b} \tag{A9}$$

At the $\chi^2$ minimum the gradient will vanish and the relation

$$\mathbf{A} \cdot \mathbf{x}_{min} = \mathbf{b} \tag{A10}$$

will be obeyed. Combining equations ( A 9) and ( A 10) we obtain a prescription for taking a step in the parameter space

$$\delta\mathbf{x} \equiv \mathbf{x}_{min} - \mathbf{x} = \mathbf{A}^{-1} \cdot [-\nabla \chi^2(\mathbf{x})] \tag{A11}$$

Equation ( A 11) provides the exact solution in the limit where equation ( A 7) is exact. As the vector $\mathbf{x}$ gets closer to the minimum of $\chi^2$, located at $\mathbf{x}_{min}$, the higher order contributions to the taylor expansion become increasingly small. In matrix form, equation ( A 11) can be rewritten in a manner analogous to equation ( A 4).

$$\sum_{j=1}^{M} \alpha_{kj} \delta x_j = \beta_k \tag{A12}$$

where the derivatives can be calculated from equation ( A 1).

$$\beta_k \equiv -\frac{1}{2}\frac{\partial \chi^2}{\partial a_k} = -2\sum_{i=1}^{N} \frac{[y_i - y(x_i;\mathbf{a})]}{\sigma_i^2}\frac{\partial y(x_i;\mathbf{a})}{\partial a_k} \qquad k = 1, \ldots, M \tag{A13}$$

$$\alpha_{kj} \equiv \frac{1}{2}\frac{\partial^2 \chi^2}{\partial a_k \partial a_j} = \sum_{i=1}^{N} \frac{1}{\sigma_i^2}\left[\frac{\partial y(x_i;\mathbf{a})}{\partial a_k}\frac{\partial y(x_i;\mathbf{a})}{\partial a_j} - [y_i - y(x_i;\mathbf{a})]\frac{\partial^2 y(x_i;\mathbf{a})}{\partial a_k \partial a_j}\right] \tag{A14}$$

By convention, the second derivative in equation ( A 14) is omitted. If the model function $y(x;\mathbf{a})$ describes the data well, then $y_i - y(x_i;\mathbf{a})$ will be small, and the

statistical fluctuations of the data about the model will likely lead to an overall cancellation of this term. If the model function is a poor representation of the data, or if the initial parameter set is far from the $\chi^2$ minimum, then the right hand term could be quite large, and could then possibly play a destabilizing role in the iterative procedure. The omission of the second term is justified, as Press *et al.* point out, since modifications of $\alpha$ have no effect on the final parameter set $\mathbf{a}$ reached, only on the iterative path taken to reach them. The condition for the $\chi^2$ minimization is that the first derivatives $\beta_k$ vanish, independent of how $\alpha$ is defined. Hence the matrix equation ( A 12) can be solved solely from knowledge of the model function and its first derivatives.

The approach to finding the minimum of the general nonlinear least squares problem is therefore straightforward. One must continue to take steps $\delta\mathbf{x}$ in parameter space until successive iterations fail to meaningfully improve $\chi^2$, at which point convergence is achieved.

The accuracy of the step $\delta\mathbf{x}$ depends on the contribution to $\chi^2$ due to higher order terms in the taylor series. If it turns out that equation ( A 7) is a poor approximation of $\chi^2$, then it is possible that the new selection of parameters $\mathbf{x} + \delta\mathbf{x}$ will not lead to a reduction of $\chi^2$. In this case the minimization strategy most likely to succeed is to simply follow the gradient of $\chi^2$ downhill (the so-called *steepest descent* method), in small increments, until the second order taylor expansion becomes a better local approximation of $\chi^2$. The familiar *Levenberg-Marquardt* method provides a simple strategy to set the scale of the stepsize down the $\chi^2$ gradient.

There are two major areas of concern regarding the conventional nonlinear fitting technique outlined above. First, if the evaluation of the model function is expensive, in terms of CPU time, then an iterative approach may be impractical. Second, the requirement that the observables have a functional relation $y(x;\mathbf{a})$ might be awkward, if not impossible, to implement in code. In fact, in the most general case the set of observables need not even share the same units. Since the underlying goal of the fitting procedure is the extraction of the adjustable model

parameters **a**, there is no need to impose the requirement that each experimental observable be related to one another via a superfluous (with regard to the fitting procedure) independent variable. All that is required is that each observable be dependent on the same set of adjustable parameters.

A new technique for nonlinear least-squares fitting which addresses these concerns has been developed at UNH.[55,56] The philosophy behind the new fitting technique can be expressed in terms of three goals: first, to minimize the number of model evaluations necessary to converge on the final solution, second, to maximize the utilization of information gained from each evaluation, and third, to generalize the description of the model function by eliminating explicit references to unneeded independent variables.

Due to the nonlinearity of the fitting problem, it is not possible to escape the necessity of an iterative stepping procedure. An effective minimization technique, however, will *accumulate* information with each successive step rather than discard information obtained from bad steps. Given a set of observables $\mathbf{y} = \{y_1, ..., y_N\}$, each dependent on the same set of parameters $\mathbf{x} = \{x_1, ...x_M\}$, we can construct a taylor series expansion for each element of $\mathbf{y}$ about a vector $\mathbf{x}_o$ in the parameter space of $\mathbf{y}$.

$$y(\mathbf{x}) = y_o + \sum_{j=1}^{M} L_j(x_j - x_{oj}) + \sum_{j=1}^{M}\sum_{k=1}^{j} \frac{Q_{jk}}{1+\delta_{jk}}(x_j - x_{oj})(x_k - x_{ok}) \qquad \text{(A15)}$$

To determine the expansion coefficients $L_j$ and $Q_{jk}$ several evaluations of the model function $\mathbf{y}(\mathbf{x}) = \{\mathbf{y}(\mathbf{x}_1), ..., \mathbf{y}(\mathbf{x}_K)\}$ are required. The vector $\mathbf{x}$ which produces the lowest $\chi^2$ is generally chosen to be the expansion point $\mathbf{x}_o$. It is clear that the more vectors $\mathbf{y}$ one provides, the more rigorously defined the taylor expansion coefficients will be. With the basis set $\mathbf{y}(\mathbf{x})$ of model evaluations we can construct a set of coupled equations, expressed in matrix form by $\mathbf{A} \cdot \mathbf{t} = \mathbf{y}$, where

$$\mathbf{A} = \begin{pmatrix} 1 & x_{11} - x_{o1} & \cdots & (x_{11} - x_{o1})(x_{11} - x_{o1}) & \cdots \\ 1 & x_{21} - x_{o1} & \cdots & (x_{21} - x_{o1})(x_{21} - x_{o1}) & \cdots \\ \vdots & \vdots & \ddots & \vdots & \ddots \\ 1 & x_{K1} - x_{o1} & \cdots & (x_{K1} - x_{o1})(x_{K1} - x_{o1}) & \cdots \end{pmatrix} \qquad \text{(A16)}$$

$$t = \begin{pmatrix} y_o \\ L_1 \\ \vdots \\ Q_{11} \\ \vdots \end{pmatrix} \qquad y = \begin{pmatrix} y_1 \\ \vdots \\ y_K \end{pmatrix} \tag{A17}$$

The matrix **A** can then be inverted in order to solve for the vector **t** of taylor expansion coefficients.

The advantages gained from the taylor series expansion are immediately apparent. First, the model function is easily evaluated for all values of **x** using the taylor expansion coefficients. This is a great advantage in cases where the original set of model evaluations **y(x)** requires a large amount of CPU time to generate. Second, the taylor expansion of the observables is expressed directly in terms of the parameter set **x**, thereby eliminating all reference to additional unnecessary independent variables. Third, the taylor series can contain information about *all* true evaluations of the model function, since the number of elements in the basis set **y(x)** has no practical size limitation. In this manner we are able to incorporate all known information about the functional dependence of each observable on each of the adjustable parameters into the taylor expansion. The inclusion of rejected steps in the expansion will have the effect of inhibiting subsequent steps from straying into bad regions of parameter space, and in addition, the rejected steps will help determine the higher order derivatives of expression ( A 15).

Once the taylor expansion coefficients are determined for each observable, the $\chi^2$ minimization proceeds along essentially the same lines as the standard nonlinear least squares fit outlined above. The curvature matrix and the gradient, defined in equations ( A 13) and ( A 14), can be calculated from the first derivative of the taylor expansion

$$b_k = \frac{\partial \chi^2}{\partial x_k} = L_k + \sum_{j=1}^{M} Q_{kj}(x_{kj} - x_{oj}) \tag{A18}$$

Once the new step $\delta\mathbf{x}$ is calculated by solving equation ( A 12), the set of observables $\mathbf{y(x + \delta x)}$ can be calculated from the taylor series expansion of equation

( A 15). If $\chi^2$ is reduced, then the procedure can be repeated again, this time by calculating the gradient and curvature at the improved parameter coordinates $\mathbf{x}$. When convergence is reached, the final set of parameters $\mathbf{x}_{min}$ can be tested by evaluating the true model function. The entire procedure may be repeated as often as desired, each time with one additional model vector $\mathbf{y}$.

# APPENDIX B

## Momentum Distributions for the Discrete Final States Observed in the $^{16}O(e,e'p)^{15}N$ Reaction.

**Table B.1** Momentum distribution for the $1p_{1/2}$ ground state of $^{15}N$

| $p_m$ MeV/c | $\rho(\mathbf{p}_m)$ $[MeV/c]^{-3}$ | $\sigma$ $[MeV/c]^{-3}$ | $p_m$ MeV/c | $\rho(\mathbf{p}_m)$ $[MeV/c]^{-3}$ | $\sigma$ $[MeV/c]^{-3}$ |
|---|---|---|---|---|---|
| 12.5 | 4.635 | 2.648 | | | |
| 17.5 | 8.557 | 2.961 | | | |
| 22.5 | 11.723 | 1.748 | -22.5 | 4.432 | 2.670 |
| 27.5 | 14.175 | 1.668 | -27.5 | 5.824 | 2.960 |
| 32.5 | 22.712 | 2.346 | | | |
| 37.5 | 26.556 | 2.090 | | | |
| 42.5 | 26.440 | 1.905 | -42.5 | 10.582 | 1.711 |
| 47.5 | 32.048 | 2.762 | -47.5 | 15.020 | 2.101 |
| 52.5 | 31.806 | 1.894 | -52.5 | 19.143 | 2.186 |
| 57.5 | 39.073 | 2.120 | -57.5 | 23.471 | 2.611 |
| 62.5 | 38.350 | 2.500 | -62.5 | 21.787 | 3.255 |
| 67.5 | 37.340 | 2.212 | -67.5 | 23.394 | 3.578 |
| 72.5 | 39.864 | 2.239 | | | |
| 77.5 | 43.329 | 1.925 | -77.5 | 28.276 | 6.583 |
| 82.5 | 40.431 | 1.958 | -82.5 | 29.411 | 8.411 |
| 87.5 | 41.947 | 1.901 | -87.5 | 30.445 | 3.408 |
| 92.5 | 38.569 | 1.995 | -92.5 | 31.303 | 3.159 |
| 97.5 | 39.173 | 2.998 | -97.5 | 31.529 | 3.543 |
| 102.5 | 35.999 | 1.691 | -102.5 | 30.209 | 4.245 |
| 107.5 | 34.450 | 1.523 | -107.5 | 32.273 | 4.708 |
| 112.5 | 31.265 | 1.385 | -112.5 | 31.061 | 4.720 |
| 117.5 | 29.389 | 1.291 | -117.5 | 28.191 | 4.652 |
| 122.5 | 28.479 | 1.115 | -122.5 | 26.438 | 4.609 |
| 127.5 | 26.754 | 1.186 | -127.5 | 27.395 | 3.838 |
| 132.5 | 25.200 | 1.269 | -132.5 | 22.161 | 3.989 |
| 137.5 | 22.287 | 1.040 | -137.5 | 24.109 | 5.440 |
| 142.5 | 18.201 | 1.601 | -142.5 | 23.974 | 4.899 |
| 147.5 | 17.355 | 1.123 | -147.5 | 25.421 | 5.135 |
| 152.5 | 15.299 | 0.969 | -152.5 | 18.623 | 3.074 |

**Table B.1** Momentum distribution for the $1p_{1/2}$ ground state of $^{15}N$

| $p_m$ MeV/c | $\rho(\mathbf{p}_m)$ $[\mathrm{MeV}/c]^{-3}$ | $\sigma$ $[\mathrm{MeV}/c]^{-3}$ | $p_m$ MeV/c | $\rho(\mathbf{p}_m)$ $[\mathrm{MeV}/c]^{-3}$ | $\sigma$ $[\mathrm{MeV}/c]^{-3}$ |
|---|---|---|---|---|---|
| 157.5 | 13.963 | 0.755 | | | |
| 162.5 | 12.310 | 0.605 | -162.5 | 22.167 | 3.407 |
| 167.5 | 11.733 | 0.781 | -167.5 | 18.616 | 3.067 |
| 172.5 | 9.629 | 0.633 | -172.5 | 20.591 | 3.801 |
| 177.5 | 7.700 | 0.548 | -177.5 | 16.605 | 3.870 |
| 182.5 | 7.212 | 0.809 | | | |
| 187.5 | 6.435 | 0.513 | | | |
| 192.5 | 5.372 | 0.423 | | | |
| 197.5 | 4.115 | 0.295 | | | |
| 202.5 | 4.065 | 0.368 | | | |
| 207.5 | 3.143 | 0.331 | | | |
| 212.5 | 3.094 | 0.454 | | | |
| 227.5 | 1.565 | 0.218 | | | |
| 232.5 | 1.252 | 0.218 | | | |
| 245.0 | 0.973 | 0.206 | | | |
| 255.0 | 0.504 | 0.077 | | | |
| 265.0 | 0.292 | 0.064 | | | |

**Table B.2** Momentum distribution for the $(2s_{1/2},1d_{5/2})$ doublet at $E_x$ = 5.30 MeV

| $p_m$ MeV/c | $\rho(\mathbf{p}_m)$ $[\mathrm{MeV/c}]^{-3}$ | $\sigma$ $[\mathrm{MeV/c}]^{-3}$ | $p_m$ MeV/c | $\rho(\mathbf{p}_m)$ $[\mathrm{MeV/c}]^{-3}$ | $\sigma$ $[\mathrm{MeV/c}]^{-3}$ |
|---|---|---|---|---|---|
| 15.0 | 9.164 | 2.282 | -15.0 | 9.940 | 2.926 |
| 25.0 | 6.960 | 0.756 | -25.0 | 7.338 | 2.376 |
| 35.0 | 6.247 | 0.560 | -35.0 | 8.321 | 1.070 |
| 45.0 | 4.501 | 0.411 | -45.0 | 7.062 | 0.882 |
| 55.0 | 3.603 | 0.381 | -55.0 | 6.245 | 1.029 |
| 65.0 | 3.778 | 0.396 | -65.0 | 4.658 | 0.966 |
| 75.0 | 2.919 | 0.287 | -75.0 | 4.463 | 1.329 |
| 85.0 | 2.952 | 0.268 | -85.0 | 2.800 | 0.904 |
| 95.0 | 2.676 | 0.234 | -95.0 | 3.752 | 0.992 |
| 105.0 | 2.583 | 0.238 | -105.0 | 4.648 | 1.312 |
| 115.0 | 2.716 | 0.199 | -115.0 | 2.153 | 0.613 |
| 125.0 | 2.382 | 0.176 | -125.0 | 2.323 | 0.858 |
| 135.0 | 2.151 | 0.183 | -135.0 | 2.103 | 0.783 |
| 145.0 | 2.256 | 0.165 | -145.0 | 2.804 | 0.718 |
| 155.0 | 1.662 | 0.144 | -155.0 | 3.785 | 0.946 |
| 165.0 | 1.857 | 0.150 | -165.0 | 2.028 | 0.720 |
| 175.0 | 1.697 | 0.132 | | | |
| 185.0 | 1.137 | 0.127 | | | |
| 195.0 | 1.062 | 0.108 | | | |
| 205.0 | 0.899 | 0.112 | | | |
| 215.0 | 0.644 | 0.064 | | | |
| 225.0 | 0.451 | 0.045 | | | |
| 235.0 | 0.282 | 0.036 | | | |
| 245.0 | 0.151 | 0.034 | | | |
| 255.0 | 0.098 | 0.025 | | | |

**Table B.3** Momentum distribution for the $1p_{3/2}$ state at $E_x = 6.32$ MeV

| $p_m$ MeV/c | $\rho(\mathbf{p}_m)$ $[\text{MeV/c}]^{-3}$ | $\sigma$ $[\text{MeV/c}]^{-3}$ | $p_m$ MeV/c | $\rho(\mathbf{p}_m)$ $[\text{MeV/c}]^{-3}$ | $\sigma$ $[\text{MeV/c}]^{-3}$ |
|---|---|---|---|---|---|
| 12.5 | 16.233 | 4.279 | | | |
| 17.5 | 16.387 | 3.447 | | | |
| 22.5 | 18.547 | 2.232 | -22.5 | 6.737 | 2.021 |
| 27.5 | 24.005 | 1.921 | -27.5 | 8.458 | 1.978 |
| 32.5 | 30.682 | 2.335 | | | |
| 37.5 | 36.028 | 2.431 | | | |
| 42.5 | 36.319 | 2.695 | -42.5 | 16.268 | 3.411 |
| 47.5 | 41.317 | 2.226 | -47.5 | 23.023 | 2.920 |
| 52.5 | 41.849 | 2.138 | -52.5 | 20.711 | 2.387 |
| 57.5 | 44.091 | 2.291 | -57.5 | 23.896 | 3.125 |
| 62.5 | 46.381 | 2.051 | -62.5 | 23.185 | 3.107 |
| 67.5 | 51.582 | 2.552 | | | |
| 72.5 | 53.117 | 2.941 | -72.5 | 33.796 | 7.002 |
| 77.5 | 50.344 | 2.509 | -77.5 | 38.761 | 8.367 |
| 82.5 | 52.503 | 2.281 | -82.5 | 31.738 | 4.658 |
| 87.5 | 50.747 | 2.166 | -87.5 | 39.706 | 5.104 |
| 92.5 | 49.768 | 2.800 | | | |
| 97.5 | 47.489 | 1.815 | -97.5 | 35.218 | 4.692 |
| 102.5 | 44.985 | 1.751 | -102.5 | 42.160 | 3.887 |
| 107.5 | 45.699 | 1.822 | | | |
| 112.5 | 43.207 | 1.704 | -112.5 | 39.707 | 3.803 |
| 117.5 | 41.861 | 1.449 | -117.5 | 44.610 | 4.605 |
| 122.5 | 39.624 | 1.496 | -122.5 | 40.936 | 4.477 |
| 127.5 | 34.488 | 1.299 | -127.5 | 41.294 | 4.553 |
| 132.5 | 32.478 | 1.243 | -132.5 | 40.514 | 4.582 |
| 137.5 | 29.265 | 1.121 | -137.5 | 37.416 | 5.375 |
| 142.5 | 25.738 | 1.108 | -142.5 | 35.449 | 5.046 |
| 147.5 | 23.179 | 1.238 | -147.5 | 32.492 | 3.835 |
| 152.5 | 21.968 | 1.033 | -152.5 | 36.787 | 6.297 |
| 157.5 | 19.690 | 1.233 | -157.5 | 36.479 | 4.114 |
| 162.5 | 17.048 | 0.834 | -162.5 | 28.788 | 3.666 |
| 167.5 | 15.039 | 0.748 | -167.5 | 28.030 | 4.152 |
| 172.5 | 13.259 | 0.634 | -172.5 | 25.954 | 4.542 |
| 177.5 | 11.842 | 0.595 | -177.5 | 32.572 | 6.803 |
| 182.5 | 9.403 | 0.678 | | | |

**Table B.3** Momentum distribution for the $1p_{3/2}$ state at $E_r = 6.32$ MeV

| $p_m$ MeV/c | $\rho(\mathbf{p}_m)$ $[\text{MeV/c}]^{-3}$ | $\sigma$ $[\text{MeV/c}]^{-3}$ | $p_m$ MeV/c | $\rho(\mathbf{p}_m)$ $[\text{MeV/c}]^{-3}$ | $\sigma$ $[\text{MeV/c}]^{-3}$ |
|---|---|---|---|---|---|
| 187.5 | 8.172 | 0.546 | | | |
| 192.5 | 7.841 | 0.556 | | | |
| 197.5 | 6.664 | 0.396 | | | |
| 202.5 | 6.135 | 0.473 | | | |
| 207.5 | 4.647 | 0.683 | | | |
| 212.5 | 3.778 | 0.515 | | | |
| 217.5 | 3.268 | 0.255 | | | |
| 222.5 | 2.576 | 0.318 | | | |
| 227.5 | 2.259 | 0.175 | | | |
| 232.5 | 2.052 | 0.255 | | | |
| 235.0 | 1.490 | 0.182 | | | |
| 245.0 | 0.957 | 0.104 | | | |
| 255.0 | 0.898 | 0.095 | | | |
| 265.0 | 0.563 | 0.095 | | | |

**Table B.4** Momentum distribution for the $1g_{7/2}$ state at $E_x = 7.57$ MeV

| $p_m$ MeV/c | $\rho(\mathbf{p}_m)$ $[\text{MeV/c}]^{-3}$ | $\sigma$ $[\text{MeV/c}]^{-3}$ | $p_m$ MeV/c | $\rho(\mathbf{p}_m)$ $[\text{MeV/c}]^{-3}$ | $\sigma$ $[\text{MeV/c}]^{-3}$ |
|---|---|---|---|---|---|
| 35.0 | 0.235 | 0.257 | | | |
| 45.0 | 0.344 | 0.200 | | | |
| 65.0 | 0.476 | 0.282 | | | |
| 75.0 | 0.798 | 0.299 | | | |
| 85.0 | 1.106 | 0.295 | | | |
| 95.0 | 0.958 | 0.305 | | | |
| 105.0 | 1.169 | 0.245 | | | |
| 115.0 | 1.206 | 0.209 | | | |
| 125.0 | 0.830 | 0.174 | | | |
| 135.0 | 0.767 | 0.164 | | | |
| 145.0 | 0.980 | 0.214 | | | |
| 155.0 | 0.832 | 0.146 | | | |
| 165.0 | 0.385 | 0.107 | | | |
| 175.0 | 0.342 | 0.091 | | | |
| 190.0 | 0.355 | 0.085 | | | |
| 202.5 | 0.245 | 0.063 | | | |
| 215.0 | 0.142 | 0.032 | | | |
| 225.0 | 0.095 | 0.023 | | | |
| 235.0 | 0.104 | 0.022 | | | |
| 245.0 | 0.090 | 0.016 | | | |
| 255.0 | 0.030 | 0.008 | | | |
| 265.0 | 0.041 | 0.009 | | | |

**Table B.5** Momentum distribution for the $1s_{1/2}$ state at $E_x = 8.31$ MeV

| $p_m$ MeV/c | $\rho(\mathbf{p}_m)$ $[\mathrm{MeV/c}]^{-3}$ | $\sigma$ $[\mathrm{MeV/c}]^{-3}$ | $p_m$ MeV/c | $\rho(\mathbf{p}_m)$ $[\mathrm{MeV/c}]^{-3}$ | $\sigma$ $[\mathrm{MeV/c}]^{-3}$ |
|---|---|---|---|---|---|
| 25.0 | 0.827 | 0.476 | | | |
| 35.0 | 0.970 | 0.279 | -35.0 | 2.283 | 0.444 |
| 45.0 | 0.403 | 0.210 | -45.0 | 1.311 | 0.322 |
| 55.0 | 0.766 | 0.240 | -55.0 | 1.461 | 0.319 |
| 65.0 | 0.849 | 0.286 | -65.0 | 1.132 | 0.321 |
| 75.0 | 0.515 | 0.170 | -75.0 | 2.349 | 0.632 |
| | | | -85.0 | 0.921 | 0.390 |
| 95.0 | 0.485 | 0.186 | -95.0 | 1.127 | 0.396 |
| 105.0 | 0.206 | 0.122 | -105.0 | 0.529 | 0.354 |
| 115.0 | 0.201 | 0.119 | -115.0 | 0.988 | 0.441 |
| 125.0 | 0.261 | 0.110 | -125.0 | 1.340 | 0.444 |
| 135.0 | 0.335 | 0.099 | | | |
| 145.0 | 0.241 | 0.088 | -145.0 | 0.884 | 0.601 |
| 155.0 | 0.174 | 0.084 | -155.0 | 1.149 | 0.399 |
| 165.0 | 0.213 | 0.077 | -165.0 | 1.290 | 0.661 |
| 175.0 | 0.171 | 0.061 | -175.0 | 0.725 | 0.708 |
| 185.0 | 0.201 | 0.073 | | | |
| 205.0 | 0.063 | 0.041 | | | |
| 215.0 | 0.053 | 0.028 | | | |
| 225.0 | 0.064 | 0.029 | | | |
| 235.0 | 0.040 | 0.023 | | | |
| 245.0 | 0.034 | 0.020 | | | |

**Table B.6** Momentum distribution for the $1d_{3/2}$ state at $E_x = 8.57$ MeV

| $p_m$ MeV/c | $\rho(\mathbf{p}_m)$ $[\text{MeV/c}]^{-3}$ | $\sigma$ $[\text{MeV/c}]^{-3}$ | $p_m$ MeV/c | $\rho(\mathbf{p}_m)$ $[\text{MeV/c}]^{-3}$ | $\sigma$ $[\text{MeV/c}]^{-3}$ |
|---|---|---|---|---|---|
| 27.5 | 1.7417 | 0.8543 | | | |
| 32.5 | 1.3658 | 0.6319 | | | |
| 37.5 | 1.1498 | 0.5641 | | | |
| 42.5 | 1.3296 | 0.5556 | | | |
| 47.5 | 1.2793 | 0.5418 | | | |
| 52.5 | 1.0382 | 0.5018 | | | |
| 57.5 | 0.9360 | 0.5299 | | | |
| 62.5 | 1.0496 | 0.4884 | 162.5 | 0.3712 | 0.1681 |
| 67.5 | 1.3265 | 0.5386 | | | |
| 72.5 | 0.7515 | 0.4239 | 172.5 | 0.3742 | 0.1513 |
| 77.5 | 0.8768 | 0.4003 | 177.5 | 0.2099 | 0.1338 |
| 82.5 | 0.8471 | 0.3962 | | | |
| 87.5 | 0.7638 | 0.3850 | | | |
| 92.5 | 0.8558 | 0.4459 | 192.5 | 0.1356 | 0.1193 |
| 97.5 | 0.6273 | 0.4148 | | | |
| 102.5 | 0.9155 | 0.3205 | | | |
| 107.5 | 0.6674 | 0.3282 | 207.5 | 0.1970 | 0.0799 |
| 112.5 | 0.9071 | 0.2941 | 212.5 | 0.1914 | 0.0657 |
| 117.5 | 0.6556 | 0.2527 | 217.5 | 0.1838 | 0.0659 |
| 122.5 | 0.6702 | 0.2447 | 222.5 | 0.1541 | 0.0612 |
| 127.5 | 1.0933 | 0.2513 | 227.5 | 0.1426 | 0.0587 |
| 132.5 | 0.7304 | 0.2456 | 232.5 | 0.1178 | 0.0503 |
| 137.5 | 0.5741 | 0.2195 | 237.5 | 0.1164 | 0.0473 |
| 142.5 | 0.6830 | 0.3190 | 242.5 | 0.1202 | 0.0463 |
| 147.5 | 0.5184 | 0.2436 | 247.5 | 0.0875 | 0.0378 |
| 152.5 | 0.4162 | 0.2029 | 252.5 | 0.1004 | 0.0395 |
| 157.5 | 0.3434 | 0.1816 | 257.5 | 0.0579 | 0.0423 |

**Table B.7** Momentum distribution for the $1s_{1/2}$ state at $E_x = 9.05$ MeV

| $p_m$ MeV/c | $\rho(\mathbf{p}_m)$ $[\text{MeV/c}]^{-3}$ | $\sigma$ $[\text{MeV/c}]^{-3}$ | $p_m$ MeV/c | $\rho(\mathbf{p}_m)$ $[\text{MeV/c}]^{-3}$ | $\sigma$ $[\text{MeV/c}]^{-3}$ |
|---|---|---|---|---|---|
| 25.0 | 2.192 | 0.612 | | | |
| 35.0 | 2.926 | 0.440 | -35.0 | 2.476 | 0.488 |
| 45.0 | 1.832 | 0.309 | -45.0 | 2.447 | 0.400 |
| 55.0 | 1.175 | 0.267 | -55.0 | 2.297 | 0.376 |
| 65.0 | 1.076 | 0.224 | -65.0 | 1.780 | 0.388 |
| 75.0 | 1.046 | 0.200 | -75.0 | 2.045 | 0.529 |
| 85.0 | 0.560 | 0.176 | -85.0 | 2.640 | 0.515 |
| 95.0 | 0.505 | 0.155 | -95.0 | 1.685 | 0.429 |
| 105.0 | 0.699 | 0.144 | -105.0 | 1.612 | 0.415 |
| 115.0 | 0.306 | 0.120 | -115.0 | 0.277 | 0.385 |
| 125.0 | 0.346 | 0.111 | -125.0 | 1.377 | 0.551 |
| 135.0 | 0.204 | 0.103 | -135.0 | 0.337 | 0.438 |
| | | | -145.0 | 0.082 | 0.342 |
| 155.0 | 0.169 | 0.081 | -155.0 | 0.923 | 0.433 |
| 165.0 | 0.077 | 0.065 | -165.0 | 0.949 | 0.554 |
| 175.0 | 0.105 | 0.053 | -175.0 | 2.024 | 0.926 |
| 185.0 | 0.250 | 0.078 | | | |
| 195.0 | 0.104 | 0.052 | | | |
| 205.0 | 0.068 | 0.067 | | | |
| 225.0 | 0.047 | 0.026 | | | |
| 235.0 | 0.035 | 0.021 | | | |
| 245.0 | 0.045 | 0.020 | | | |
| 255.0 | 0.019 | 0.014 | | | |

**Table B.8** Momentum distribution for the $1p_{3/2}$ state at $E_x = 9.93$ MeV

| $p_m$ MeV/c | $\rho(\mathbf{p}_m)$ $[\text{MeV/c}]^{-3}$ | $\sigma$ $[\text{MeV/c}]^{-3}$ | $p_m$ MeV/c | $\rho(\mathbf{p}_m)$ $[\text{MeV/c}]^{-3}$ | $\sigma$ $[\text{MeV/c}]^{-3}$ |
|---|---|---|---|---|---|
| 35.0 | 1.527 | 0.337 | | | |
| 45.0 | 2.026 | 0.317 | -45.0 | 1.470 | 0.447 |
| 55.0 | 2.391 | 0.364 | -55.0 | 1.013 | 0.451 |
| 65.0 | 3.531 | 0.347 | -65.0 | 2.394 | 0.672 |
| 75.0 | 3.236 | 0.314 | -75.0 | 2.413 | 0.824 |
| 85.0 | 2.815 | 0.299 | -85.0 | 3.101 | 0.920 |
| 95.0 | 2.878 | 0.274 | -95.0 | 4.006 | 1.186 |
| 105.0 | 3.267 | 0.252 | -105.0 | 4.628 | 1.138 |
| 115.0 | 2.681 | 0.239 | -115.0 | 4.000 | 0.962 |
| 125.0 | 2.322 | 0.203 | -125.0 | 2.832 | 0.653 |
| 135.0 | 2.170 | 0.236 | -135.0 | 6.002 | 1.224 |
| 145.0 | 1.322 | 0.171 | -145.0 | 4.139 | 1.140 |
| 155.0 | 1.063 | 0.155 | -155.0 | 3.709 | 0.873 |
| 165.0 | 1.021 | 0.138 | -165.0 | 2.946 | 0.974 |
| 175.0 | 0.482 | 0.078 | -175.0 | 3.295 | 1.421 |
| 185.0 | 0.406 | 0.093 | | | |
| 195.0 | 0.444 | 0.081 | | | |
| 205.0 | 0.494 | 0.064 | | | |
| 215.0 | 0.212 | 0.050 | | | |
| 225.0 | 0.166 | 0.039 | | | |
| 235.0 | 0.069 | 0.019 | | | |
| 255.0 | 0.014 | 0.016 | | | |

**Table B.9** Momentum distribution for the $1p_{3/2}$ state at $E_x = 10.70$ MeV

| $p_m$ MeV/c | $\rho(\mathbf{p}_m)$ $[\mathrm{MeV/c}]^{-3}$ | $\sigma$ $[\mathrm{MeV/c}]^{-3}$ | $p_m$ MeV/c | $\rho(\mathbf{p}_m)$ $[\mathrm{MeV/c}]^{-3}$ | $\sigma$ $[\mathrm{MeV/c}]^{-3}$ |
|---|---|---|---|---|---|
| 25.0 | 3.729 | 0.815 | | | |
| 35.0 | 2.767 | 0.429 | | | |
| 45.0 | 2.675 | 0.359 | -45.0 | 1.634 | 0.469 |
| 55.0 | 3.564 | 0.446 | -55.0 | 1.132 | 0.448 |
| 65.0 | 3.868 | 0.359 | -65.0 | 2.080 | 0.584 |
| 75.0 | 3.566 | 0.335 | -75.0 | 3.965 | 0.885 |
| 85.0 | 4.173 | 0.367 | -85.0 | 4.412 | 0.867 |
| 95.0 | 4.367 | 0.409 | -95.0 | 5.387 | 1.441 |
| 105.0 | 4.522 | 0.308 | -105.0 | 6.450 | 1.444 |
| 115.0 | 3.881 | 0.299 | -115.0 | 5.762 | 1.183 |
| 125.0 | 3.103 | 0.234 | -125.0 | 5.164 | 0.979 |
| 135.0 | 2.331 | 0.217 | -135.0 | 4.123 | 0.964 |
| 145.0 | 2.040 | 0.169 | -145.0 | 4.908 | 1.189 |
| 155.0 | 2.169 | 0.237 | -155.0 | 3.429 | 0.808 |
| 165.0 | 1.935 | 0.223 | -165.0 | 4.854 | 1.241 |
| 175.0 | 1.246 | 0.124 | | | |
| 185.0 | 0.826 | 0.122 | | | |
| 195.0 | 0.809 | 0.106 | | | |
| 205.0 | 0.993 | 0.086 | | | |
| 215.0 | 0.428 | 0.071 | | | |
| 225.0 | 0.329 | 0.058 | | | |
| 235.0 | 0.108 | 0.022 | | | |
| 245.0 | 0.102 | 0.025 | | | |
| 255.0 | 0.057 | 0.020 | | | |

**Table B.10** Momentum distribution for the $1d_{5/2}$ state at $E_x = 12.10$ MeV

| $p_m$ MeV/c | $\rho(\mathbf{p}_m)$ $[\text{MeV/c}]^{-3}$ | $\sigma$ $[\text{MeV/c}]^{-3}$ | $p_m$ MeV/c | $\rho(\mathbf{p}_m)$ $[\text{MeV/c}]^{-3}$ | $\sigma$ $[\text{MeV/c}]^{-3}$ |
|---|---|---|---|---|---|
| | | | -15.0 | 1.690 | 1.391 |
| 25.0 | 0.924 | 0.519 | -25.0 | 1.384 | 0.897 |
| 35.0 | 0.092 | 0.167 | -35.0 | 0.970 | 0.624 |
| 45.0 | 0.239 | 0.160 | -45.0 | 0.231 | 0.242 |
| 55.0 | 0.203 | 0.234 | -55.0 | 0.813 | 0.369 |
| 65.0 | 0.260 | 0.200 | -65.0 | 1.004 | 0.493 |
| | | | -75.0 | 0.544 | 0.510 |
| 95.0 | 0.285 | 0.149 | -95.0 | 0.844 | 0.488 |
| 105.0 | 0.222 | 0.137 | -105.0 | 0.415 | 0.516 |
| 115.0 | 0.407 | 0.115 | -115.0 | 1.303 | 0.596 |
| 125.0 | 0.328 | 0.104 | -125.0 | 0.864 | 0.569 |
| 135.0 | 0.410 | 0.093 | -135.0 | 1.503 | 0.604 |
| 145.0 | 0.259 | 0.081 | -145.0 | 0.787 | 0.431 |
| 155.0 | 0.293 | 0.087 | -155.0 | 0.712 | 0.395 |
| 165.0 | 0.260 | 0.081 | -165.0 | 1.541 | 0.723 |
| 175.0 | 0.160 | 0.056 | -175.0 | 0.151 | 0.647 |
| 185.0 | 0.245 | 0.077 | | | |
| 195.0 | 0.116 | 0.042 | | | |
| 215.0 | 0.288 | 0.058 | | | |
| 225.0 | 0.067 | 0.028 | | | |
| 235.0 | 0.062 | 0.018 | | | |
| 245.0 | 0.026 | 0.019 | | | |

**Table B.11** Momentum distribution for the $1d_{5/2}$ state at $E_x = 12.92$ MeV

| $p_m$ MeV/c | $\rho(\mathbf{p}_m)$ $[\text{MeV/c}]^{-3}$ | $\sigma$ $[\text{MeV/c}]^{-3}$ | $p_m$ MeV/c | $\rho(\mathbf{p}_m)$ $[\text{MeV/c}]^{-3}$ | $\sigma$ $[\text{MeV/c}]^{-3}$ |
|---|---|---|---|---|---|
| 25.0 | 0.111 | 0.514 | | | |
| 45.0 | 0.504 | 0.183 | | | |
| 55.0 | 0.378 | 0.187 | | | |
| 65.0 | 1.366 | 0.309 | | | |
| 75.0 | 0.575 | 0.164 | | | |
| 85.0 | 0.755 | 0.180 | | | |
| 95.0 | 0.679 | 0.176 | | | |
| 105.0 | 0.593 | 0.129 | | | |
| 115.0 | 0.605 | 0.125 | | | |
| 125.0 | 0.604 | 0.119 | | | |
| 135.0 | 0.359 | 0.109 | | | |
| 145.0 | 0.475 | 0.088 | | | |
| 155.0 | 0.292 | 0.091 | | | |
| 165.0 | 0.323 | 0.084 | | | |
| 175.0 | 0.175 | 0.056 | | | |
| 185.0 | 0.146 | 0.069 | | | |
| 195.0 | 0.081 | 0.038 | | | |
| 205.0 | 0.021 | 0.180 | | | |
| 215.0 | 0.128 | 0.045 | | | |
| 225.0 | 0.018 | 0.026 | | | |

# APPENDIX C

## Spectroscopic Factors from the Multipole Decomposition of the $^{16}O(e,e'p)^{15}N$ Spectral Function

**Table C.1**

| $E_m$ | $S_{l=0}$ | $\sigma$ | $S_{l=1}$ | $\sigma$ | $S_{l=2}$ | $\sigma$ |
|---|---|---|---|---|---|---|
| 10.5 | 1.690e-7 | 3.818e-3 | 1.429e-6 | 4.217e-3 | 1.640e-3 | 7.109e-3 |
| 11.5 | 4.792e-3 | 1.895e-4 | 1.960e-9 | 1.739e-4 | 6.891e-3 | 3.028e-4 |
| 12.5 | 8.017e-3 | 3.594e-3 | 1.201 | 8.661e-3 | 9.487e-6 | 4.541e-3 |
| 13.5 | 1.309e-4 | 1.961e-3 | 2.390e-2 | 2.947e-3 | 1.638e-3 | 3.498e-3 |
| 14.5 | 1.238e-3 | 2.186e-3 | 1.375e-2 | 2.802e-3 | 1.310e-6 | 2.886e-3 |
| 15.5 | 3.560e-3 | 1.353e-3 | 1.311e-2 | 2.726e-3 | 1.764e-6 | 3.282e-3 |
| 16.5 | 3.005e-3 | 1.740e-3 | 9.341e-3 | 3.376e-3 | 3.329e-6 | 3.162e-3 |
| 17.5 | 3.254e-2 | 1.770e-3 | 8.520e-3 | 3.014e-3 | 1.101e-1 | 4.267e-3 |
| 18.5 | 6.560e-4 | 1.340e-3 | 2.341 | 1.344e-2 | 2.185e-6 | 4.948e-3 |
| 19.5 | 3.279e-3 | 4.845e-3 | 4.503e-2 | 4.568e-3 | 1.087e-2 | 4.178e-3 |
| 20.5 | 1.839e-2 | 1.505e-3 | 3.296e-2 | 3.792e-3 | 1.380e-2 | 2.986e-3 |
| 21.5 | 3.964e-2 | 4.629e-3 | 1.217e-1 | 4.057e-3 | 5.760e-7 | 2.297e-3 |
| 22.5 | 6.378e-6 | 3.860e-3 | 2.941e-1 | 5.412e-3 | 1.615e-2 | 3.903e-3 |
| 23.5 | 1.206e-2 | 3.657e-3 | 3.153e-2 | 3.499e-3 | 0.040e-9 | 2.651e-3 |
| 24.5 | 6.521e-3 | 3.783e-3 | 4.426e-2 | 3.501e-3 | 1.789e-2 | 2.594e-3 |
| 25.5 | 6.215e-3 | 3.687e-3 | 3.503e-2 | 3.233e-3 | 3.948e-3 | 2.394e-3 |
| 26.5 | 3.201e-2 | 3.341e-3 | 4.314e-3 | 3.033e-3 | 5.515e-3 | 2.375e-3 |
| 27.5 | 2.638e-2 | 3.247e-3 | 6.269e-8 | 2.875e-3 | 5.428e-4 | 2.404e-3 |
| 28.5 | 5.169e-2 | 3.521e-3 | 2.925e-7 | 2.842e-3 | 1.115e-2 | 2.303e-3 |
| 29.5 | 5.456e-2 | 3.717e-3 | 1.045e-2 | 3.215e-3 | 1.114e-4 | 2.393e-3 |
| 30.5 | 4.029e-2 | 3.629e-3 | 1.327e-2 | 3.091e-3 | 4.382e-7 | 2.256e-3 |
| 31.5 | 3.282e-2 | 3.642e-3 | 2.048e-2 | 3.149e-3 | 3.240e-9 | 1.805e-3 |
| 32.5 | 4.585e-2 | 3.828e-3 | 2.270e-7 | 3.147e-3 | 1.229e-2 | 2.511e-3 |
| 33.5 | 4.816e-2 | 4.021e-3 | 1.133e-2 | 3.410e-3 | 3.073e-3 | 2.539e-3 |
| 34.5 | 6.291e-2 | 4.285e-3 | 6.445e-4 | 3.625e-3 | 6.557e-3 | 2.708e-3 |
| 35.5 | 6.489e-2 | 4.669e-3 | 3.025e-4 | 3.865e-3 | 8.604e-3 | 2.911e-3 |
| 36.5 | 6.571e-2 | 4.981e-3 | 7.528e-3 | 4.069e-3 | 2.211e-8 | 2.949e-3 |
| 37.5 | 8.955e-2 | 5.509e-3 | 2.209e-8 | 3.452e-3 | 1.437e-6 | 2.597e-3 |
| 38.5 | 7.384e-2 | 5.962e-3 | 5.369e-3 | 4.813e-3 | 1.233e-7 | 3.141e-3 |
| 39.5 | 7.963e-2 | 6.343e-3 | 1.741e-7 | 3.211e-3 | 0.040e-9 | 2.561e-3 |